Dissertation

submitted to the
Combined Faculties for the Natural Sciences and for Mathematics
of the Ruperto-Carola University of Heidelberg, Germany
for the degree of

Doctor of Natural Sciences

Put forward by
Dipl.-Phys.: Kathrin Egberts
Born in: Mülheim/Ruhr, Germany

Oral examination: 30.03.2009

The Energy Spectrum of Cosmic-Ray Electrons Measured with H.E.S.S.

Referees:	Prof. Dr. Werner Hofmann
	Prof. Dr. Andreas Quirrenbach

Abstract

The spectrum of cosmic-ray electrons has so far been measured using balloon and satellite-based instruments. At TeV energies, however, the sensitivity of such instruments is very limited due to the low flux of electrons at very high energies and small detection areas of balloon/satellite based experiments. The very large collection area of ground-based imaging atmospheric Cherenkov telescopes gives them a substantial advantage over balloon/satellite based instruments when detecting very-high-energy electrons (> 300 GeV). By analysing data taken by the High Energy Stereoscopic System (H.E.S.S.), this work extends the known electron spectrum up to 4 TeV – a range that is not accessible to direct measurements. However, in contrast to direct measurements, imaging atmospheric Cherenkov telescopes such as H.E.S.S. detect air showers that comic-ray electrons initiate in the atmosphere rather than the primary particle. Thus, the main challenge is to differentiate between air showers initiated by electrons and those initiated by the hadronic background. A new analysis technique was developed that determines the background with the support of the machine-learning algorithm Random Forest. It is shown that this analysis technique can also be applied in other areas such as the analysis of diffuse γ rays from the Galactic plane.

Kurzfassung

Das Spektrum der kosmischen Elektronen wurde bisher nur mit Ballon- und Satellitenexperimenten gemessen. Bei hohen Energien im TeV-Bereich ist allerdings die Sensitivität dieser Experimente nicht ausreichend, da bei diesen Energien der Teilchenfluss der Elektronen nur sehr gering ist und Ballon- oder Satellitenexperimente nur über sehr kleine Detektionsflächen verfügen. Die sehr großen Detektionsflächen von erdgebundenen Experimenten sind im Gegensatz dazu besonders geeignet für die Messung von hochenergetischen, kosmischen Elektronen (> 300 GeV). Durch die Analyse von Daten, die mit dem High Energy Stereoscopic System (H.E.S.S.) gemessen wurden, wird in dieser Arbeit erstmalig das bisher bekannte Spektrum der kosmischen Elektronen auf 4 TeV erweitert - ein Bereich, der nicht mehr von ballon- und satellitengestützten Messungen abgedeckt werden kann. Im Vergleich zu direkten Messungen detektieren abbildende Cherenkovteleskope wie H.E.S.S. nicht die Primärteilchen sondern die Luftschauer, die diese in der Atmosphäre erzeugen. Eine Hauptherausforderung ist damit die Unterscheidung zwischen Luftschauern, die von Elektronen, und solchen, die von hadronischem Untergrund erzeugt werden. Dazu wurde in dieser Arbeit eine neue Analysemethode entwickelt, die den Untergrund mit Hilfe des selbstlernenden Algorithmus Random Forest bestimmt. Es wird gezeigt, dass diese Analysemethode auch auf andere Anwendungen übertragbar ist wie zum Beispiel die Analyse von diffuser γ-Strahlung aus der Galaktischen Ebene.

Contents

List of Figures

List of Tables

Preface

Cosmic rays puzzle us since their discovery between 1911 and 1913, when Victor Hess found in ten balloon ascents a penetrating *cosmic radiation* – a discovery that was honoured with the Nobel Prize in 1936. Although a lot of progress has been made in recent years in unveiling the mysteries of cosmic rays, still many questions remain open.

Cosmic rays hit the Earth's atmosphere with ≈1000 particles per second and square meter. While the majority of cosmic rays are protons and nuclei, only a small fraction consists of electrons. However, this somewhat enigmatic component of cosmic rays provides rather different and indeed complementary information compared to that of cosmic-ray protons and nuclei. Due to their low masses, electrons above a few GeV suffer severe radiative energy losses. These energy losses restrict the lifetime of cosmic-ray electrons so drastically that TeV electrons can reach the Earth only from rather local (< 1 kpc) astrophysical accelerators. Previous instruments that measured cosmic-ray electrons were balloon and satellite-based. The sensitivity of these experiments, however, was extremely limited at TeV energies due to their small physical size and short duration of flight.

This work presents the first measurement of cosmic-ray electrons made from ground level. Imaging atmospheric Cherenkov telescopes like the H.E.S.S. experiment represent with their large effective collection area and superior sensitivity an excellent tool for measuring very-high-energy electrons and can extend the measured electron spectrum up to ≈10 TeV. While a distinction of electrons and γ rays can be made by using the anisotropic nature of γ rays and excluding any possible γ-ray emission region from the data, the main difficulty of this challenging measurement lies in the determination of the vast hadronic background. At TeV energies, only one in thousand cosmic-ray particles is an electron and their identification can only be done indirectly via the shape of the air showers they produce in the atmosphere when interacting with air molecules. In this analysis, the background subtraction is performed by applying hard selection cuts and then modelling the data passing the cuts with Monte Carlo simulations of electrons and protons in the distributions of a separation parameter ζ. This method involves large systematic uncertainties, which arise from a lack of knowledge of the relevant strong interaction physics at high energies required for the proton simulations. The systematic effects involved in this analysis are investigated in detail.

The spectrum measured with H.E.S.S., which is presented in this work, extends to 4 TeV with small statistical and systematic errors, and potentially to 10 TeV with larger systematic uncertainties. This measurement implies the existence of a local electron accelerator as close as $\lesssim 1$ kpc.

Furthermore, the analysis developed for the cosmic-ray electron measurement can, with small modifications, be applied to extended γ-ray sources. This is useful for the case where the source extension is comparable to the field of view of the camera and thus a background subtraction from regions with no γ-ray emission in the field of view is not possible. An application of this method to the search for large-scale diffuse γ-ray emission in the Galactic plane is included.

This work is structured as follows:

- Chapter 1 is dedicated to the physics background of the analysis. It summarises the physics of cosmic rays and cosmic-ray electrons in particular and addresses the connection between cosmic rays and diffuse γ rays.
- The imaging atmospheric Cherenkov technique is introduced in Chapter 2. The H.E.S.S. experiment is presented and air-shower physics and air-shower simulations are discussed.
- Chapter 3 describes the analysis of cosmic-ray electrons and presents the measured electron spectrum. The spectrum is interpreted in terms of a nearby electron accelerator. Other explanations of the 4–10 TeV signature in the spectrum are discussed.
- A conclusion is given in Chapter 4. An application of the method to the diffuse γ-ray emission follows in the Appendix B.

Chapter 1

Cosmic-Ray Electrons - an Introduction

In this chapter the physics background of the analysis presented in this work is introduced. In the focus are cosmic-ray electrons at TeV energies, their properties and possible sources. The starting point of the discussion are the already measured spectra of cosmic-ray electrons as well as nucleonic cosmic rays (Section 1.1). The energy loss mechanisms and possible sources of cosmic-ray electrons are discussed in Section 1.2. Predictions can be made for the shape of the electron spectrum under the assumption of certain source distributions by solving the diffusion equation. This is shown in Section 1.3 and applied to actually existing objects. Finally, in Section 1.4 the background of a cosmic-ray electron measurement in form of diffuse γ rays is discussed.

Throughout this work the terminus *electrons* will refer to both particle and antiparticle. The presented measurement (as well as many direct measurements) cannot distinguish between charges. If a distinction has to be made, particles will be addressed as *negative electrons* and antiparticles as *positrons.*

1.1 The Spectrum of Cosmic Rays

1.1.1 Electrons

Fig. 1.1 shows the spectrum of cosmic-ray electrons in comparison with the nucleonic cosmic rays. The cosmic-ray electron spectrum is measured between 1 GeV and 2 TeV with balloon and satellite-borne instruments using electromagnetic calorimeters, and, since the longitudinal shower profile in the calorimeters alone is not suited for an efficient proton rejection, also with transition radiation detectors and/or magnetic spectrometers as is the case for the AMS (Aguilar et al. (2002)) and HEAT experiment (Barwick et al. (1998)). Other tools for particle identification are emulsion chambers that allow a visual observation of the shower (Kobayashi et al. (2004)) or imaging calorimeters exploring the longitudinal and lateral shower development, which are implemented in the BETS (Torii et al. (2001)) and ATIC detector (Guzik (2008)).
Further data are expected in the near future from the PAMELA (Picozza et al. (2007))

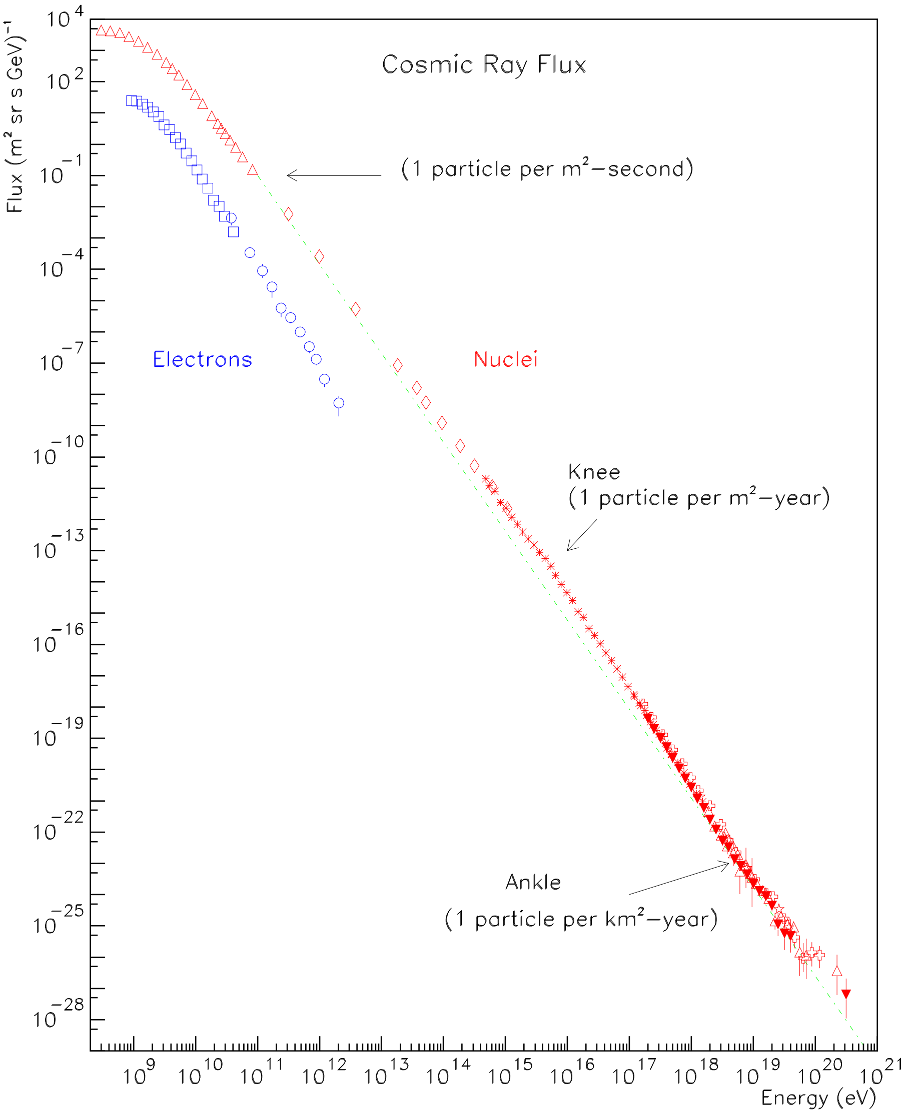

Figure 1.1: The spectrum of cosmic rays [adapted from S. Swordy].

and FERMI experiment (Moiseev et al. (2007), Ormes & Moiseev (2007)). The CREST experiment uses a completely different approach: the indirect detection of electrons via their synchrotron radiation produced in the Earth's magnetic field (Yagi & et al. (2005)). The CREST experiment is designed to be sensitive to electrons at 2–50 TeV and higher and is scheduled to be launched in 2009. On a long term perspective, the Calet experiment (The Calet Collaboration (2007)) is planned to measure the whole electron spectrum in the range of 1 GeV to 10 TeV with one instrument on board of the International Space Station.

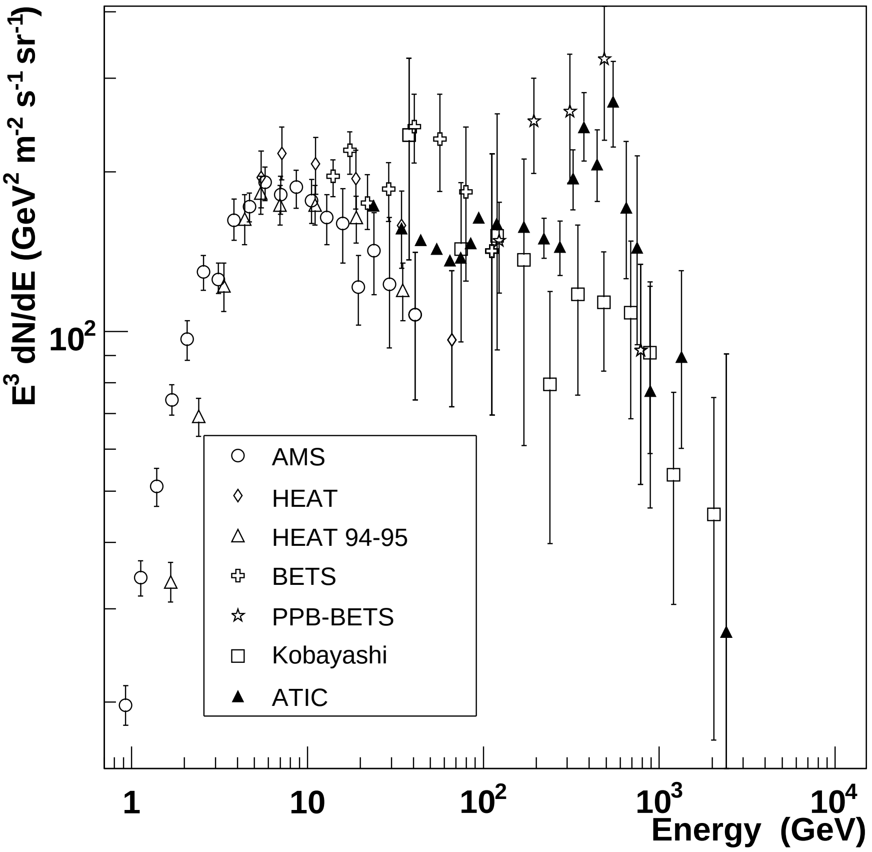

Figure 1.2: The spectrum of cosmic-ray electrons. Data are reproduced from: AMS (Aguilar et al. (2002)), HEAT (Barwick et al. (1998)), HEAT 94-95 (DuVernois et al. (2001)), BETS (Torii et al. (2001)), PPB-BETS (Torii et al. (2008)) Kobayashi (Kobayashi et al. (2004)) and ATIC (Chang et al. (2008)).

A collection of measurements of the cosmic-ray electron spectrum is shown in Fig. 1.2 in a presentation of flux scaled by the energy cubed, which has the advantage of making features in the very steep spectrum visible. At the lower end of the spectrum, solar modulation alters the original spectrum; interactions of cosmic-ray electrons with the varying field of the heliosphere cause a dependence of the spectrum on the solar activity. Between $\approx$10 GeV and 1 TeV the electron spectrum follows a powerlaw $\frac{dF}{dE} \propto E^{-\Gamma}$ with a *spectral index* of $\Gamma = 3.3$. An interesting feature of the spectrum in this range is the "bump" that was observed by the ATIC experiment between 300 and 800 GeV and which was recently interpreted as signature of Kaluza-Klein dark matter (Chang et al. (2008)). Beyond 2 TeV the fluxes become too low for balloon and satellite measurements and a ground-based installation is needed to determine the end of the cosmic-ray electron spectrum as first suggested by Nishimura (1994). The implementation of such a measurement with H.E.S.S. is the topic of this work.

The Positron Fraction

Besides their spectrum cosmic-ray electrons are characterised by their composition of negative electrons and positrons. As will be discussed in the next section, different production mechanisms lead to different positron fractions. Therefore, the positron-electron fraction is an important tool to discriminate between the mechanisms. The positron fraction as function of energy is shown in Fig. 1.3 with stress on the latest PAMELA results (Adriani et al. (2008)). At low energies the deviation of the PAMELA results with respect to other observations can be explained by a charge dependence of solar modulation effects. At ≈10 GeV the positrons form only about 5% of all electrons, which indicates that the bulk of cosmic-ray electrons is accelerated via diffusive shock acceleration and positrons are mostly of secondary origin. The rise at energies above 10 GeV to more than 10% could be an indication for a dark matter or pulsar contribution to the cosmic-ray electron spectrum (Dario Serpico (2008)).

Before in the following sections the energy loss mechanisms that are responsible for the steep electron spectrum and possible sources of cosmic-ray electrons are discussed, first a short summary on the nucleonic component of cosmic rays is given. The spectrum of the nucleonic component of cosmic rays as shown in Fig. 1.1 is especially important for this work as it constitutes a major background for the presented electron analysis.

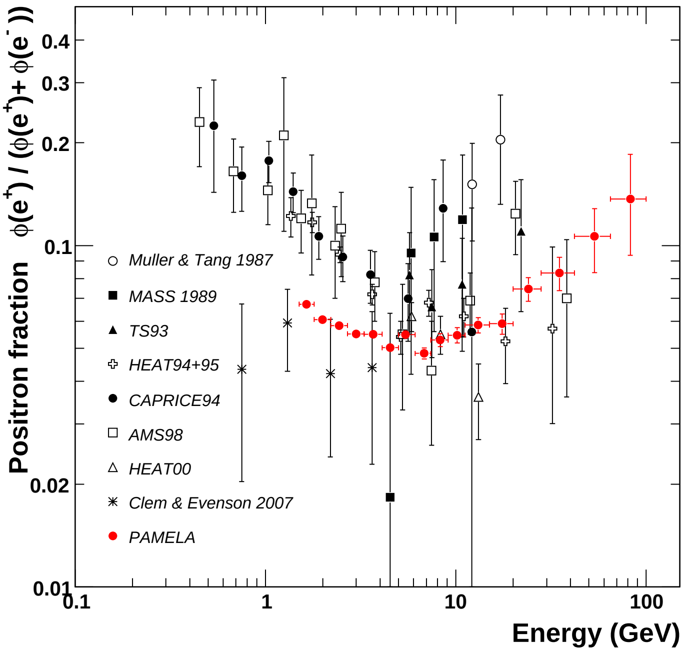

Figure 1.3: The positron fraction as function of energy, measured by various experiments. Taken from Adriani et al. (2008).

1.1.2 Nucleonic Cosmic Rays

Thee spectrum of nucleonic cosmic rays (Fig. 1.1) follows a pure powerlaw over a huge range of energies ($10^8 - 10^{20}$ eV, therefore the flux covers the enormous range of 32 decades) and contains only a few breaks: the so-called *knee* at 4×10^{15} eV, where the spectral index changes from 2.7 to 3.1, the *second knee* at 4×10^{17} eV, where the spectrum steepens to an index of 3.3, and the so-called *ankle* at $\approx 4 \times 10^{18}$ eV, where the spectrum hardens again with a spectral index of 2.7.

The wide range of fluxes and energies makes it obvious that different techniques are needed to measure cosmic rays. At low energies the large fluxes allow for small satellite and balloon measurements with sophisticated detector techniques like silicon detectors capable of resolving isotopes as implemented in the CRIS experiment (Stone et al. (1998)) for MeV energies, magnet spectrometers to identify particle and antiparticle like the BESS experiment (Ajima et al. (2000)) for GeV energies, and calorimeters and transition radiation detectors in the GeV to TeV range as used by the ATIC (Guzik (2008)), CREAM (Seo et al. (2004)) and TRACER (Gahbauer et al. (2004)) experiments. Beyond a few TeV/nucleon the fluxes of cosmic rays become too low for the small collection areas of the above mentioned experiments (≈ 1 m^2), and ground-based installations with their larger collection areas are needed. They measure the secondary products of the particle interactions in the atmosphere. In the TeV domain, ground-based experiments like H.E.S.S. (Hinton (2004)), MAGIC (Ferenc & MAGIC Collaboration (2006)) or VERITAS (Holder et al. (2006)) detect the Cherenkov radiation of secondary particles in the atmosphere or - like MILAGRO (Atkins et al. (2004)) - in water. Although all these experiments rather aim at the γ-ray component of cosmic rays, they can also be used for a measurement of charged cosmic rays (e.g. Aharonian et al. (2007b)). For the measurement of cosmic rays up to 10^{20} eV, huge ground-based detector arrays are needed. At energies above 10^{14} eV, secondary particles of the air shower reach the ground and are detected by scintillation detectors and calorimeters, as done by KASCADE (Antoni et al. (2003)). In addition, hybrid detectors use the fluorescence light emitted by nitrogen molecules that are excited by air-shower particles, used for instance in the AUGER experiment (Abraham et al. (2004)).

The origin of nucleonic cosmic rays up to the knee and second knee is thought to be Galactic. Beyond the second knee, cosmic rays are supposed to be extragalactic.

In the following Galactic cosmic rays at energies below the knee and second knee are discussed first, followed by a discussion of extragalactic cosmic rays and the energies beyond the second knee.

Measurements of the composition of cosmic rays have been performed with great accuracy in the MeV and GeV range. At higher energies the measurements are less and less reliable, with ground-based measurements being only sensitive to the logarithm of the mass number and always dependent on hadronic interaction models predicting the interaction of particles in the atmosphere[1]. At GeV energies, measurements show that cosmic rays consist primarily of protons ($\approx$87% of the nucleonic cosmic rays) and helium ($\approx$12%), but also of heavier nuclei in good agreement with the solar abundance (Simpson (1983)). This demonstrates that cosmic rays are regular matter, which is accelerated to high energies. The relative abundance of cosmic rays as function of nuclear charge number is shown in Fig. 1.4 in comparison with the solar abundance. Observed deviations from the solar abundance can be explained by spallation of heavy nuclei in the course of propagation. The

---

[1] For a discussion of hadronic interaction models see Chapter 2.1.

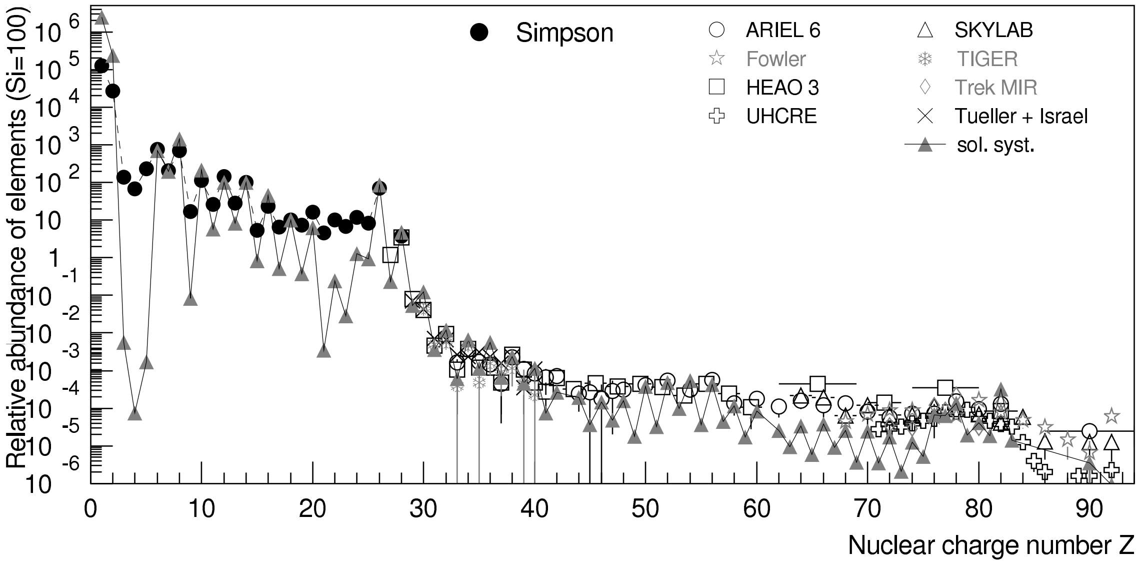

Figure 1.4: The relative abundance of cosmic rays as function of their charge number Z at energies arount 1 GeV/nucleon. The cosmic-ray composition is compared to the solar abundance visualised by grey triangles. Both distributions are normalised to a fixed value of 100 for Si. Taken from Hörandel (2008).

ratios of spallation products to their primaries (in particular the boron to carbon ratio) can be used to investigate the average amount of interstellar medium that the cosmic rays traverse, resulting in the conclusion that cosmic rays diffuse rather than propagate in straight lines (Yanasak et al. (2001), Garcia-Munoz et al. (1975)). If the produced secondaries are radioactive (as is the case for ^{10}Be for example), also the confinement time of cosmic rays in the Galaxy can be deduced to be $\tau_{\rm esc} = (15.0 \pm 1.6) \times 10^6$ years (Yanasak et al. (2001)). Concerning the sources of Galactic cosmic rays, Baade and Zwicky were in 1934 the first to link cosmic rays to supernovae (Baade & Zwicky (1934)). A simple energy budget argument makes this connection plausible: the energy density of cosmic rays in the Galaxy is $\rho_{cr} \approx 1$ eV/cm^3. If this is a stationary value, the power leaving the Galaxy volume V, $\rho_{cr}\, V/\tau_{esc} \approx 10^{41}$ erg/s, has to be sustained by a mechanism accelerating cosmic rays to their high energies. With the rate of supernovae in the Galaxy per year of 1/30, and a typical supernova releasing $\approx 10^{51}$ erg of kinetic energy, only $\approx$10% of this kinetic energy is needed to maintain the cosmic-ray energy density.

The mechanism thought to be responsible for the acceleration is diffusive shock acceleration in the shock fronts of supernova remnants (SNRs). Attractive feature of this mechanism is that it naturally produces an energy spectrum following a powerlaw with the approximately right spectral index if taking into account diffusion of the particles from the source to the Earth. However, so far there has been no clear experimental evidence for the acceleration of hadrons in SNRs, while for electrons radio, X-ray and γ observations see evidence for their acceleration in these objects (Koyama et al. (1995), Aharonian et al. (2004b)). Main difficulty of cosmic-ray acceleration in SNRs is the fact that with typical Galactic magnetic field values of $\approx 5\ \mu$G, the acceleration process is too inefficient to accelerate particles in the lifetime of a SNR shock front to energies larger than $E_{\rm max} \approx 10^5 \cdot Z$ GeV, with Z being the nuclear charge number (Lagage & Cesarsky (1983)). Considerable effort has been made to explain the knee and second knee structure in the cosmic-ray spectrum with the cutoff due to this maximum energy. But only taking into account magnetic field amplification (Berezhko & Völk (2004), Vink (2003)), the knee can result naturally from the cutoff of the proton component and the successive drop-out of the heavier nuclei up to the cutoff of iron at the second knee, an idea that is supported by the increase of mean mass with energy in this region. For a review on models explaining the knee see Hörandel (2004).

As the Galactic component can reach at most up to the second knee, an extragalactic component is needed to explain the continuation of the spectrum up to 10^{20} eV. These extragalactic cosmic rays might be related to active galactic nuclei (AGN). Composition measurements, which could facilitate the interpretation of the cosmic-ray spectrum, are intrinsically difficult at these energies.

Regarding the processes at ultra-high energies, photodisintegration is the dominant energy loss for heavier nuclei, while there are two processes that reduce the flux of extragalactic protons at ultra-high energies: They interact with the cosmic microwave background (CMB) and either create electron-positron pairs, $p\,\gamma_{\mathrm{CMB}} \rightarrow p\,e^+\,e^-$, which is thought to cause the dip in extragalactic cosmic rays formed by the ankle (Berezinsky (2006)), or produce pions, $p\,\gamma_{\mathrm{CMB}} \rightarrow p\,\pi^0$ or $p\,\gamma_{\mathrm{CMB}} \rightarrow n\,\pi^+$, which is expected to suppress the flux above the threshold of 6×10^{19} eV, the so called GZK cutoff (after Kenneth Greisen, Vadim Kuzmin and Georgiy Zatsepin).

1.2 Energy Losses and Local Sources

The main difference between nucleonic cosmic rays and cosmic-ray electrons are the strong energy losses that electrons suffer when traversing matter, radiation fields and magnetic fields. These energy losses cause the comparatively steeper energy spectrum and limit the possible sources of the locally measured energetic cosmic-ray electrons.

1.2.1 Propagation and Energy Losses

The energy losses of cosmic-ray electrons can be expressed as

$$-\frac{dE}{dt} = A_1(\ln\frac{E}{m_e c^2} + 19.8) + A_2 E + A_3 E^2 \ , \tag{1.1}$$

where the term with constant A_1 describes ionisation losses, the term with A_2 bremsstrahlung and adiabatic losses, and the A_3 term inverse Compton scattering and synchrotron radiation. Energy losses caused by ionising the traversed material and deceleration of electrons in matter by the emission of bremsstrahlung are relevant only at low energies. While adiabatic cooling of electrons in an expanding volume becomes important in expanding sources such as supernova remnants, starting in the GeV range the dominant processes are typically the emission of synchrotron radiation in interstellar magnetic fields and inverse Compton scattering, where energy is transferred from a high-energy electron to a low-energy photon. For the inverse Compton scattering, the E^2 dependence is only an approximation. For high enough photon energies (for TeV electrons, this means photon energies of 1 eV and higher, i.e. in the range of optical emission), the Klein-Nishina effect has to be taken into account. The Klein-Nishina effect reduces the cross-section for the case that the photon energy is comparable or larger than the electron rest mass in the centre of momentum frame. This effect is neglected here as it does not have a big impact on the results. For a treatment of the Klein-Nishina effect see the calculations of Kobayashi et al. (2004).

Since the energy threshold of the H.E.S.S. experiment is at ≈100 GeV, for this work, the high-energy part of the cosmic-ray electron spectrum is the most relevant. Therefore in the following discussion the focus will be set on the two processes of inverse Compton scattering and synchrotron radiation and the behaviour of cosmic-ray electrons at high energies. Calculations are based on the work of Atoyan et al. (1995), Aharonian et al. (1995), and Müller (2001).

Above several GeV, the radiative losses due to inverse Compton scattering and synchrotron radiation dominate and the energy loss equation can be simplified to

$$-\frac{dE}{dt} = \frac{4\,\sigma_T\,c}{3(m_e c^2)^2} E^2 \left(\frac{B^2}{8\pi} + w_{\mathrm{ph}}\right) \equiv \beta E^2 \equiv b(E) \ , \tag{1.2}$$

where $\sigma_T = 6.65 \times 10^{-25}$ cm^2 is the Thomson cross section, w_{ph} the photon energy density and B the magnetic field strength. A convenient way to write this is

$$-\frac{dE}{dt} \bigg/ \left(1\,\frac{\mathrm{GeV}}{\mathrm{s}}\right) = 6.25 \times 10^{-17} \left(\frac{E}{1\,\mathrm{GeV}}\right)^2 \left(\frac{w_B}{1\,\mathrm{eV/cm^3}} + \frac{w_{\mathrm{ph}}}{1\,\mathrm{eV/cm^3}}\right) \ . \tag{1.3}$$

The energy density of the magnetic field for a typical magnetic field of $5\,\mu$G is $w_B \simeq$ 0.6 eV/cm^3, the photon energy density w_{ph} consists of contributions of the cosmic microwave background ($w_{\mathrm{CMB}} \simeq 0.25$ eV/cm^3), of thermal dust emission in the infrared ($w_{\mathrm{inf}} \simeq 0.2$ eV/cm^3), and of star light emitting in the optical ($w_{\mathrm{opt}} \simeq 0.45$). A total energy density of $w_B + w_{\mathrm{ph}} \simeq 1$ eV/cm^3 is assumed.

Due to radiative cooling, an electron of initial energy E_0 is, after a time t, left with an energy

$$E(t) = \frac{1}{1/E_0 + \beta\,t} \ , \tag{1.4}$$

where β is defined in Eqn. (1.2). This equation demonstrates that within the time $\tau \approx 1/\beta E$ an electron of arbitrarily high energy E_0 is cooled down to an energy E. Even more important, the maximum energy at a time t after injection of the electron into the interstellar medium is $E_{\mathrm{max}} \approx 1/\beta t$. This radiative lifetime is shown in Fig. 1.5. It can be seen that 1 TeV electrons have a lifetime of not more than 5×10^5 yr.

This small lifetime sets strict limitations to the sources that have accelerated these electrons.

Local Sources

As sources of cosmic-ray electrons, SNRs and pulsars are discussed. Only few SNRs and pulsars come into consideration as sources of electrons measured at TeV energies at Earth. Sources contributing to the cosmic-ray electron spectrum in the TeV domain have to be young in the sense that injection of the particle in the ISM must have occurred recently, and have to be close since particles can diffuse only a distance $\lambda \simeq 2\sqrt{D\tau}$ (Atoyan et al. (1995)) before they lose their energy. For a diffusion coefficient[2] D of $\sim 10^{29}$ cm^2/s, this is

---

[2] Note that the diffusion coefficient is not very well known.

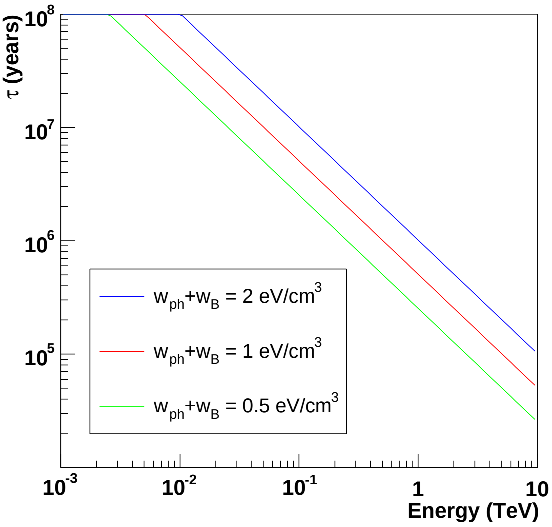

Figure 1.5: Radiative lifetime as function of energy for three different total energy densities $w_{\mathrm{ph}} + w_B = 0.5,\ 1,\ 2\ \mathrm{eV/cm}^3$.

a distance $\lambda \approx 800$ pc. The condition on the distance is true only on average; for a very strong source there is still the possibility to see particles of the tail of the λ distribution reaching us. Table 3.5 summarises the known pulsars and SNRs that are closer than 1 kpc and younger than 5×10^5 yr and can possibly contribute to the TeV electron spectrum. At some energy this component will drop out due to the lack of accelerators close enough to Earth and the secondary electrons will be the only remaining component.

Another consequence of local sources is the expectation of anisotropy in the electron flux. The anisotropy parameter Δ_i is defined as

$$\Delta_i = \frac{I_{\max} - I_{\min}}{I_{\max} + I_{\min}} = \frac{3D}{c}\frac{\nabla N_i}{N_i} = \frac{3r_i}{2ct_i}\ , \tag{1.5}$$

where $I_{\max}$ and $I_{\min}$ are the maximum and minimum intensity in all directions, N_i is the contribution to the local cosmic-ray electron intensity of a source i at a distance r_i and with an age t_i (Mao & Shen (1972)). However, the expected anisotropies (13% for the Vela SNR, Kobayashi et al. (2004)) are too small to be observed within the systematic uncertainties of this measurement[3].

Possible mechanisms that give cosmic-ray electrons their high energies are discussed in the following.

---

[3] The systematic uncertainties are discussed in Chapter 3.6.

Source name	Distance (kpc)	Age (years)	Common names
Pulsars:			
J0633+1746 (1)	0.16	3.42×10^5	Geminga
J0835-4510 (1)	0.29	1.13×10^4	Vela Pulsar
J0659+1414 (1)	0.29	1.11×10^5	Monogem
J1825-0935 (1)	1.00	2.33×10^5	
SNRs:			
Loop I (2)	0.17	2×10^5	
Monogem-Ring (3)	0.3	8.6×10^4	
G263.9-3.3 (4,5)	0.3	1.13×10^4	Vela SNR
G266.2-1.2 (4,6)	0.33	660	RXJ0852.0-4622/Vela Jr.
G180.0-1.7 (4,7)	0.36-0.88	$(3 \pm 0.4) \times 10^4$	S147
G74.0-8.5 (4,8)	0.44	$(5 - 10) \times 10^3$	Cygnus Loop
G114.3+0.3 (4,9)	0.7	7.7×10^3	
G65.3+5.7 (4,10)	0.8	4.5×10^5	
G89.0+4.7 (4,11)	0.8	$(8 - 15) \times 10^3$	HB21

Table 1.1: List of nearby and young SNRs and pulsars (distance < 1 kpc and age $< 5 \times 10^5$ yr).

1.2.2 Sources of Cosmic-Ray Electrons

When talking of the origin of cosmic-ray electrons, generally two cases are distinguished: a primary and a secondary origin. Primary cosmic-ray electrons are accelerated in astrophysical objects. X-ray observations have shown that electrons with energies up to ~100 TeV exist in the shock fronts of supernova remnants as well as in pulsar wind nebulae, which makes them good candidates for electron accelerators. Also a dark matter origin of cosmic-ray electrons has been discussed (e.g. Cholis et al. (2008)).

Secondary cosmic-ray electrons are produced in interactions of cosmic-ray protons with protons of the ISM:

$$pp \longrightarrow \pi^{+/-} X\,, \;\; \pi^{+/-} \longrightarrow \mu^{+/-} \overset{(-)}{\nu_e}\,, \;\; \mu^{+/-} \longrightarrow e^{+/-} \overset{(-)}{\nu_e} \overset{(-)}{\nu_\mu}\,, \tag{1.6}$$

---

[1] found in the ATNF Pulsar Catalogue, available at http://www.atnf.csiro.au/research/pulsar/psrcat, Manchester et al. (2005)

[2] Egger & Aschenbach (1995)

[3] Plucinsky et al. (1996)

[4] found in the Green Catalogue of Galactic Supernova Remnants, available at http://www.mrao.cam.ac.uk/surveys/snrs/, Green (2006)

[5] Large et al. (1968)

[6] Bamba et al. (2005)

[7] Kramer et al. (2003)

[8] Katsuda & Tsunemi (2008)

[9] Yar-Uyaniker et al. (2004)

[10] Gull et al. (1977)

[11] Leahy (1987)

a mechanism which shows a slight preference for positrons due to the charge asymmetry in the cosmic rays and the ISM (Dario Serpico (2008)). For a discussion of the spectrum of secondary cosmic-ray electrons see Delahaye et al. (2008).
While other ideas on the origin of cosmic-ray electrons exist in the literature (e.g. magnetic reconnection), the SNR, pulsar, and dark matter scenario will be discussed further in the following.

Diffusive Shock Acceleration in Supernova Remnants

In a supernova explosion the outer shell of the exploding star is ejected and expands supersonically as a shock front (free expansion phase). It sweeps up the interstellar medium (ISM) with constant velocity of ≈10000 km/s until the mass of the stellar injection reaches the swept up mass. At this point, the wave starts to slow down (Sedov-Taylor phase). These two phases are the relevant ones for particle acceleration since they involve a strong shock travelling through the ISM. After $\approx 10^4$ yr, the temperature falls below 10^6 K and electrons recombine with heavy element ions under UV line emission. This radiative cooling becomes the dominant energy loss mechanism (hence this phase is called radiation phase) and cools the remnant for about 10^5 yr until the remnant finally disperses into the surrounding medium.
The mechanism thought to be responsible for the acceleration in the free expansion and Sedov-Taylor phases of SNR evolution is the diffusive shock acceleration, which is based on an idea of Fermi (Fermi (1949)). But Fermi only considered stochastically moving magnetic mirrors of very low velocity, resulting in a very inefficient acceleration process, where the energy gain is proportional to $(v/c)^2$ with v being the velocity of the magnetic mirrors. Diffusive shock acceleration, which was independently developed by Axford et al. (1978), Krymskii (1977), Bell (1978), and Blandford & Ostriker (1978), introduces with the existence of a shock front higher velocities and a preferred, unique direction resulting in an energy gain of first order in v/c.

If the shock front of an expanding SNR shell moves supersonically through the ISM with a shock velocity of v, a sharp discontinuity is formed at the position of the shock. A particle with high enough energy (for a discussion of the injection problem see Malkov & O'C Drury (2001)) gets accelerated when crossing the shock front: After the crossing, the particle gets scattered collisionlessly at magnetic inhomogeneities (elastic in the rest frame of the scattering centres). They are produced downstream by the turbulences caused by the shock front, and upstream by the streaming instabilities due to the relativistic particles themselves. Multiple scattering of the particles yields an isotropisation of the particle in the rest frame of the material. Thereby, the particle gets accelerated due to the adaptation of the particle's net momentum to the bulk velocity of the medium. This situation is completely symmetric in both directions, therefore the particle gains energy in every crossing.
In order to obtain a powerlaw in the energy spectrum as observed in cosmic rays, only two conditions have to be fulfilled: the increase in energy in each cycle has to be proportional to E and the probability to stay in the shock region has to be a constant. Simple calculations result in a spectral index of 2 for the case of a strong shock (the Mach number $M \rightarrow \infty$), which is close to the value expected from the shape of the cosmic-ray spectrum if taking into account energy dependent diffusion.
In this approach, several approximations are involved: particles move without influencing

each other and the plasma (test particle approximation) and much faster than the plasma, scattering occurs elastically and energy losses are neglected. Modelling of a more realistic scenario includes relaxing these conditions; for a review see Drury (1983). The case of relativistic shock speeds is discussed in Achterberg et al. (2001).

In the model of diffusive shock acceleration in SNRs, regular matter is accelerated, which in the case of electrons are negative electrons. The electron source spectrum can be determined with radio observations of typical SNRs like Cas A, Kepler, SN 1006 or RCW 86. The radio emission has a spectral index of $\alpha \approx 0.6$. If this emission is produced by synchrotron radiation of electrons, their source spectrum can be deduced to have typical spectral indices of $2.2 (= 2\alpha + 1)$ (Allen (1999)). X-ray measurements of SN 1006 (Koyama et al. (1995)) have shown that in SNRs electrons are accelerated to ≈100 TeV. Also the total energy of one SNR going in cosmic-ray electrons above 1 GeV can be estimated to $\approx 10^{48}$ erg (Kobayashi et al. (2004)).

Particle Acceleration in Pulsar Magnetospheres

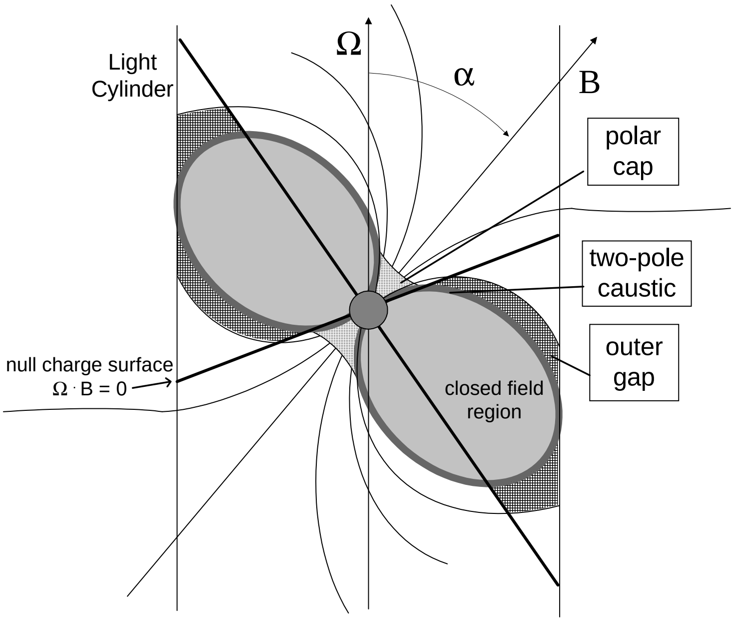

Figure 1.6: Schematic drawing of the geometry of a pulsar with angular velocity Ω and magnetic field B. The emission regions in polar cap and outer gap models are marked. Taken from Kaspi et al. (2004).

Another potential source of high-energy cosmic-ray electrons are pulsars. Pulsars are rapidly rotating neutron stars that form after supernova explosions of stars with masses between 1.44 and 5 solar masses. They possess extremely high magnetic fields of the order of $10^{10} - 10^{13}$ G, possibly the strongest that exist in the Universe. The rotation of these high magnetic fields induces strong electric fields that can accelerate particles. For details refer to Manchester & Taylor (1977), and Kaspi et al. (2004).

Pulsars are surrounded by a magnetosphere of charged particles pulled out of the pulsar surface by electric fields, with a charge density of $\rho_{\mathrm{GJ}} \simeq \omega \cdot \mathbf{B}/2\pi c$ (the so called Goldreich-Julian charge density, Goldreich & Julian (1969)), where ω is the angular velocity of the pulsar. The magnetosphere co-rotates with the pulsar. At large distances from the pulsar, this co-rotation is limited by particle inertia and cannot persist beyond the surface where the velocity reaches the speed of light, the *light cylinder*. Magnetic field lines within the light cylinder are closed, magnetic field lines crossing it are open. Since particles gyrate along the magnetic field lines, they can escape the pulsar magnetosphere only along open field lines. Particles gain energy if the generated electric fields have a non-vanishing component parallel to the magnetic field: $\mathbf{E} \cdot \mathbf{B} \neq 0$. Normally, this $E_{\|} = 0$ due to screening of free electric charges in the magnetosphere. There are two different classes of models of electrostatic acceleration in pulsar magnetospheres differing in the regions where $E_{\|} \neq 0$ occurs: In polar cap models acceleration and radiation occurs in charge depleted zones near the polar caps of the pulsar. In outer gap models, acceleration takes place in vacuum gaps that form in the outer magnetosphere along the last open field line in the vicinity of the null charge surface $\omega \cdot \mathbf{B} = 0$ where the Goldreich-Julian charge density changes sign. The regions of the two models are shown in a schematic drawing of the pulsar in Fig. 1.6. If $E_{\|} \neq 0$, a cascading mechanism increases the number of energetic particles: γ rays, which are produced by synchrotron radiation, move in the strong magnetic fields and produce e^+e^- pairs. The secondary particles get accelerated as well and a cascade is initiated. For the Crab pulsar, calculated values are 10^7 e^+e^- pairs created for each primary electron, which yields a total of 10^{40} particles per second.

The energetic particles produced by this cascading mechanism form the pulsar wind nebula (PWN), which expands in the ambient medium. It is in the outer regions confronted with the expanding shell of the SNR and a termination shock is formed. At this termination shock, shock acceleration can occur as discussed previously for SNRs, and electrons are reaccelerated. In this case, however, the shock moves with relativistic speed and therefore, the energy gain per crossing is much larger, while the probability to return to the shock is low.

The details of particle acceleration in pulsars beyond this simple picture are still very much under debate.

In contrast to shock acceleration in SNRs, in pulsars, both negative electrons and positrons are accelerated.

Dark Matter

Another potential source of both, negative electrons and positrons is the annihilation of dark matter. Weakly interacting particles that are proposed by Supersymmetry (like neutralinos) or theories of extra dimensions (like the Kaluza-Klein particle) can annihilate via the production of e^+e^- pairs or γ rays (Chang et al. (2008)). For neutralinos the e^+e^- channel is chirality suppressed (because of their Majorana nature), resulting in a broad spectrum. The direct production of e^+e^- pairs by Kaluza-Klein particles yields a spectrum of a delta function at the particle's mass, which is broadened to lower energies due to propagation effects. Fig. 1.7 shows the contributions to the cosmic-ray positron flux calculated by Cheng et al. (2002) for the case of Kaluza-Klein dark matter for different

dark matter masses. The sharp peak at the energy of the dark matter mass leaves a very peculiar feature in the spectrum.
The bump observed by the ATIC experiment has been interpreted as signature of Kaluza-Klein dark matter of a mass of 620 GeV (Chang et al. (2008)). In order to be consistent with measurements of the Wilkinson Microwave Anisotropy Probe (WMAP), which observed a "haze" in the inner region of the Galaxy, which could be a product of dark matter annhihilation, the large ATIC signal can only be explained by introducing a large "boost factor", i.e. a substantial enhancement of the dark matter density close to our Solar System.

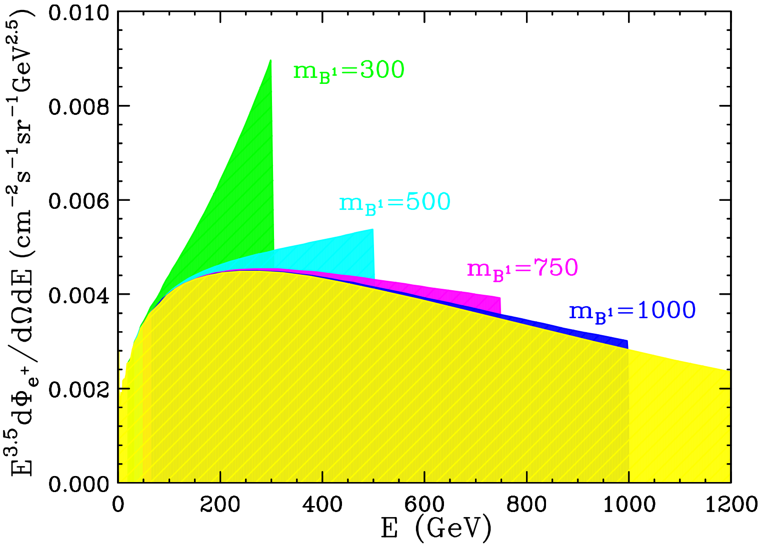

Figure 1.7: Predicted positron signals of Kaluza-Klein dark matter with masses of 300, 500, 750, and 1000 GeV. Taken from Cheng et al. (2002).

1.3 Modelling the Electron Spectrum

In this section the efforts of calculating the energy spectrum of cosmic-ray electrons under various model assumptions are summarised.
Because of the short timescales involved in the range of very high energies, the use of a continuous source distribution is not valid and single nearby and young sources can contribute significantly to the TeV electron spectrum. This was first pointed out by Shen (1970), who already discussed Vela as a possible local accelerator, based on calculations of Berkey & Shen (1969).
The cosmic-ray electron spectrum can be modelled by summing over distant (> 1 kpc, assumed to be homogeneously distributed) and a few nearby sources that dominate the spectrum at higher energies.
An analytical solution to the diffusion equation

$$\frac{\partial f}{\partial t} = \frac{D}{r^2}\frac{\partial}{\partial r}r^2\frac{\partial f}{\partial r} + \frac{\partial}{\partial E}\left(b(E)\,f\right) + Q \tag{1.7}$$

has been calculated by Atoyan et al. (1995) for the case of burst-like injection:

$$Q(E,t) = Q(E)\,\delta(t) = Q_0 \times E^{-\alpha}\,\delta(t)\ . \tag{1.8}$$

The cosmic-ray electron density at a distance r from the source at a time t after the release of the electrons into the ISM is

$$f_e(r,t,E) = \frac{Q(\frac{E}{1-\beta\,t\,E})}{\pi^{3/2} r_{\mathrm{diff}}^3}\,(1-\beta t E)^{-2}\, e^{-(r/r_{\mathrm{diff}})^2}\ , \tag{1.9}$$

where $E < E_{\mathrm{max}} = 1/\beta t$ (otherwise $f_e = 0$). This solution contains the Eqn. (1.9) to express the initial energy E_0 of the electrons in terms of the energy E measured at Earth ($E_0 = \frac{E}{1-\beta\,t\,E}$). The diffusion radius

$$r_{\mathrm{diff}}(E,t) \simeq 2\sqrt{D(E)\,t\,\frac{1-(1-E/E_{\mathrm{max}})^{1-\delta}}{(1-\delta)\,E/E_{\mathrm{max}}}} \tag{1.10}$$

is the radius of the sphere up to which electrons of energy E effectively propagate during the time t after their injection into the ISM. For energies $E \leq 0.5\,E_{\mathrm{max}}$, the diffusion radius simplifies to $r_{\mathrm{diff}} = 2\sqrt{D(E)t}$.
For the case of continuous injection of electrons from a point source, the electron spectrum is qualitatively different. At high energies the spectrum is steeper and also the cutoff at E_{max} disappears (Atoyan et al. (1995)). A diffusion coefficient of the form $D(E) = D_0(1 + E/E_*)^\delta$ is assumed to allow for a gradual change between a constant diffusion coefficient at energies much smaller than E_* and a powerlaw behaviour at energies $E \sim E_*$. Typically, it is believed that $E_* \approx 1 - 10$ GeV and $\delta \approx 0.5 - 0.6$. With this diffusion coefficient the contributions of single sources can be evaluated as is done in Fig. 1.8. Shown are the contributions of a source at fixed distance with varying times after injection and

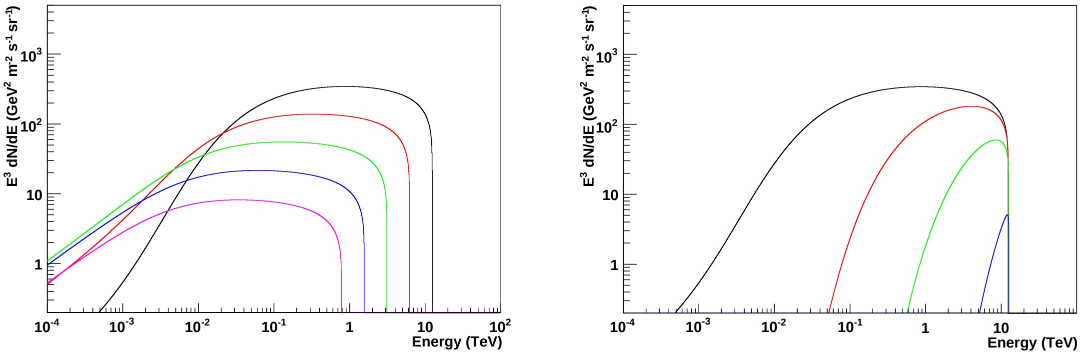

Figure 1.8: Contributions of single sources to the electron spectrum. Assumed are D(10 GeV) = 10^{28} cm^2/s, $\delta = 0.6$, $E_* = 3$ GeV, and an energy output of 10^{48} erg in powerlaw primary electrons between 0.5 GeV and 100 TeV with spectral index of 2.2. *Left*: at a distance of 100 pc, at times of 2.5×10^4 (black), 5×10^4 (red), 1×10^5 (green), 2×10^5 (blue), 4×10^5 (pink) years after injection. *Right*: 2.5×10^4 yr after injection, at distances of 100 (black), 250 (red), 500 (green) and 1000 pc (blue).

at fixed injection time, with variations of the distance. The variation of the injection time shows the time-dependent losses at high energies, the variation of the distance the reduction in flux because only few high-energy particles diffuse fast enough to reach Earth. Young and nearby sources can thus leave an individual imprint on the spectrum of very-high-energy cosmic-ray electrons.

Aharonian et al. (1995) use Eqn. (1.9) to separate contributions of distant and nearby sources and discuss a contribution of the Geminga pulsar to the local cosmic-ray electron spectrum.

Kobayashi et al. (2004) modify Eqn. (1.9) by an exponential cutoff in the source spectrum,

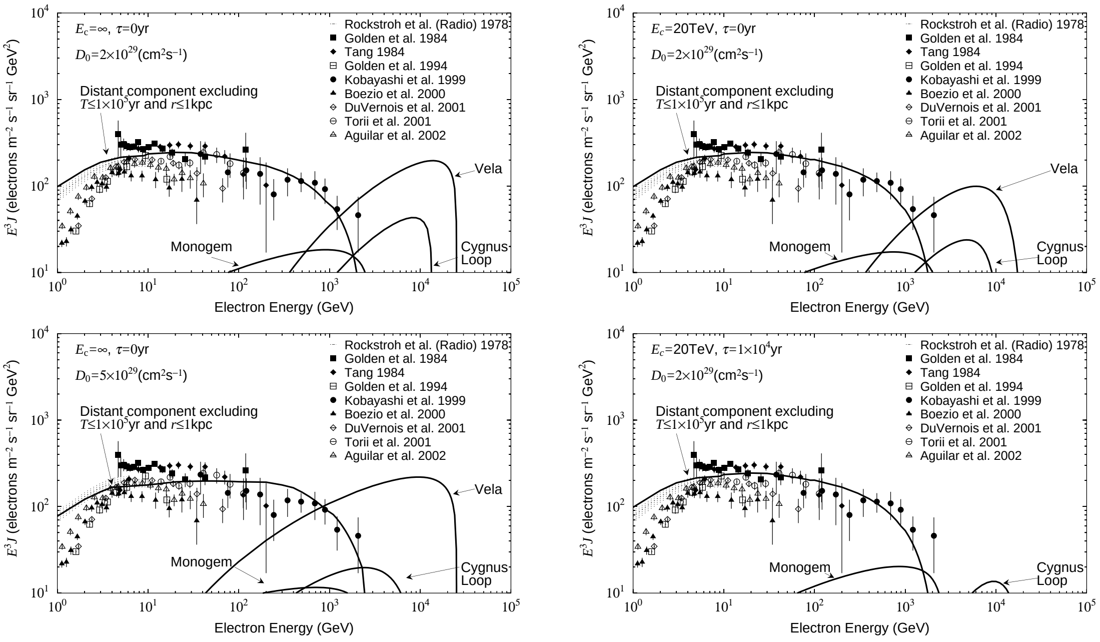

Figure 1.9: Calculated electron spectrum with single source contributions. Taken from Kobayashi et al. (2004). The contributions of the Vela SNR, Monogem and Cygnus Loop are shown. *Top left*: With prompt release after explosion, no cutoff in the injection spectrum and a diffusion coefficient of $D_0 = 2 \times 10^{29}$ cm^2 s^{-1}. *Top right*: The same conditions as the left panel but with a cutoff energy of $E_c = 20$ TeV. *Bottom left*: The same conditions as in the top left panel but with a diffusion coefficient of $D_0 = 5 \times 10^{29}$ cm^2 s^{-1}. *Bottom right*: The same conditions as in the top right panel, but with a delay of the release time of 10^4 yr.

$$Q(E,t) = Q(E)\,\delta(t) = Q_0 \times E^{-\alpha} \exp\left(\frac{E}{E_c}\right)\delta(t)\ , \tag{1.11}$$

and apply this to known, observed SNRs. Depending on diffusion coefficient, cutoff energy and release time they obtain differently pronounced contributions from Vela, Monogem and Cygnus Loop, which are displayed exemplarily for special choices of parameters in Fig. 1.9. The different scenarios illustrate the big impact of variations in diffusion coefficient and release time from the SNR on the calculated spectrum of cosmic-ray electrons. The Vela SNR has with its 300 pc distance assumed by Kobayashi et al. (2004) always significant contributions to the TeV spectrum, except for the case of a delayed release of the electrons from the remnant, in which case the electrons of the very young Vela SNR are still confined in the remnant.

Recent ATIC and PAMELA data have been interpreted in terms of a pulsar contribution or dark matter annihilation. Model calculations for local pulsars have been done by Büsching et al. (2008), Hooper et al. (2008), and Profumo (2008), for example. The calculations of Profumo (2008) for the Geminga, Monogem, Vela, and B0355+54 pulsars are shown in Fig. 1.10.
A dark matter origin has been discussed by e.g. Zhang et al. (2008) and Cholis et al. (2008). A comparison of dark matter and pulsar models for the features in the positron fraction and in the electron spectrum was done by Zhang et al. (2008) and is shown in Fig. 1.11. Dark matter and pulsar models provide a similarly good description of the data and a distinction between the models based on the available data is not possible.

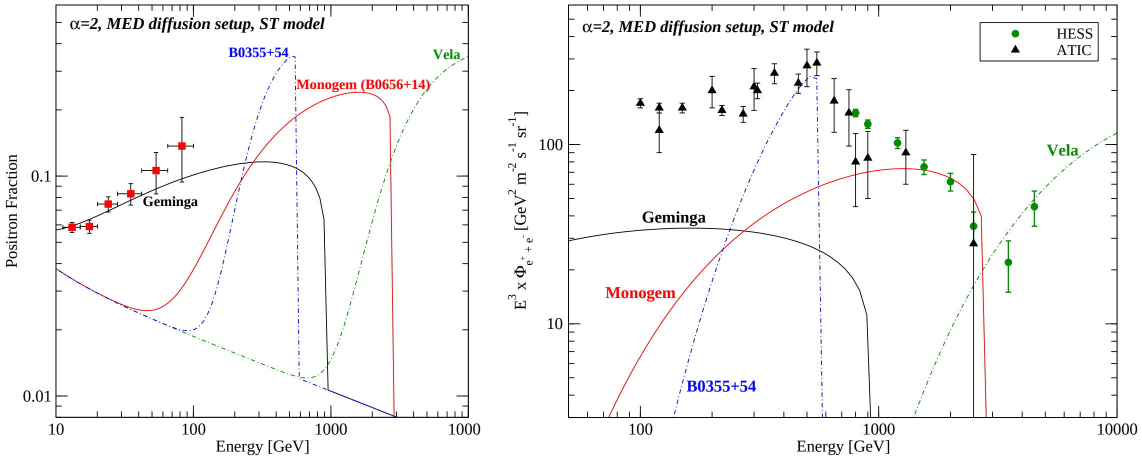

Figure 1.10: Contributions of local pulsars to the positron fraction (left panel) and the electron spectrum (right panel). Adapted from Profumo (2008).

Various other authors have also modelled the cosmic-ray electron spectrum. In order to explain the EGRET “GeV excess”, Pohl & Esposito (1998) argue that the local electron spectrum differs from the average over the Galaxy. They model electron spectra by randomly generating SNR distributions and summing up the individual contributions. Another simulation of the cosmic-ray electron spectrum was done by Erlykin & Wolfendale (2002), who modified a model for acceleration and propagation of hadronic cosmic rays (Erlykin & Wolfendale (2001)) to describe cosmic-ray electrons. Their model includes particle acceleration in SNRs throughout the lifetime of the remnant, random distribution of SN in the local part of the Galaxy and diffusion to Earth if the Sun is outside the remnant. In yet another approach, Komori (2006) includes the source region in the calculation by

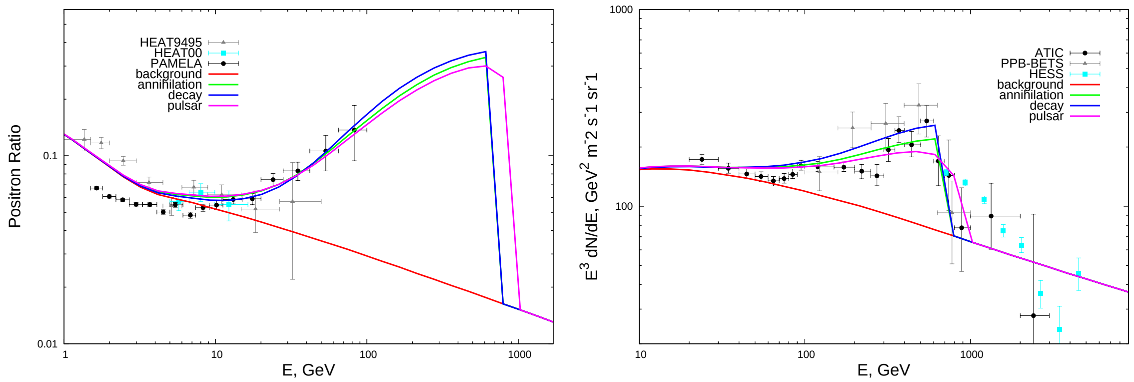

Figure 1.11: Calculations for dark matter and pulsar contributions to the positron fraction (left panel) and the electron spectrum (right panel). Taken from Zhang et al. (2008).

treating it as a leaky box with an estimation of the electron escape time in SNRs from the ratio of the radio flux in SNRs to the background flux in the Galaxy.

To summarise, the cosmic-ray electron spectrum beyond a few GeV is variable. For modelling the spectral shape especially in the TeV range, the distribution of sources in our local neighbourhood has to be known as well as their injection history, and the parameters of diffusion. Without detailed knowledge of these parameters, the spectrum of cosmic-ray electrons in the TeV cannot be predicted. Vice versa, the measurement of the electron spectrum can help to determine source and diffusion parameters. This makes the study of TeV electrons such an interesting topic.

1.4 The Backgrounds: Diffuse γ Rays

For the determination of TeV cosmic-ray electrons from ground, the background of diffuse γ rays needs to be evaluated, since the air showers of γ rays are almost indistinguishable from electron air showers and therefore diffuse γ rays make an almost irreducible background to the measurement of TeV electrons from ground.

1.4.1 Extragalactic Diffuse γ Rays

The determination of the extragalactic diffuse γ-ray background (EGRB) depends on the model assumed for the Galactic diffuse γ rays, which itself is not very well known. Moskalenko et al. (2004) discuss that the EGRB might consist of γ-ray emission of faint sources below the detection threshold. Among these sources AGN contribute significantly, but also contributions from galaxy clusters and faint γ-ray bursts are considered. Thompson et al. (2007) discuss a contribution by star-burst galaxies, which explains about 10% of the EGRET-measured flux and has a spectrum close to E^{-2}.
The spectrum of the EGRB is displayed in Fig. 1.12. The EGRET data are shown in two different interpretations (Sreekumar et al. (1998) and Strong et al. (2004)) differing in the choice of the model used for the evaluation of the Galactic diffuse emission.

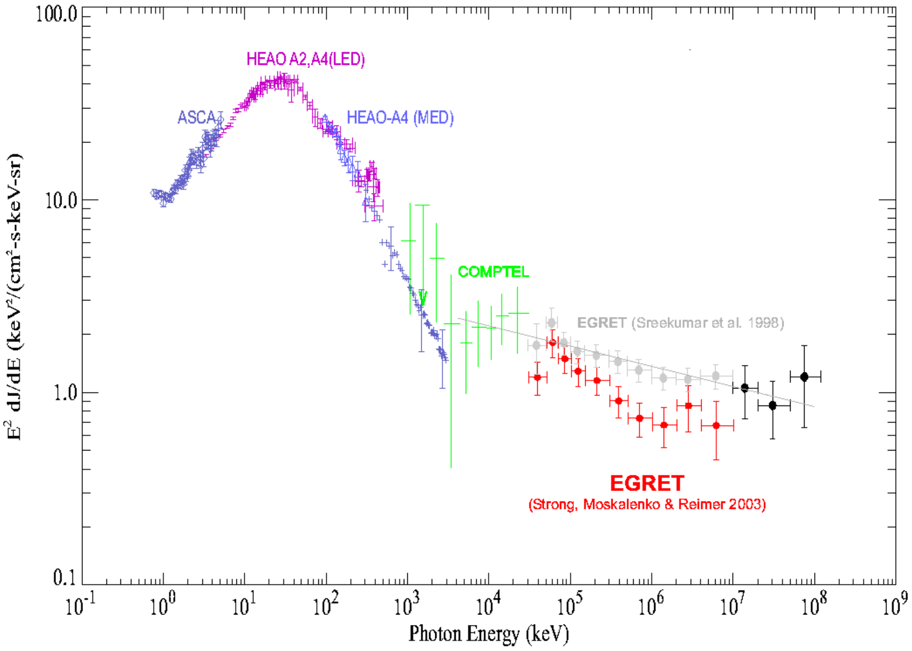

Figure 1.12: Spectrum of extragalactic diffuse γ rays. Taken from Moskalenko et al. (2004).

Sreekumar et al. (1998) apply the model presented by Hunter et al. (1997), and derive a powerlaw of $\phi = 2.7 \cdot 10^{-3} E^{-2.1}$ cm^{-2} s^{-1} sr^{-1} MeV^{-1} (solid grey line in Fig. 1.12). Strong et al. (2004) use the GALPROP code with an adjustment to account for the EGRET GeV excess and obtain a similar flux at 100 MeV and a somewhat steeper spectrum (a spectral index of -2.3) with a positive curvature and flattening of the spectrum above 1 GeV. A similar spectrum is obtained by Grenier et al. (2005) by including cold dark gas in the modelling, which is seen in the infrared. The GeV excess, however, which forced the modification of the model used for the diffuse Galactic emission by Strong et al. (2004), is not beyond dispute. de Boer et al. (2007) interpret it in terms of dark matter annihilation and include this into their model of the Galactic diffuse emission to arrive at an EGRB spectrum similar to Strong et al. (2004). Stecker et al. (2008) argue that the GeV excess is an instrumental effect arising from calibration uncertainties, and with an empirical correction they find a flux consistent with the original determination of Sreekumar et al. (1998). In the critical range for the electron measurement, beyond ≈100 GeV, no measurements exist yet. While in the GeV the EGRB flux lies orders of magnitude below the flux of cosmic-ray electrons (see Fig. 1.13 for a comparison), a continuation of the $E^{-2.1}$ powerlaw fitted to the data of Sreekumar et al. (1998) to TeV energies gives a flux which is of the same order as the cosmic-ray electron spectrum. However, extragalactic absorption due to electron-positron pair production on the cosmic microwave background should cause spectra of extragalactic γ rays to drop sharply at energies around 100 GeV and 1 TeV (Coppi & Aharonian (1997), Kneiske (2007), Kneiske & Mannheim (2008)).

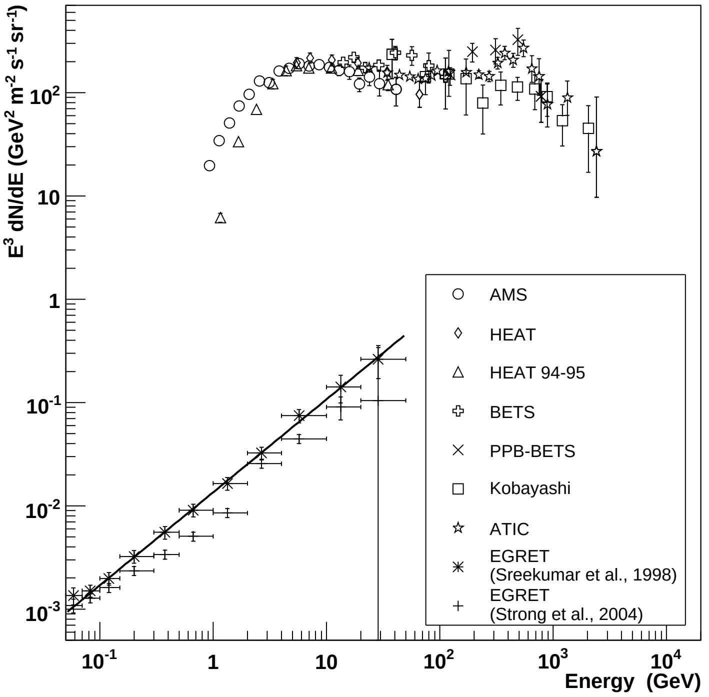

Figure 1.13: Comparison of EGRET measurements of the diffuse extragalactic γ rays and the flux of cosmic-ray electrons.

1.4.2 Solar-System γ Rays

Another potential background for the electron analysis are solar-system γ rays. In the radiation field of the Sun high-energy cosmic-ray electrons undergo inverse Compton scattering and produce energetic γ rays (Moskalenko & Porter (2006), Orlando & Strong (2007)). Therefore, the heliosphere is a diffuse source of γ rays. However, the intensities expected from these solar-system γ rays are calculated to be strongly dependent on the angular distance from the Sun (see Fig. 1.14). As H.E.S.S. observations are always performed by pointing in the opposite direction of the Sun, this background is negligible.

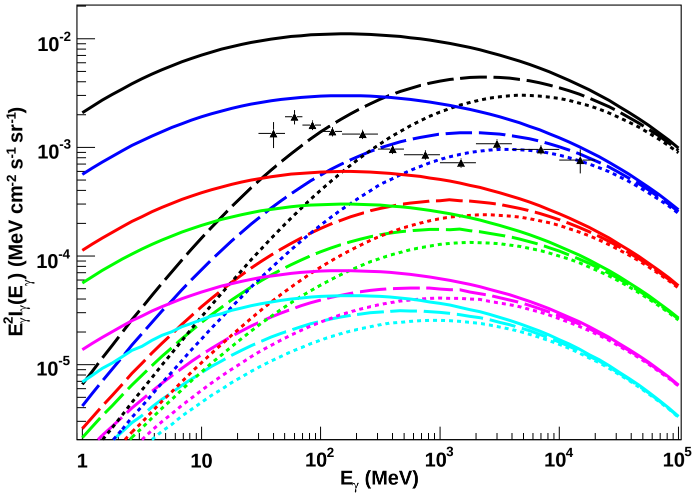

Figure 1.14: Intensities expected from solar-system γ rays. Colours show different angular distances from the Sun: 0.3° (black), 1° (dark blue), 5° (red), 10° (green), 45° (pink), and 180° (light blue). Differences between solid, dashed, and dotted lines are the effect of solar modulations. Data points are the EGRB as determined by Strong et al. (2004). Taken from Moskalenko & Porter (2006).

Chapter 2

Imaging Atmospheric Cherenkov Technique

The imaging atmospheric Cherenkov technique makes use of the opacity of the Earth's atmosphere for very-high-energy (VHE, >100 GeV) particles. γ rays and electrons as well as hadronic cosmic rays interact in the top layers of the atmosphere and produce a cascade of secondary particles, an *air shower*. The secondary particles move with relativistic velocities and emit Cherenkov light. This Cherenkov light can be measured with telescopes from ground. The measurement of the light distribution and intensity allows to estimate the incident particle direction and energy, and to a certain degree also the particle type. The physics of air showers as well as their simulations are discussed in Section 2.1.
Imaging atmospheric Cherenkov telescopes (IACTs) measure VHE γ rays that are produced in interaction processes of cosmic rays. Being electrically neutral, they are not deflected by interstellar magnetic fields and thus point back to their sources. This allows γ-ray *astronomy* with the imaging of astrophysical objects. The success story of the imaging atmospheric Cherenkov technique began with the detection of the Crab nebula by the Whipple Observatory in 1989 in VHE γ rays (Weekes et al. (1989)). Today a new generation of IACTs is in operation: H.E.S.S. in Namibia, MAGIC in La Palma, Spain (Ferenc & MAGIC Collaboration (2006)), the VERITAS telescopes in Arizona, USA (Holder et al. (2006)), and CANGAROO-III in Australia (Kubo et al. (2004)). The H.E.S.S. experiment, with which the measurement of the cosmic-ray electron spectrum presented in this work was conducted, is introduced in Section 2.2.

2.1 Air-Shower Physics and Simulations

2.1.1 Air-Shower Physics

When cosmic rays enter the atmosphere, they interact with air molecules and produce an air shower of secondary particles. Depending on the incident particle, there are two different kinds of air showers: *electromagnetic showers* and *hadronic showers*.

Electromagnetic Showers

If the primary particle is an electron or γ ray, an electromagnetic shower is initiated. The two basic mechanisms involved are $e^+ e^-$ pair creation of a γ ray in the Coulomb field of

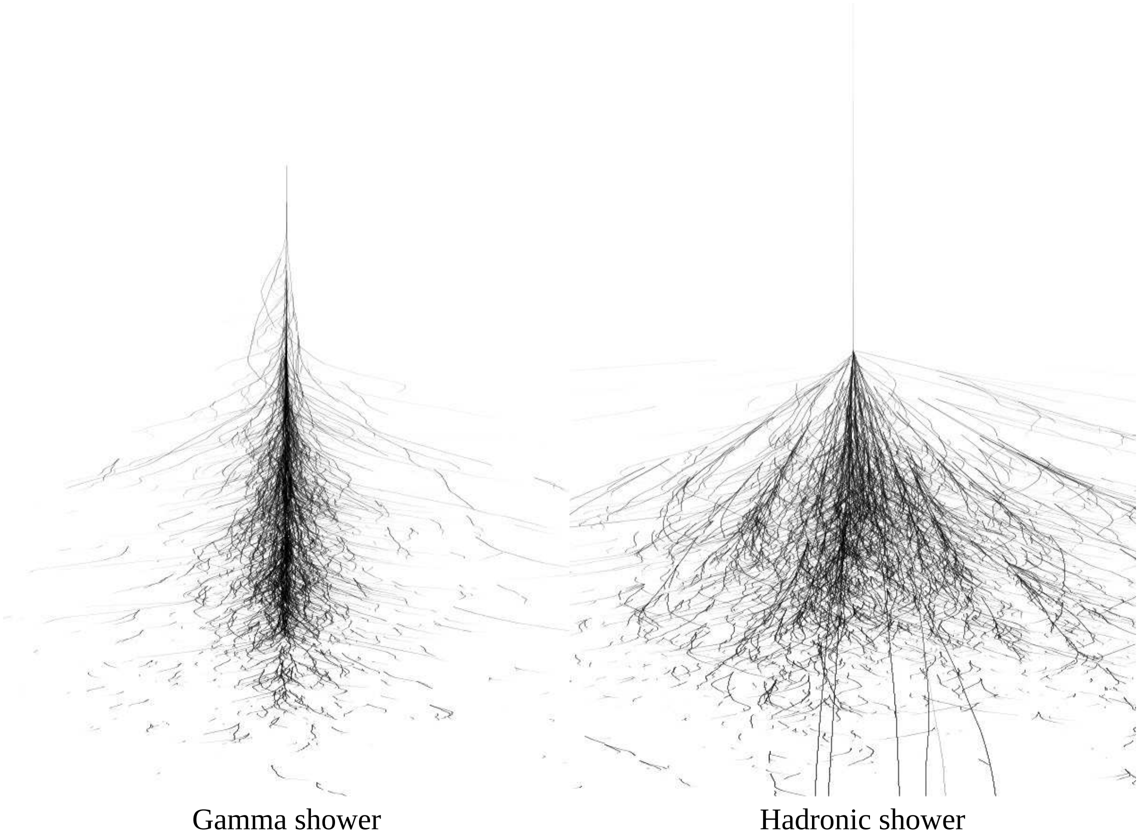

Figure 2.1: Air shower of a γ ray and a proton in comparison. Clearly visible is the broader lateral distribution and the irregular shape of the hadronic shower. Taken from Völk & Bernlöhr (2008).

a nucleus, and the emission of bremsstrahlung by an electron that is deflected by an air nucleus. The characteristic length scale under which bremsstrahlung occurs is the radiation length X_0. If a particle has travelled a distance $x = X_0$, it is on average left with $1/e$ of its initial energy:

$$-\frac{dE}{dx} = \frac{E}{X_0} \; . \tag{2.1}$$

In air, the radiation length is $X_0 = 37.2\ \mathrm{g/cm^2}$. The analogously defined conversion length for pair production is $X_c = 9/7\, X_0$.

As the produced particles (electrons and γ rays) move again with relativistic velocities, they again interact via bremsstrahlung and pair creation; a cascade of particles is formed. The procedure continues to produce new particles until the single particle energy reaches the critical value of 80 MeV, where ionisation becomes the dominant energy loss mechanism. Below this energy, electrons rather ionise the nuclei of the air than undergo bremsstrahlung. No new particles are created and the shower expires in the upper atmosphere.

The number of particles in the shower at its maximum extension is directly proportional to the energy of the incident particle. The depth in the atmosphere at which this maximum occurs, $X_{\max}$, depends logarithmically on the energy. For a 1 TeV electron or γ ray, $X_{\max} \approx 300$ g/cm^2, which corresponds to an altitude of ≈10 km above sea level. Electrons have their shower maximum about half a radiation length (≈20 g/cm^2) higher in the atmosphere than γ rays (Gaisser (1990)).

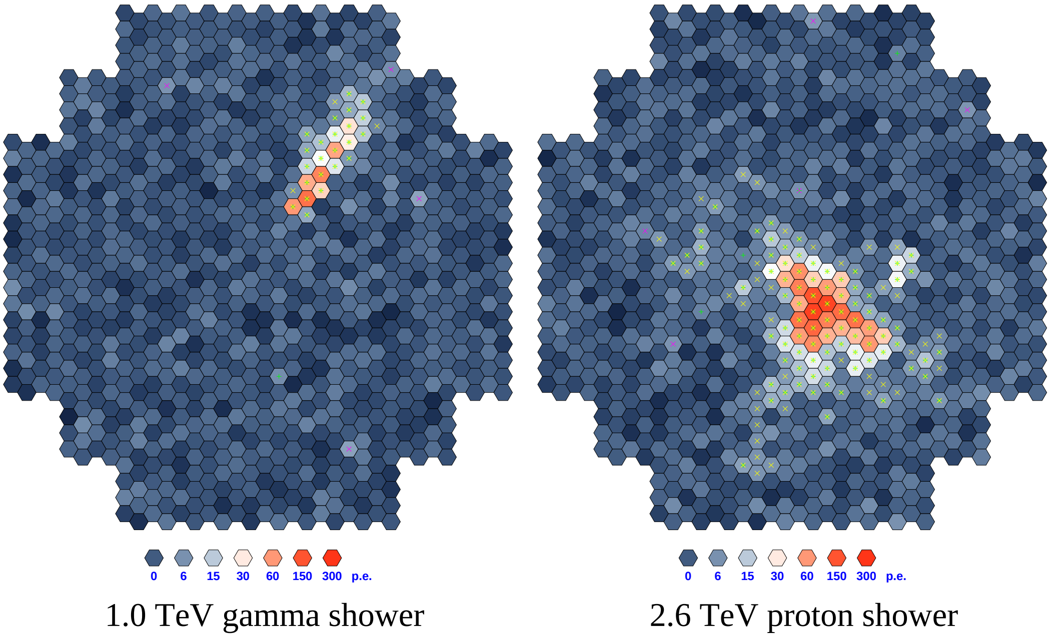

Figure 2.2: Example of a γ-ray and a proton event in one H.E.S.S. camera. As a consequence of the broader and less regular shape of hadronic air showers, their camera images are themselves broader and show larger fluctuations. Taken from Völk & Bernlöhr (2008).

Hadronic Showers

If the incident particle is a proton or nucleus, also strong and weak interactions take place. The inelastic scattering off air nuclei produces mesons (π, K) as well as nucleons and hyperons. Secondary pions and nucleons continue the cascade and the size of the shower increases as long as the energy of the secondaries is above the threshold for multiple pion production of about 1 GeV. The mean free path length of the inelastic scattering is ≈80 g/cm^2 at 1 TeV, therefore hadronic showers start deeper in the atmosphere and also exhibit their shower maximum $X_{\max}$ at larger atmospheric depth than electromagnetic showers.

Hadronic showers lose energy in the production of muons and neutrinos, which are produced in the decay of charged pions and do not interact further thus carrying away their energy.

Due to their different production mechanisms, hadronic showers are distinct from electromagnetic showers by various means: the weak and strong interactions produce high transverse momenta and thus cause a larger lateral extension of the shower. Also the complex processes involving many particles produce large fluctuations in the shower and give it a less regular shape compared to electromagnetic showers. This can be seen in the

comparison of a γ-ray and a hadronic shower in Fig. 2.1. A comparison of the images in one of the H.E.S.S. cameras is shown in Fig. 2.2.
However, the difference between a γ-ray (or electron) and a hadronic shower image is not always that pronounced. Due to the production of π^0 and their subsequent decay into γ rays, electromagnetic sub-showers are initiated. If these electromagnetic sub-showers are strongly pronounced, the shower is hard to distinguish from a γ-ray or electron initiated shower. Cosmic-ray events as background for γ-ray observations are discussed by Maier & Knapp (2007) and Sobczynska (2007), their implications for air-shower simulations are presented in Section 2.1.2.

Cherenkov Radiation

If a charged particle moves in an insulating medium with refractive index n at a velocity $v = \beta c > c/n$, i.e. larger than the speed of light in this medium, it emits Cherenkov radiation due to the polarisation of the medium. The polarisation leads to the emission of electromagnetic waves, which in case of a particle faster than the speed of light interfere constructively. In the atmosphere, the density is not a constant and therefore neither the refractive index.
The light cone of the Cherenkov radiation forms with the particle direction an angle θ:

$$\cos\theta = \frac{1}{\beta\, n} \ . \tag{2.2}$$

Because of Coulomb scattering of the electrons, the Cherenkov light is not emitted along the same axis but diffused over an area with a radius of ≈100 m on the ground. The light flash lasts a few ns.
Cherenkov light on its way to the ground is partly scattered and absorbed. Since the Cherenkov spectrum follows a $1/\lambda^2$ dependence, it has its maximum emission at ultraviolet wavelengths. But these photons are strongly absorbed in the atmosphere, and therefore, the observed maximum lies at wavelengths of ≈330 nm (blue light).

2.1.2 Air-Shower Simulations with CORSIKA

For the analysis of air-shower data, detailed simulations of the reactions in the atmosphere as well as the detector response are necessary in order to determine the incident particle's energy, and the fluxes from the number of detected γ rays. For these simulations the CORSIKA program is used, which was developed at the Forschungszentrum Karlsruhe for the KASCADE experiment (Heck et al. (1998)). CORSIKA is a detailed Monte Carlo program that studies the evolution of air showers in the atmosphere. The details of the CORSIKA program can be found in Heck et al. (1998) and Heck & Pierog (2007).

CORSIKA differentiates between 50 elementary particles (among them γ, $\mathrm{e}^{+/-}$, $\mu^{+/-}$, π^0, $\pi^{+/-}$, $\mathrm{K}^{+/-}$, $\mathrm{K}^0_{S/L}$, η, p, n, hyperons, various resonance states and anti particles), and additionally nuclei up to $A = 56$.
The atmosphere is modelled consisting of N_2, O_2 and Ar with volume fractions of 78.1%, 21.0%, and 0.9%. The density variation of the atmosphere with altitude is taken into account by the use of five different layers. In the lower four, the mass overburden causing the atmospheric density follows an exponential dependence on the altitude with parameters

varying from layer to layer, in the fifth layer, the mass overburden decreases linearly with altitude before it vanishes at $h = 112.8$ km. The mass overburden is continuous at the layer boundaries and can be differentiated continuously. In CORSIKA, always a flat atmosphere is adopted. For small zenith angles as used in the analysis presented here, this is justified. For larger zenith angles, corrections have to be applied.
CORSIKA simulations track an incident particle in the atmosphere, follow its interactions and the involved production of secondary particles, and track the secondary particles as well. Particles are dropped from the calculation if their energy falls below a critical value specified for each particle type. At certain user-defined *observation levels*, the type, energy, location, direction, and arrival times of all particles are stored. This allows a detailed analysis of simulated showers and is the link to the detector simulations described in Section 2.2.2.
CORSIKA contains

- the decay of unstable particles,
- the tracking of particles taking into account ionisation losses and deflection by multiple scattering and in the Earth's magnetic field,
- hadronic interactions of nuclei and hadrons with the air nuclei, and
- the transport and interaction of electrons and γ rays.

Neutral pions and η mesons as well as all resonance states have such a short lifetime that interaction is negligible before they decay. Muons decay only. Neutrons are treated as stable particles due to their long life time. For all other unstable particles, there is a competition between interaction and decay process. Decay length and interaction length are then determined independently at random and the shorter one is taken as the actual path length and the corresponding mechanism is the one taking place. If several decay modes exist, all known modes with branching ratio down to 1% are taken into account. For the use of IACTs, an additional option enables the calculation of the Cherenkov light yield of each particle.

CORSIKA contains all known processes that might play a role in order to give as accurate results as possible. However, the most serious problem of these simulations is the lack of knowledge of hadronic interactions. Cross sections have to be extrapolated since no experimental data exists yet at high energies and in the extreme forward direction. However, this is the most important direction for air showers, but difficult to measure in collider experiments because the forward direction is the position of the beam pipe. Various models are in use that describe hadronic interactions with extrapolations to the energy and angular ranges required. They are usually specialised in low-energy ($E \lesssim 80$ GeV) and high-energy ($E \gtrsim 80$ GeV) interactions. The low-energy models used for this work are the GHEISHA and UrQMD (Bass et al. (1998)) models, and, more important, the high-energy models are the SIBYLL (Fletcher et al. (1994)) and the QGSJET-II model (Ostapchenko (2004)).
A comparison of the different models was performed by Maier & Knapp (2007) and is shown in Fig. 2.3. Plotted is in the left panel the energy fraction that goes into electromagnetic components, $E_{\mathrm{e-m}}/E_{\mathrm{tot}}$, for a 100 GeV proton. It can be seen that the GHEISHA low-energy model has a significantly smaller fraction of energy going into electromagnetic sub-showers than other models. According to the studies of Heck (2006), the GHEISHA

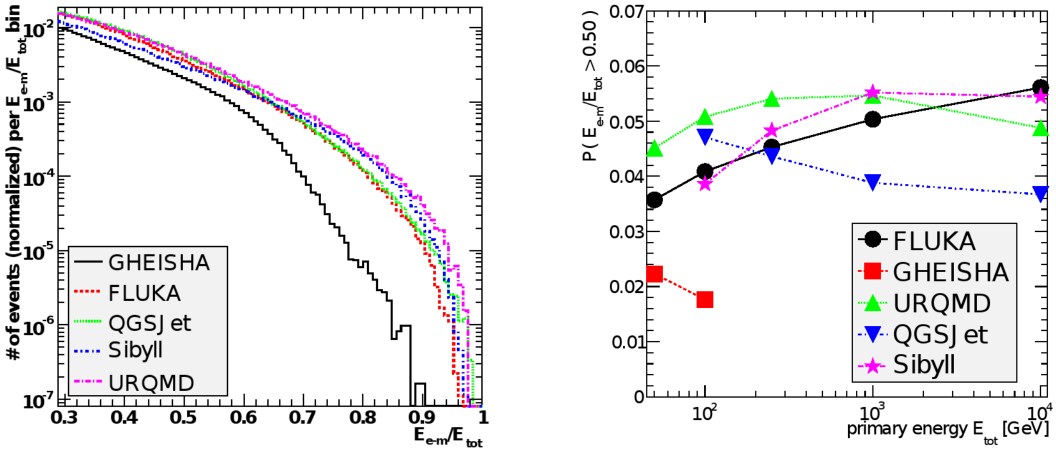

Figure 2.3: Energy deposited in electromagnetic components. Compared are five different interaction models. Taken from Maier & Knapp (2007). *Left*: The fraction of energy going into electromagnetic sub-showers for a 100 GeV proton. *Right*: The probability that more than 50% of the primary energy is deposited in electromagnetic components as function of energy.

model produces too few pions compared to experimental data. Contrariwise, the UrQMD model is the one with the highest probability of a large electromagnetic fraction. In the right panel of Fig. 2.3 the energy dependence of $E_{\mathrm{e-m}}/E_{\mathrm{tot}}$ for an electromagnetic fraction larger than 0.5 is shown. The figure demonstrates that also the energy dependence of the electromagnetic fraction varies between models.

As models differ significantly, it is supposable that this also influences the electron spectrum if determined by the means of hadronic interaction models.

2.2 The H.E.S.S. Experiment

Figure 2.4: The four H.E.S.S. telescopes in Namibia.

After having outlined the physics of air showers, the next section introduces the H.E.S.S. experiment, which uses the Cherenkov light emitted by air showers to measure the properties of the initial particle.
The name H.E.S.S. is short for High Energy Stereoscopic System and at the same time honours Victor Hess, who discovered the cosmic rays. H.E.S.S. is a system of four imaging atmospheric Cherenkov telescopes located in the Khomas highland in Namibia ($23^\circ16'18''$ South, $16^\circ30'00''$ East), at 1800 m above sea level (see Fig. 2.4). The position was chosen because of the altitude, the clear nights, low humidity that is typical for this area, as well as the good view on the Galactic centre, which is not accessible from the northern hemisphere. The four identical telescopes are positioned at the corners of a square with a side length of 120 m. This distance is a compromise between good stereoscopic viewing conditions and a high rate of showers illuminating all four telescopes. Since December 2003, the telescope array is fully operational. The H.E.S.S. experiment covers an energy range from 100 GeV to 100 TeV and is currently the most sensitive instrument in this energy range. Its sensitivity is shown in Fig. 2.5.
Currently, Phase II of the experiment is under construction: a single huge reflector with 600 m^2 mirror area is mounted in the centre of the array. This extension will increase the energy range to below 100 GeV, the angular resolution, and the sensitivity of the experiment.

A detailed description of the H.E.S.S. experiment can be found for example in Hinton (2004) and Aharonian et al. (2006a).

2.2.1 Technical Framework

In the following paragraphs the different components of the H.E.S.S. telescopes and their properties are discussed.

Reflector

The Cherenkov light of an air shower is collected by large reflectors and imaged into a camera located in the focal plane. The mirrors have a focal length of 15 m and a diameter of 13 m. The reflector size allows measurements of γ rays down to 100 GeV. The mirrors consist of 382 single round quartz-coated facets of 60 cm diameter each giving a total of 107 m^2 mirror area and are mounted in Davies-Cotton design (Davies & Cotton (1957)). The mirror reflectivity is about 80% in the wavelength range of 300–600 nm. Each mirror facet has its own motor controlled support unit to align the individual mirrors by a fully automated procedure using the image of a bright star on the closed lid of the camera. Because of the rigidity of the structure, this alignment is very stable. The reflector is mounted on a steel structure in an altitude mount, and a circular rail allows movements in azimuth direction.

Camera

The H.E.S.S. camera (Vincent et al. (2003)) is designed to combine a good image resolution with a large field of view and fast read-out times. For this purpose, each camera consists of a hexagonal array of 960 pixels of photomultiplier tubes (PMTs, Photonis XP2960) of 0.16° aperture each, yielding a total field of view of 5° diameter. The large field of view has proven valuable in the scan of the Galactic plane as well as for the observations of

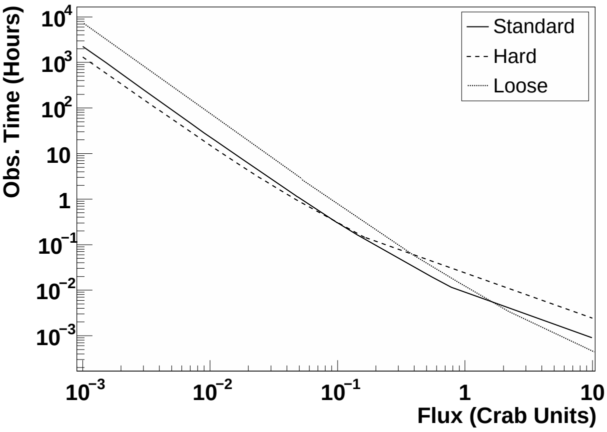

Figure 2.5: The H.E.S.S. sensitivity. Shown is the amount of time needed to detect a VHE pointsource with a statistical significance of $5\,\sigma$ at 20° zenith angle and 0.5° offset from the camera centre, as a function of the flux of the source. The flux is given in units of the flux of the Crab nebula. A spectral slope similar to the Crab is assumed. Three different sets of event selection cuts are distinguished, standard, hard (optimised for weak sources), and loose (optimised for strong sources). Figure taken from Aharonian et al. (2006a).

extended objects like the SNR Vela Jr. Also for the measurement of cosmic-ray electrons, the wide field of view is a key feature that makes their measurement possible.

The PMT peak quantum efficiency lies at ≈25% at ≈400 nm. For a maximum light yield, Winston cones funnel the light into the PMTs in order to close the gaps between the circular PMTs. The camera is constructed in a modular design of 60 *drawers*. Each drawer contains 16 PMTs, the associated read-out electronics and the high-voltage supply for the PMTs. One complete camera amounts to a total weight of ≈800 kg.

Trigger

The H.E.S.S. trigger consists of a trigger on camera level and a central trigger. A camera triggers, if within 1.5 ns at least three PMTs of a *sector* register a signal of at least 4 photo electrons (p.e.). A sector in the camera comprises 64 pixels. The sectors are arranged in overlap. This condition selects extended, spatially connected signals (as they are expected from air showers), as opposed to random signals caused by night sky background and noisy pixels.

The central trigger (Funk et al. (2004)) requires at least two telescopes triggering within 80 ns. Only then, the array triggers and data are read out and stored. Thereby the central trigger drastically reduces triggering due to night sky background and single muon events, and therefore the dead time of the system.

2.2.2 Simulation of the Detector Response with *sim_hessarray*

The hardware of the H.E.S.S. telescopes is simulated using a simulation program called *sim_hessarray*. Together with CORSIKA, which was presented in Section 2.1.2, *sim_hessarray*

zenith Simulations	0 °	20 °	30 °	40 °
electrons	8.9×10^7	9×10^7	9×10^7	8.8×10^7
γ rays (diffuse)	-	1×10^7	-	-
γ rays (point-like)	-	1×10^7	-	-
protons (SIBYLL, GHEISHA)	-	4×10^9	-	-
protons (QGSJET-II, UrQMD)	-	3.8×10^9	-	-
helium	-	2.5×10^7	-	-
nitrogen	-	1.5×10^7	-	-
silicon	-	2.75×10^7	-	-
iron	-	2×10^7	-	-

Table 2.1: Numbers of simulated events used for the electron analysis.

is one cornerstone of the H.E.S.S. data analysis. It provides a full description of the H.E.S.S. telescopes.

As the telescope simulations with *sim_hessarray* are much faster than the CORSIKA simulations, one shower is used multiple times with randomly (horizontally) displaced telescope arrays in the detector simulation. Cherenkov light is treated in bunches of photons for a faster simulation. These photon bunches are tracked through the detector components if they pass within a specified radius from the detector position. The bunch size is chosen such that each bunch gives less than 1 photo electron signal in the camera.

The simulation of the optics includes

- the atmospheric transmission (determined for different weather conditions for Windhoek),
- the reflection on non-perfect mirror facets with random misalignments and a wavelength dependent mirror reflectivity,
- the shadowing of the camera (and optionally also the masts of the camera support structure), and
- the acceptance of the pixels (PMTs as well as Winston cone funnels) dependent on the angle of incidence, and the wavelength dependence of the PMT quantum efficiency.

The full simulations contain also a simulation of the electronics, the triggers and random night sky background, which might even contain stars. The simulations are very flexible due to the use of configuration data files containing relevant information on weather conditions, mirror reflectivity and so on.

The output of the *sim_hessarray* simulations is converted into the same raw data format as the H.E.S.S. data. The same calibration and reconstruction software is applied. Thus, the air-shower simulations give a very reliable tool in the data analysis of the H.E.S.S. data.

2.2.3 Simulations Used in the Analysis

With the combination of the air-shower simulations with CORSIKA and the simulation of the detector response with *sim_hessarray*, electron and proton events are simulated, as

well as heavier nuclei and γ rays for tests and systematic studies.
Simulations of diffuse electrons with a view cone of 2° are generated using CORSIKA 6.204 at zenith angles of 0°, 20°, 30°, and 40° in an energy range of 0.1–40 TeV.
Diffuse protons are simulated with CORSIKA 6.204 using SIBYLL as high-energy hadronic interaction model and, with CORSIKA 6.600, QGSJET-II, both in a view cone of 2.2° with energies of 0.2–60 TeV (0.2–100 TeV for QGSJET-II).
A small data set of nuclei (helium, nitrogen, silicon and iron) is used for systematic tests, as well as some diffuse and point-like γ-ray simulations. All simulations are produced with an energy distribution following a powerlaw with spectral index of 2. By the use of energy dependent weighting other spectra are emulated for the modeling of proton (2.7) and electron spectra (3.3). The spectral index of 2 is chosen to avoid poor statistics at the high-energy end of the spectrum, which would be caused by steeper spectra.

2.2.4 Data Taking

The H.E.S.S. array takes data only during astronomical darkness, i.e. in moon-less nights when the Sun is 18° or more below the horizon. Observations are divided in 28 min duration *observation runs* and are generally performed in *wobble mode*: if observing an astrophysical target, a pointing position is chosen at a fixed offset (between 0.5° and 1°) from the target position. This pointing position is tracked during the observation run. For the next observation run, the pointing position is mirrored at the target position. This procedure facilitates the background subtraction in the analysis. The background estimation of γ-ray observations takes advantage of the large field of view of the H.E.S.S. cameras and determines the background from *off* regions (without any γ-ray source) from the same field of view. The advantage of the *wobbling* around the target position over a direct pointing to the target is the possibility to find *off* regions at the same offset from the camera centre as the target position, thus reducing systematic effects due to a radial drop in acceptance in the camera.
In the following, the standard H.E.S.S. data analysis is shortly summarised.

2.2.5 Standard Data Analysis Method

For the H.E.S.S. data analysis, several analysis techniques are in use (Hillas, Model, and 3D Model, multivariate analysis techniques). These analysis techniques allow a precise measurement of the spectrum and spatial extension of all kinds of γ-ray sources with limited extension. The standard method (Hillas), which is generally used for publications, is shortly presented in the following. A more detailed description of the H.E.S.S. standard analysis can be found in Hoppe (2008).

Calibration and Reconstruction

The H.E.S.S. raw data consists of events with two to four air-shower images. In a first step, these images are calibrated such that pixel amplitudes are in photo electrons (p.e.) and pedestals are subtracted (for details see Aharonian et al. (2004a)). The calibrated images are then cleaned of pixels most likely only containing noise from night sky background. For this purpose only pixels are kept that contain more than 5 p.e. and have a neighbour with more than 10 p.e., or vice versa. Thereby, spatially correlated features are selected. The cleaned image is parametrised in terms of the *Hillas* moments (Hillas (1985)). The shape of the shower image in the camera is approximated by an ellipse and the centre-of-gravity, the image size (i.e. number of photo electrons contained in the cleaned image), the orientation of the ellipse in the camera, and the length of the major and minor axis are calculated. The Hillas parameters are illustrated in Fig. 2.6. They contain all information needed to reconstruct the shower direction, the impact distance, the depth of the shower maximum, and the energy of the incident particle. The shower direction is reconstructed stereoscopically by the means of the intersection of the major image axes (see Fig. 2.6) and an angular resolution of $\lesssim 0.1°$ is obtained. The *impact distance* is the distance of the impact point, where the extrapolation of the incident particle's trajectory reaches the ground, to the telescope array. It is reconstructed in a similar way by intersecting the major axes in the coordinate system of the telescope array. The angular distance of the centre-of-gravity to the reconstructed direction and the impact distance are used to calculate the height (in meters) at which the shower maximum occurs. The depth of the shower maximum, X_{max} (in units of g/cm^2), is then computed from the atmospheric profile. The energy of the incident particle is determined from the image intensity as function of zenith angle and impact distance by comparison with simulations. This is done for each telescope separately, and then averaged over the telescopes. Since the mirrors degrade over time (on the timescale of years), the image intensity of an event with a given energy is reduced, causing a shift in the total energy scale. This effect can be corrected by the use of muon events (*muon correction*, Bolz (2004)). These events are easily recognised because of their ring-like images and their light yield can be predicted and thus provides a measurement of the through-put of the whole system. A correction factor is determined for each run and telescope, and applied to the energy estimate reconstructed assuming nominal optical efficiency (*reconstructed energy*) for each telescope separately before averaging over all telescopes.

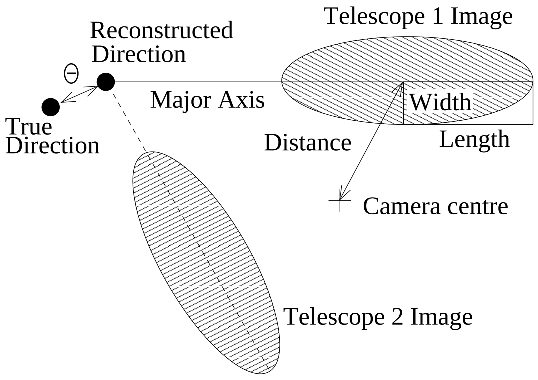

Figure 2.6: Schematic drawing of the air-shower images of two telescopes. Shown are the width and length of the Hillas ellipse. The direction reconstruction by the means of intersecting the two major axes of the ellipses is sketched. Taken from Aharonian et al. (2006a).

γ-Hadron Separation

In order to separate the γ-ray like events, event selection cuts are applied. Such event selection cuts, which are also important later on in this work, select a subset of the original data set based on event characteristics. For the γ-hadron separation, a cut on the image size assures the availability of a minimum of information. A "local distance" cut assures that the centre-of-gravity of the Hillas ellipse is not further away from the camera centre than 2° to avoid images only partly contained in the camera leading to a faulty reconstruction. As hadronic showers have a broader image in the camera than leptonic showers, the width of the Hillas ellipse is a convenient tool to distinguish them. Since the width depends on the shower's energy, the zenith angle and the impact distance, a *scaled* parameter is defined that links the measured width to the mean expectation obtained from Monte Carlo simulations for a given energy, zenith and impact distance, scaled by the spread in the distribution of the simulations. The scaled width is then averaged over the telescopes, giving the *mean scaled width*:

$$MSCW = \frac{1}{N_{\mathrm{tel}}} \sum_{i=1}^{N_{\mathrm{tel}}} \frac{\mathrm{width}_i - \langle \mathrm{width}_i^{MC} \rangle}{\sigma_i} \,. \tag{2.3}$$

The definition for the *mean scaled length*, $MSCL$, is analogous. The cuts on the $MSCW$ and $MSCL$, the image size and the squared angular distance to the source position are optimised simultaneously for a maximum detection significance. Details are described in Aharonian et al. (2006a).

Background Determination

After selecting the γ-ray like events, the remaining background of hadronic events has to be subtracted. Here the analysis takes advantage of the isotropy of cosmic-ray arrival directions. The background is usually estimated from *off* regions within the field of view, that do not contain γ rays. The number of background events in the *on* region is then evaluated as αN_{off}, where N_{off} is the number of events in the *off* region and α is the normalisation factor that corrects for differences in area and acceptance. In Fig. 2.7 two possible methods are illustrated. The choice of *off* regions of equal size, distributed at the same distance around the camera centre (*reflected region method*), allows a simple calculation of the background in the *on* region, because no acceptance correction is needed[1]. This reduces α to a purely geometrical factor accounting for the larger area of the *off* region. For the choice of a ring around the source position to evaluate the background level (*ring background method*), the camera acceptance has to be known. However, this method is advantageous if a map of γ-ray emission of the whole camera field of view is desired, because a ring can be placed around any point of the field of view.

For both methods it is important to avoid any γ-ray source in the choice of the *off* regions. For this purpose *exclusion* regions are defined that amply include any region where γ-ray emission has been detected. The exclusion regions are not used for the background estimation.

A summary of different background models is given in Berge et al. (2007).

---

[1] The acceptance of the camera is assumed to be radially symmetric.

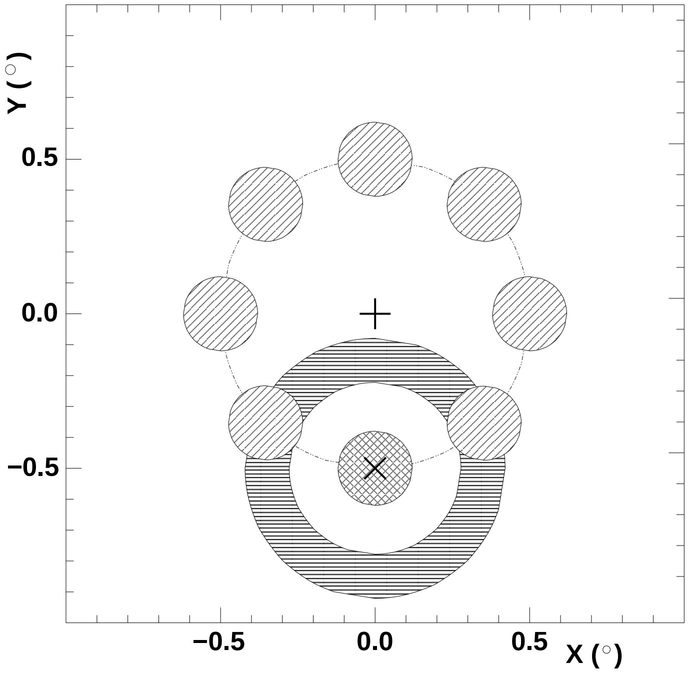

Figure 2.7: Sketch of two different methods to determine the background in the *on* region (cross hatched) around the source position (X): Either *off* regions of equal size are distributed at the same distance around the camera centre (diagonally hatched, the camera centre is marked with an upright cross) or a ring around the source position is chosen as *off* region (horizontally hatched). Taken from Aharonian et al. (2006a).

Spectrum Determination

The number of γ-ray events in the *on* region is obtained by subtracting the background events in the *on* region (αN_{off}) from the total number of events measured in the *on* region (N_{on}):

$$N_\gamma = N_{\mathrm{on}} - \alpha\, N_{\mathrm{off}} \ . \tag{2.4}$$

The flux is determined according to Eqn. (2.4) by weighting each event with its effective collection area A_{eff}:

$$\frac{dF_i}{dE} = \frac{1}{T\,\Delta E_i}\left(\sum_{j=1}^{N_{\mathrm{on}}}\frac{1}{A_{\mathrm{eff,j}}} - \alpha\sum_{k=1}^{N_{\mathrm{off}}}\frac{1}{A_{\mathrm{eff,k}}}\right) \ . \tag{2.5}$$

Here, T is the observation time corrected for losses due to the dead time of the system (*livetime*) and ΔE_i is the size of the energy bin of this spectral point.

2.2.6 Selected Highlights

After having detailed the hard- and software of the H.E.S.S. experiment, it is worth to mention its contribution to high-energy astrophysics. Since its inauguration in 2004,

the H.E.S.S. experiment has detected more than 60 VHE γ-ray sources, thereby decupling the total number of known γ-ray sources. The scan of the Galactic plane alone (Aharonian et al. (2005)), which was conducted between 2004 and 2005 and since then consecutively extended, resulted in the detection of 45 sources. Among these sources are 9 pulsar wind nebulae, many "dark" sources with no counterpart in other wavelengths, and three shell-type SNRs: RX J1713.7-3946 (Aharonian et al. (2007c)), RX J0852.0-4622 (Vela Jr., Aharonian et al. (2007d)), and RCW 86 (Aharonian et al. (2008b)). SNRs have long been discussed as likely acceleration sites of the bulk of Galactic cosmic rays (see Chapter 1), and the detection of γ rays proves the existence of TeV particles in the expanding SNR shock. However, the question of the nature of these particles (hadronic or leptonic) has so far not been answered conclusively.
Also extragalactic sources have been successfully detected by H.E.S.S. Various AGN have been observed and their spectra derived, which allowed to set restrictive limits to the extragalactic background light, which causes AGN spectra to steepen at longer distances (Aharonian et al. (2006b)). In 2006, during the regular monitoring of the AGN PKS 2155-304, an exceptionally bright γ-ray flare was observed (Aharonian et al. (2007a)). The H.E.S.S. observations triggered a broad multiwavelength observation of this object. The flux, increased by a factor of 100, was found to be variable in time scales of a few minutes, and was during the observation period not only the brightest source on the γ-ray sky but also the brightest source ever observed in VHE γ rays.

The H.E.S.S. experiment has clearly contributed to the success story of the imaging atmospheric Cherenkov technique. Since the first break-through of the Whipple experiment using the imaging atmospheric Cherenkov technique to detect the Crab nebula at $9\,\sigma$ confidence level in more than 80 hours of observation time (Weekes et al. (1989)), with the sensitivity of H.E.S.S. we have now reached a point at which even challenging measurements such as the determination of the cosmic-ray electron spectrum come into reach. The analysis of cosmic-ray electrons with its special demands is presented in the following.

Chapter 3

Cosmic-Ray Electron Analysis

In this chapter the data analysis of cosmic-ray electrons is described and the resulting spectrum is interpreted. It extends the results already published in Aharonian et al. (2008a). First a short summary on the event reconstruction is given in Section 3.1. Due to the huge hadronic background, considerable effort goes into the identification of electrons and reduction of hadronic background. For this purpose the usage of the machine-learning algorithm Random Forest is discussed in Section 3.2. The fitting procedure that determines the remaining background is described in Section 3.3. After a short summary of the data selection criteria in Section 3.4, the generation of the spectrum of cosmic-ray electrons is discussed in Section 3.5. Section 3.6 presents the spectrum of cosmic-ray electrons. Various systematic tests on this analysis are summarised in Section 3.7. Finally, the spectrum is interpreted in Section 3.8.

3.1 Event Selection and Energy Reconstruction

As described in Chapter 2.2.5 each event to be treated in the data analysis needs to be characterised by a set of parameters such as energy, direction, and the Hillas length and width (for particle identification) obtained by the event reconstruction.

Events used in this analysis are subject to the standard H.E.S.S. calibration and image cleaning. Each event is reconstructed in terms of the Hillas parametrisation and its direction is determined stereoscopically in the standard H.E.S.S. analysis scheme. For this purpose the local distance cut of the standard H.E.S.S. analysis assures that the centre-of-gravity of the Hillas ellipse is not further away from the camera centre than 2° in order to avoid a bias in the image reconstruction. The energy reconstruction is performed in the standard way as detailed before, but dedicated lookups are generated from Monte Carlo electron simulations for an electron-specific energy reconstruction.

Based on the event reconstruction first cuts are applied to ensure good quality data in the analysis. These cuts are Cuts A and Cuts B. They are summarised in Table 3.1. Cuts A contain a minimum size of 200 p.e. in each image after image cleaning and a maximum impact distance of 200 m. The cut on the image size guarantees that events have pronounced images with a good Hillas parametrisation. The cut on the impact distance was chosen because showers that have their impact point at larger distances are generally not as well reconstructed as those nearby. These cuts are chosen for high energies. Cuts B are chosen for a better performance at low energies. The cut in image size is loosened to 80 p.e. in

	Distance of shower's impact point	Image size in each camera
Cuts A	<200 m	>200 p.e.
Cuts B	<100 m	>80 p.e.

Table 3.1: Summary of event selection cuts. Cuts A constitute the set of cuts used in this work for the electron spectrum, Cuts B are only used in Chapter 3.5 for a reduction of the energy threshold to extend the spectrum to lower energies.

order to reduce the energy threshold. The harder cut on the impact distance of 100 m is motivated by the need of well reconstructed events in the face of very good statistics. Cuts B are used to extend the electron spectrum obtained with Cuts A to lower energies. For this purpose not only a different set of cuts is chosen but also a different data set with improved optical efficiency, which will be discussed in Section 3.6.1.

The influence of Cuts A and B on the energy reconstruction is shown in Fig. 3.1. The left panel shows the mean relative energy bias $(E_{\text{reco}} - E_{\text{true}})/E_{\text{true}}$ with E_{reco} being the reconstructed energy and E_{true} the true energy, with which the electron was simulated, as function of the true energy of the simulations. The energy range of the analysis has to be chosen such that in this range the energy bias is close to 0. The distribution in Fig. 3.1 shows large deviations at energies below 400 GeV and above 20 TeV. The reasons are spill-over effects of events with lower/higher energy than the energy range covered by the energy lookups. The low-energy threshold depends on the chosen cuts and is comparatively lower for Cuts B than for Cuts A. Only energies with an energy bias smaller than 10% are used for the analysis. The energy ranges of the two analyses with Cuts A and B are indicated in Fig. 3.1 by vertical lines. The threshold of the Cuts A is at a comparatively high energy with an apparent bias of less than 5%. This high threshold is necessary due to the effect of optical efficiency correction, which uses simulations at lower energies to mimic events with a reduced efficiency[1]. As the analysis with Cuts B uses data with good optical efficiency, for this analysis this effect is not as pronounced.

The right panel of Fig. 3.1 shows the distribution of the relative error of the energy reconstruction for the two Cuts A and B. Included are only events that pass the event selection cuts and have their energy reconstructed in the corresponding energy range. Cuts B have a significantly broader distribution, which is caused by both the lower energy threshold and the looser cut in the image size. The root mean square of the distribution is 12% for Cuts A and 15% for Cuts B.

3.2 Electron Identification

As can be seen from Fig. 1.1, in the TeV region there are ≈1000 protons for every electron at a particular energy. Thus, for an acceptable signal to background ratio, an excellent separation power is needed that reduces protons by a factor 10^{-3} while leaving the electron component largely unaffected. A first step is the restriction of the analysis to events that are well measured, meaning only events reconstructed using all four telescopes, which have a maximum of information available. The second step is to use this image information in

---

[1] See Section 3.5.2 for details.

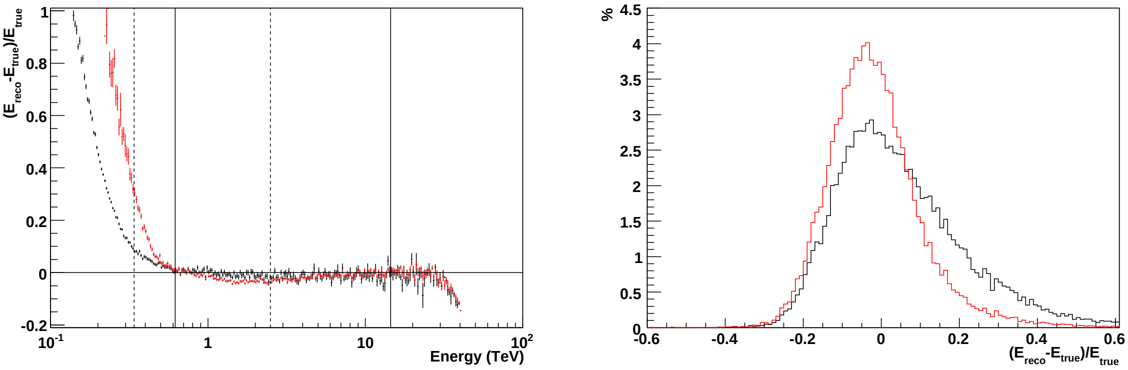

Figure 3.1: The energy reconstruction as determined from Monte Carlo simulations at a zenith angle of 20° for the two sets of event selection cuts, Cuts A in red and Cuts B in black. *Left*: The relative energy bias $(E_{\mathrm{reco}} - E_{\mathrm{true}})/E_{\mathrm{true}}$ as function of energy. The solid vertical lines show the energy range of the analysis performed with Cuts A. The dashed vertical lines indicate the energy range of the low-energy analysis. *Right*: Distribution of the relative error in the reconstructed energy for events in the energy range of the analyses, i.e. 0.62–14.5 TeV for the analysis with Cuts A, 0.34–2.5 TeV for the analysis with Cuts B.

an optimal way to extract a particle identification. For this purpose a machine-learning algorithm is used that combines the available image information to a single separation parameter.

3.2.1 Random Forest Method

For an optimised background suppression, the Random Forest algorithm[2] (Breiman (2001)) was chosen to separate between electrons and background events. This algorithm was investigated by Bock et al. (2004) for the application to Cherenkov telescopes and was customised for the data analysis of the MAGIC collaboration (Albert et al. (2008)). The customisation and implementation of the Random Forest for H.E.S.S. was initially done by Egberts (2005). Ohm (2007) further developed and integrated the algorithm into the H.E.S.S. analysis software.

Random Forest is a machine learning algorithm consisting of a “forest” of decision trees. A decision tree as shown in Fig 3.2 is a structure of decision *nodes*: each decision node has, except for the starting node, only one incoming connection and, except for the final nodes, exactly two outgoing connections. In each node, a true/false decision in the form of a cut on one of the input parameters is applied. Each decision tree decides from the set of input parameters whether this event was an electron (1) or background (0) event.

The input parameters (52 in total) are telescope-wise information on the shower image in the four cameras, i.e. per telescope (and camera) there are 13 parameters. As the Random Forest is stable against parameters that do not contain a significant separation power (Breiman (2001)), any information on the shower that can possibly contribute to the sepa-

---

[2] The code is available at http:www.stat.berkeley.edu/users/breiman/RandomForests/.

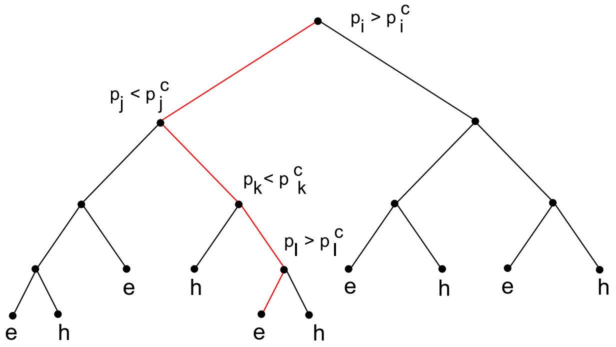

Figure 3.2: Schematic drawing of a decision tree of the Random Forest. An event with a parameter set $\{p\}$ enters the decision tree at the root node. The parameter p_i of the event is compared to p_i^c, the optimised cut value. Events with $p_i < p_i^c$ are led to the successive right node, events with $p_i > p_i^c$ to the left. In the highlighted example (red) the event follows the left-hand side sub-tree. In the following node, the parameter p_j is tested. This procedure continues until a final node is reached. The final nodes are either labelled with e for electron or h for hadron. In the example, the decision tree "decides" for an electron.

ration is included. Hadronic cosmic rays, which interact strongly and electromagnetically in the atmosphere, produce broader and less regular showers than purely electromagnetically interacting electrons (and γ rays). Therefore the length and width of the Hillas ellipse are good separators between electrons and background. They are calculated for each camera image and scaled with the expectation from γ-ray simulations[3]. The parameters are listed in Table 3.2.

The performance of the Random Forest rises with the number of trees. The reason is that for each tree a different subset of known electron and background events is used to "train" the tree. In addition, each tree chooses in each node between different decision parameters as explained in the next sub-section. The number of trees is chosen somewhat arbitrarily, being restricted only by the criteria of a sufficiently high number of trees in order to avoid performance losses, and computational limitations. The Random Forest consists of 500 decision trees. Averaging over all decision trees yields an output parameter $\zeta \in [0, 1]$, which gives the degree of *electron-likeness* of the event.

Training of a single tree

In order to teach the Random Forest the difference between electron and background events, it is *trained* with events of known type, i.e. with simulations and background events.

The training procedure of each decision tree involves the following: a set of 52 input parameters $\{p\}$ of events of known type is used to teach the algorithm the difference between electrons and background events. The training set consists of Monte Carlo electron simulations and data from empty fields. The electron simulations are generated at a zenith

---

[3] The *scaled width* and *scaled length*. See Chapter 2.2.5 for details.

Scaled width of the Hillas ellipse
Scaled length of the Hillas ellipse
Skewness (third Hillas moment, measure of the asymmetry)
Kurtosis (fourth Hillas moment)
Size (intensity of the camera image in photo electrons)
Number of pixels in the camera with an intensity larger 0
Number of pixels in the camera with an intensity larger 10
Number of pixels in the camera with an intensity larger 30
Intensity of the sum of the two brightest pixels in photo electrons
Intensity of the pixels within the Hillas ellipse in photo electrons
Intensity of the pixels within 1.5 × the Hillas ellipse in photo electrons
Intensity of the pixels within 2 × the Hillas ellipse in photo electrons
Distance of the shower's impact point from the telescope

Table 3.2: Training parameters of the Random Forest. Most important parameter for the classification is for all energy ranges the scaled width.

angle of 20°[4], the data from empty fields are distributed in a very narrow range around an average zenith angle of 20.6°.

Using the training data set of electron simulations and empty field data, the algorithm creates a number of binary decision trees. For each decision tree, the training starts with all data in the root node. Then from the set of parameters $\{p\}$ a subset of seven[5] parameters is randomly chosen. Among these seven parameters the parameter with the highest separation power is determined, and is used to split up the data set, leading the two new subsets into two successive nodes. This procedure continues until a node contains data from only one type. This terminal node now obtains a label according to the type of data it contains.

The single decision trees vary by the means of two random components: Firstly, a subset of training events is randomly chosen out of the training data set, resulting in different events used for the training of individual decision trees. Secondly, in each node a random subset of input parameters is chosen, among which the parameter of highest classification power is selected and the optimal cut determined.

To reduce the effect of performance loss due to the energy dependence of the input parameters, Random Forests were trained in five different energy bands: 0.5–1 TeV, 1–2 TeV, 2–4 TeV, 4–8 TeV, and 8–16 TeV.

The Random Forest was trained at a zenith angle of 20°. Since parameters are zenith angle dependent, this reduces the performance at much larger zenith angles[6].

---

[4] The data set used for the training of the Random Forest is an independent data set and not used further for the analysis.

[5] The number of chosen parameters has been optimised for the case of a Random Forest with 52 parameters. The recommendation given in the Random Forest manual for this number is $\sqrt{N}$, with N being the total number of input parameters.

[6] For a classification at zenith angles beyond ≈40° Random Forests should be trained in bands of zenith angles. However, for this analysis the restriction in zenith angle is forced anyways by the limited proton simulations.

3.2.2 The ζ Parameter

The output parameter of the Random Forest, ζ, is based on various information on the shower images. In the following, the behaviour of this parameter is studied. For this purpose, simulations are used to investigate the ζ distributions of electrons, protons, and heavier nuclei. The dependence of the parameter on energy, offset of the shower direction from the pointing position, and zenith angle is examined. Simulations are also compared to real data as a check of consistency.

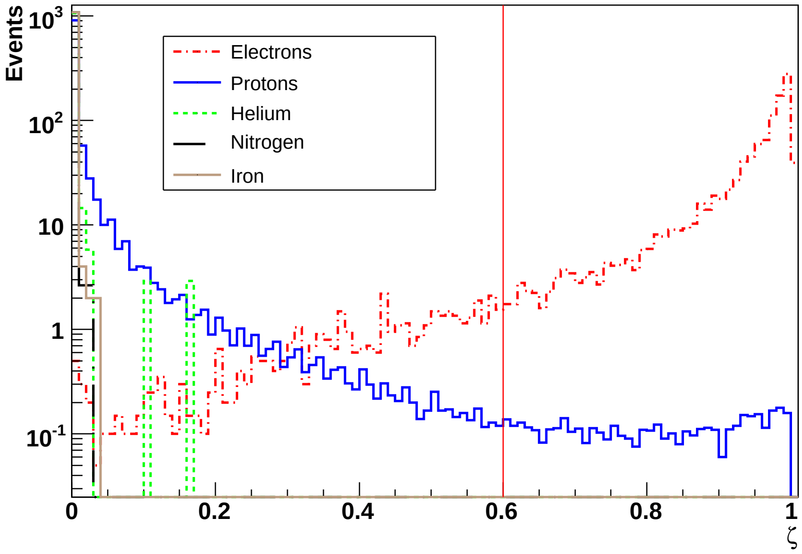

Figure 3.3: The Random Forest output parameter ζ for simulations of electrons, protons, helium, nitrogen, and iron in the energy range of 1-4 TeV. The large spikes in the distribution of helium are statistical fluctuations due to the limited number of available simulations. The vertical line demonstrates the range in ζ in which the fit for the background determination, which is explained in Section 3.3, is conducted.

Performance

The distribution of ζ for simulations of electrons, protons and heavier nuclei is shown in Fig 3.3. As expected by construction, the electron distribution peaks at 1, while the proton distribution has its peak at 0. Furthermore, from the comparison of the simulated protons and nuclei it becomes apparent that the Random Forest identifies heavier nuclei more easily as background events; their ζ distributions have a sharper peak at zero.

The good separation power of the ζ parameter is used to apply an event selection cut that removes most of the hadronic background. A high performance of a cut is achieved if most simulated electrons survive the cut, while simulated protons are cut off. The performance of the ζ parameter is shown in Fig. 3.4 in the form of the fraction of simulated electrons passing a ζ cut plotted over the fraction of simulated protons that are left in the data set

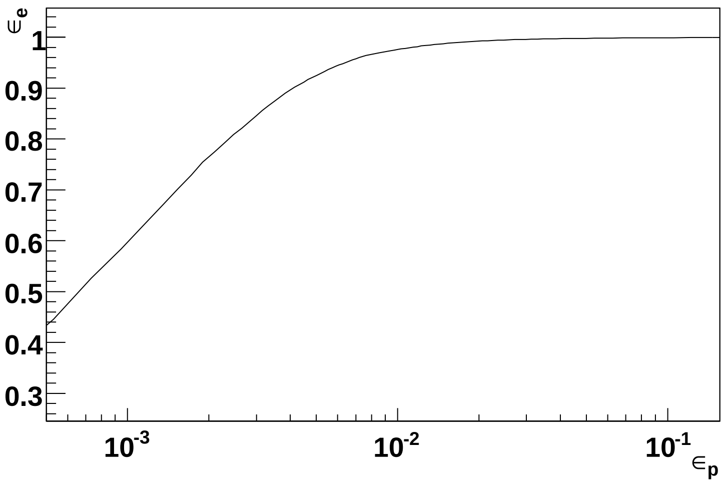

Figure 3.4: The cut efficiency of the ζ parameter for events with reconstructed energy between 1 and 4 TeV.

after the cut (i.e. the electron efficiency $\epsilon_e = N_e^{\mathrm{sel}}/N_e^{\mathrm{tot}}$ plotted over the proton efficiency $\epsilon_p = N_p^{\mathrm{sel}}/N_p^{\mathrm{tot}}$, with N_e^{sel} being the number of electron events passing the cut and N_e^{tot} the total number of simulated electron events, and for protons accordingly). A cut of $\zeta > 0.6$ was chosen (indicated by the vertical line in Fig. 3.3) to drastically reduce the hadronic background while keeping most of the electron signal. A background suppression to a level of 0.72% is achieved at energies between 1 and 4 TeV, while keeping 96% of the electrons. The cut efficiency increases further with energy. After a $\zeta > 0.6$ cut, the remaining background is completely dominated by protons.

Dependencies

Since at least some of the training parameters of the Random Forest depend on energy, the offset from the camera centre, and the zenith angle, the ζ parameter itself can depend on these variables. These dependencies are investigated in Fig. 3.5 for simulated electrons and protons in the relevant region of $\zeta > 0.6$. Although the general behaviour of the distributions remains the same, it can be seen that the performance of the parameter increases with energy: The peak of the ζ distribution of the electron simulations at $\zeta = 1$ becomes sharper with increasing energy, while the proton level at high ζ decreases slightly with energy. This energy dependence will in the following enforce a correction of the ζ distributions due to optical efficiency changes and the resulting bias in energy reconstruction[7]. The offset dependence is only weak. The zenith angle dependence is investigated only for electron simulations since protons are simulated only at 20° zenith angle. The optimal performance lies between 20° and 30° reflecting the training of the Random Forest with simulations at 20°.

---

[7] See Chapter 3.5.2.

Spectral Index Correction

In consideration of the energy dependence of the ζ distribution, the spectral index with which the simulations were generated becomes important for the description of the data with simulations. Simulations follow a powerlaw with an index of 2 (see Chapter 2.1), while the data is known to consist of protons with a spectral index of 2.7 and electrons of about 3.3. To take this effect into account, the ζ distributions of simulations are weighted by a factor $(E_{\mathrm{true}}/0.3\,\mathrm{TeV})^{2-2.7}$ for protons and $(E_{\mathrm{true}}/0.3\,\mathrm{TeV})^{2-3.3}$ for electrons. Here E_{true} denotes the energy at which the particles are generated (in contrast to the energy at which they are reconstructed). The factor 0.3 TeV ensures that the weighting factors are always smaller than one. Each bin of the weighted ζ distributions therefore contains a sum of the weights w_i. The errors of the weighted bin entries are determined according to $\Delta \sum_i w_i = \sqrt{\sum_i w_i^2}$.

Comparison Simulations-Data

As the presented analysis crucially depends on the use of simulations, a good agreement between simulations and data is essential. Fig. 3.6 shows a comparison of the ζ distributions of simulations and extragalactic data without any γ-ray source. A good match is demonstrated in the region of small ζ between data and a cosmic-ray model with a mixed composition of simulated protons, helium, nitrogen, silicon, and iron, each element representing a band of nuclear charge numbers. The contribution of the representative elements to the model is estimated according to the measured fractions of these charge number bands to the total cosmic-ray flux at TeV energies from Hörandel (2003). At large values of ζ an excess in the data is visible compared to the hadronic cosmic-ray model. This excess is due to the cosmic-ray electrons contained in the data and their measurement is targeted by the presented analysis.

In order to demonstrate the good agreement between simulations of electromagnetic showers and data, γ rays are used. They have the advantage that a background-free data set can be obtained by the use of background subtraction from off-source regions as conventionally done in γ-ray astronomy (Berge et al. (2007)). In Fig. 3.7, background-subtracted γ-ray data are shown in good agreement with simulated γ rays. The γ-ray data are obtained from the H.E.S.S. source HESS J1745 $-$ 290 (Sgr A*) with a θ^2 cut around the source position of 0.0125 deg^2 The data are background subtracted by the *reflected region method*[8].

As neither a background-free data set of electrons nor isolated proton data in the signal region $\zeta > 0.6$ exists, the agreements obtained can only be taken as indication that proton and electron simulations describe the data appropriately.

---

[8] See Chapter 2.2.5.

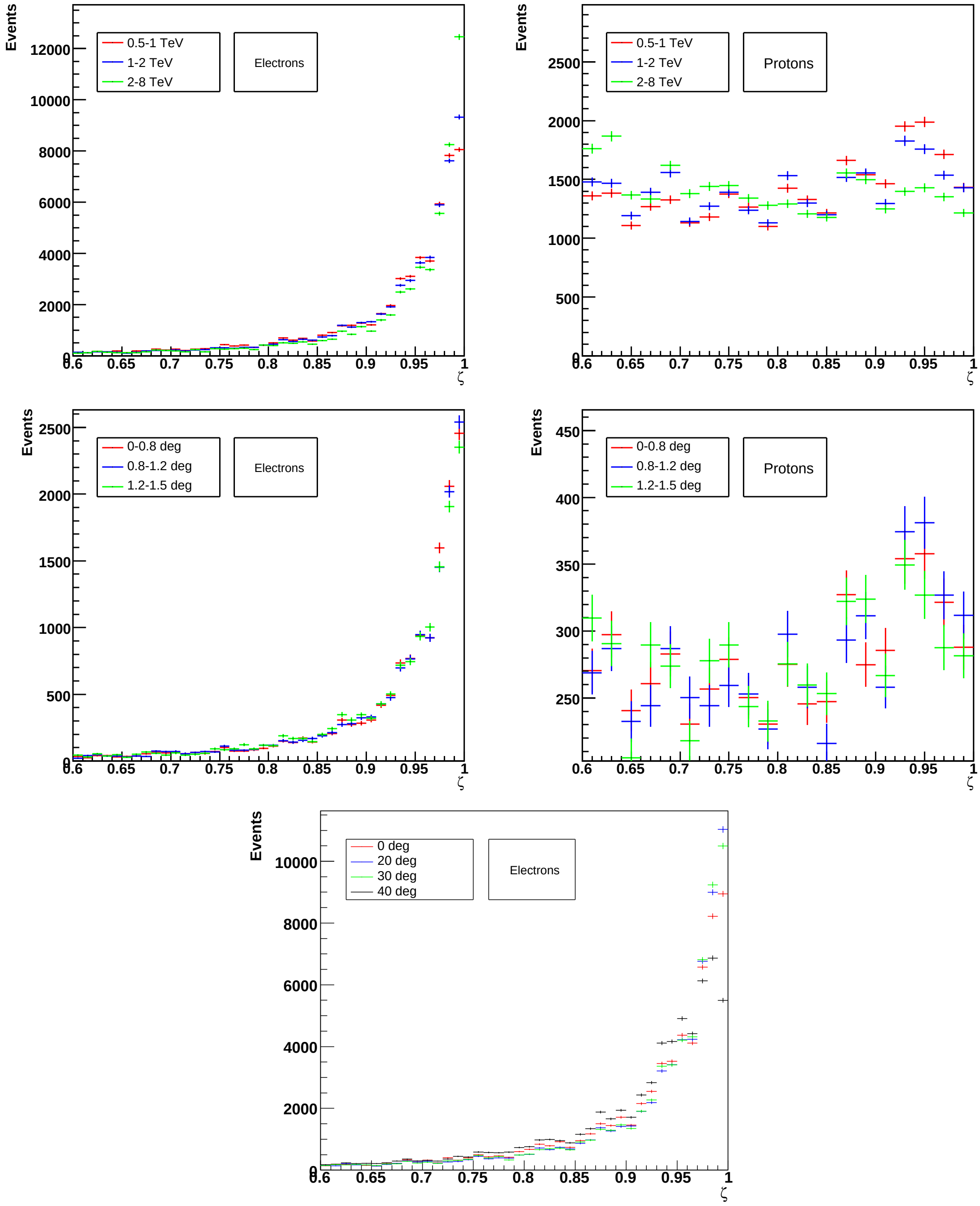

Figure 3.5: The dependencies of the ζ distribution for simulated electrons and protons. *Top*: The dependence on energy. For three different bands in energy, electron simulations are shown in the left panel, and proton simulations in the right panel. *Middle*: The dependence on the offset from the camera centre. For three different offset bands electron simulations are shown in the left panel, proton simulations in the right panel. The simulations cover an energy range of 0.7–4 TeV. *Bottom*: The dependence on zenith angle. Electron simulations are shown at zenith angles of 0°, 20°, 30° and 40°. The simulations cover an energy range of 0.7–4 TeV. There is no comparison of proton simulations, because they are simulated only at 20° zenith angle.

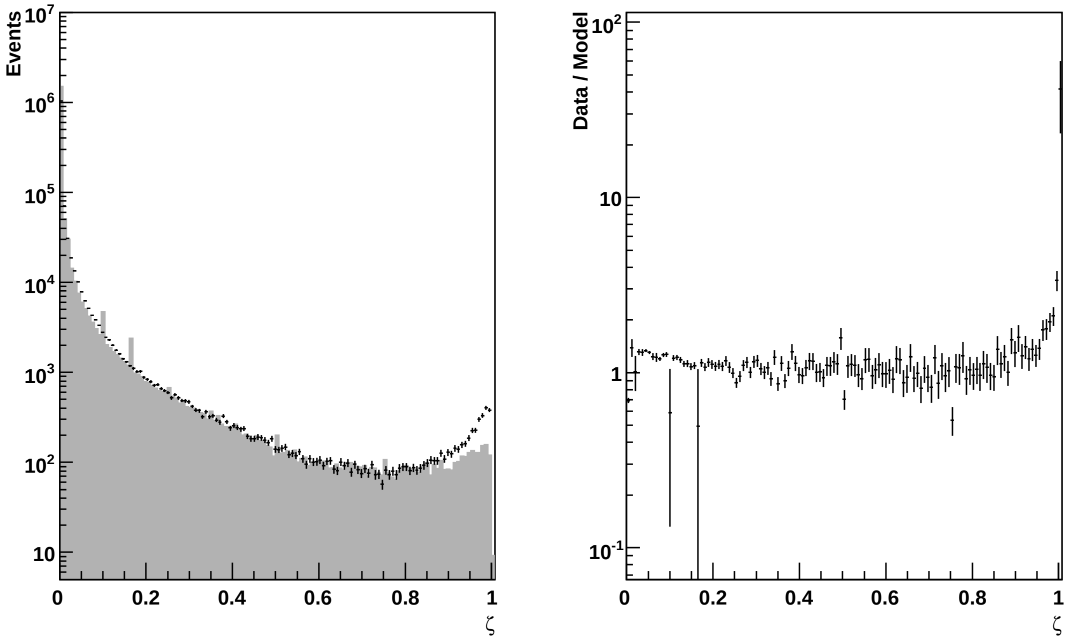

Figure 3.6: Comparison of ζ distributions of simulations and data in the energy range of 1-4 TeV. *Left*: ζ distribution of data and a mixed composition (proton, He, N, Si & Fe) cosmic-ray model. The model distribution is normalised to the data in the range of ζ of 0.1 to 0.6. At $\zeta < 0.1$, there are some systematic discrepancies between simulations and data, and at $\zeta > 0.6$, the electron component in the data sets in. The spikes in the model distribution at low ζ are a relic of the heavier nuclei with their low event numbers and large statistical errors. *Right*: The ratio of the data and the model of simulations shown in the left panel. While for small ζ this ratio is flat, for large values of ζ an excess of electromagnetic showers is observed.

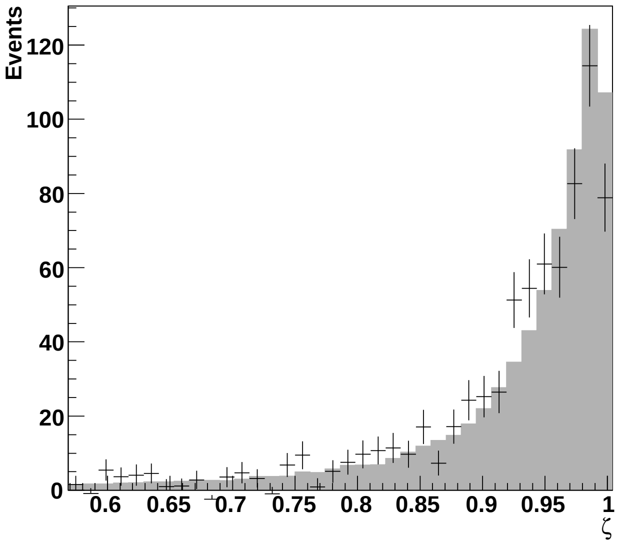

Figure 3.7: ζ distribution of background subtracted γ-ray data of Sgr A* (black data points) and γ-ray simulations (grey histogram). For the background subtraction the *reflected region method* of the H.E.S.S. standard analysis is used.

3.3 Background Determination

Despite the considerable background suppression obtained by the ζ cut, the data still contains electrons and background events in the signal region. Therefore, a mechanism is needed to estimate the background level in the data set. Since cosmic-ray electrons arrive isotropically at Earth, no comparative measurement of the electron-free background is possible. Thus, the background is determined by means of simulations in the phase space of the separation parameter ζ.

3.3.1 The Likelihood Fit

In order to evaluate the contribution of background of hadronic cosmic rays and the contribution of electron events in the data, a fit is applied to the ζ distribution, matching a combination of simulated electrons and protons to the data. This fit is applied in independent energy bands in order to obtain the number of electrons per energy band and from that the electron spectrum. For the fit with electron and proton simulations to work, two key requirements are needed:

1. The background has to consist of protons only, and
2. The simulations have to describe the reality well enough to reproduce the ζ distribution of the data.

The first condition is shown to be fulfilled in Fig. 3.3. The second condition is the most critical part of the analysis. As already discussed in Chapter 2.1, the use of proton simulations introduces large systematic uncertainties arising from lacking knowledge of the relevant strong interaction physics at TeV energies. For an estimation of this systematic uncertainty, two hadronic interaction models are compared: SIBYLL and QGSJET-II.

For the fitting procedure a maximum likelihood estimation is chosen because of small numbers both in data and simulations. The logarithm of the likelihood function is given by

$$\lg \mathrm{L} = \sum_{i=1}^{n} \lg \mathrm{L}_i \quad , \tag{3.1}$$

with L_i being the likelihood function in the ith bin of the ζ distribution. L_i is given by the Poisson distributions of the electrons, protons, and the data:

$$\begin{aligned} \mathrm{L}_i &= P(p_i|\tilde{p_i}) \cdot P(e_i|\tilde{e_i}) \cdot P(d_i|r \cdot \tilde{e_i} + s \cdot \tilde{p_i}) \\ &= \frac{\tilde{e_i}^{e_i}}{e_i!} e^{-\tilde{e_i}} \cdot \frac{\tilde{p_i}^{p_i}}{p_i!} e^{-\tilde{p_i}} \cdot \frac{(r \cdot \tilde{e_i} + s \cdot \tilde{p_i})^{d_i}}{d_i!} e^{-r \cdot \tilde{e_i} - s \cdot \tilde{p_i}} \quad , \end{aligned} \tag{3.2}$$

where e_i, p_i and d_i denote the number of events in bin i of the electron, proton, and data distributions and $\tilde{e_i}$ and $\tilde{p_i}$ their true values. The Poisson distribution of the data contains the condition that the true value of each data bin can be expressed as sum of the true electron bin content and the true proton bin content: $r \cdot \tilde{e_i} + s \cdot \tilde{p_i}$, the free parameters r and s being respectively the fraction of the total number of simulated electrons and protons in the signal region $\zeta > 0.6$. The fraction of electrons in the data can be calculated from these parameters via $f_e = \frac{r \cdot N_e}{N_{\text{data}}}$, with N_{data} the number of data events and N_e the number of electron simulations, both in the region of $\zeta > 0.6$. A similar procedure gives f_p, the fraction of protons.

Due to the use of Poisson distributions, the fit expects discrete events rather than weighted distributions. To account for this, the weighted ζ distributions, ζ_{w}, are scaled such that they sum up to the total number of events, i.e. by a scaling factor $\int \zeta_{\text{uw}} / \int \zeta_{\text{w}}$ containing the unweighted ζ distribution, ζ_{uw}. This is a good approximation for the case of high statistics but leads to biases if in any of the weighted distributions are only few entries in a bin. Fits are done for narrow energy bands, so weights are roughly constant for each fit. To test the quality of the fit, results were compared with a χ^2 fit, which is presented in Section 3.7.

The likelihood function defined in Eqns. (3.1) and (3.2) has a total of $2n + 2$ free parameters if n denotes the number of bins in the ζ distribution. The fitting aims at the determination of the optimal r that maximises the likelihood function. The true values $\tilde{e_i}$ and $\tilde{p_i}$ are of no interest, and the maximum likelihood has to be determined for all possible values of $\tilde{e_i}$ and $\tilde{p_i}$. For a maximisation of the likelihood with respect to r, the sum over the likelihoods of all possibilities of $\tilde{e_i}$ and $\tilde{p_i}$ has to be performed, with unlikely $\tilde{e_i}$ and $\tilde{p_i}$ contributing accordingly less:

$$\lg \mathrm{L}\,(r, s) = \sum_i \sum_{\tilde{e_i}} \sum_{\tilde{p_i}} \lg \mathrm{L}_i \ . \tag{3.3}$$

This tedious equation is simplified by the use of optimised values of the true values $\tilde{e_i}$ and $\tilde{p_i}$ instead of summing over their whole distribution:

$$\frac{\partial}{\partial \tilde{e_i}} \mathrm{L}_i = 0 \ , \tag{3.4}$$

$$\frac{\partial}{\partial \tilde{p_i}} \mathrm{L}_i = 0 \ . \tag{3.5}$$

This optimisation is carried out analytically and results in a likelihood function expressed only in terms of r and s, which speeds up considerably the subsequent numerical maximisation of the likelihood function with respect to r and s.

In Fig. 3.8 the two-dimensional likelihood function in terms of electron fraction r and proton fraction s is shown. The anticorrelation between r and s is easily explained by the fact that independently of the shape, both fractions give positive contributions to the fixed total number of events. The cross marks the optimum found by the fit, and the contours indicate the 1, 2, and 3 σ errors, i.e. the lines at which the logarithm of the likelihood falls below 0.5, 2, and 4 of its maximum value. $1\,\sigma$ errors on the fitted value of r are determined by the maximum extension of r in the $1\,\sigma$ contours of the likelihood function. However, if there are correlations between the $2n$ true values, $\tilde{e_i}$ and $\tilde{p_i}$, and r, this error will be underestimated. This possibility is discussed in Section 3.3.2.

The results of the fits in independent energy bands are shown in Fig. 3.9. The numbers of events are summarised in Table 3.3. A good agreement between the best fit model and the H.E.S.S. data points is observed. This impression is confirmed by the goodness-of-fit,

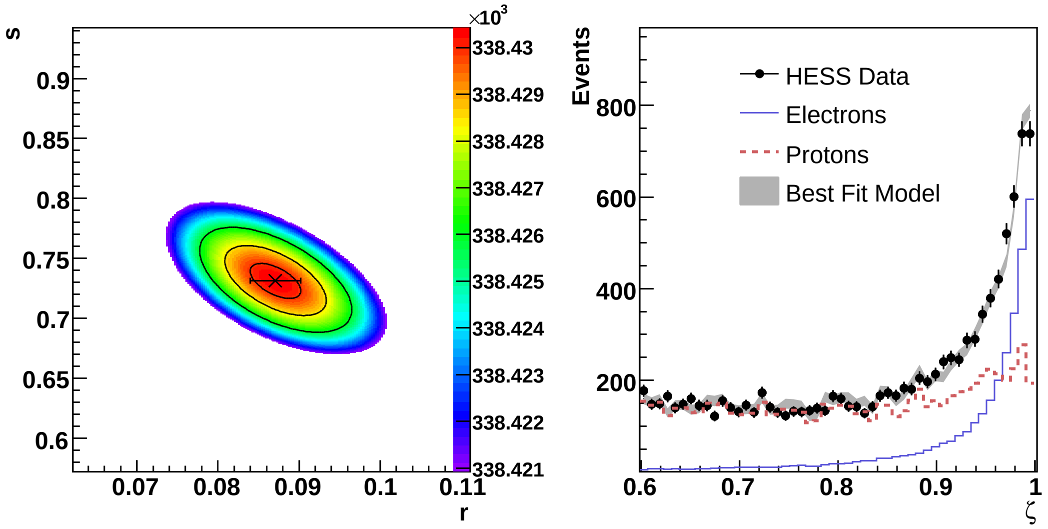

Figure 3.8: Example of a likelihood distribution and a fit in the ζ distribution for the energy range of 1–4 TeV: *Left*: The likelihood distribution. The cross marks the maximum, $1\,\sigma$ errors on r are indicated by the error bars. The contours describe the lines of 1, 2, and 3 σ deviations. The best fit position is $(r,\,s) = (0.087,\,0.73)$. With total event numbers of 38,173 electron simulations, 10,444 proton simulations, and 10,962 data events, the fit yields an electron fraction of $f_e = 30.3\%$ and a proton fraction of $f_p = 69.7\%$. *Right*: The fitted ζ distribution. The H.E.S.S. data are shown as black data points, the grey shaded band is the best fit model consisting of 30.3% electrons and 69.7% protons. Also shown are the single contributions to the fit, i.e. the proton distribution (red, dashed line) and the electron distribution (blue, solid line).

which is determined by the means of a χ^2 evaluation:

$$\chi^2 = \sum_i \frac{(d_i - m_i)^2}{\sigma_{d_i}^2 + \sigma_{m_i}^2}\ , \tag{3.6}$$

where d_i denotes the number of events in bin i of the data ζ distribution, m_i the number of events in this bin of the model distribution consisting of protons and electrons, and σ_{d_i} and σ_{m_i} are the corresponding standard deviations. For Fig. 3.9 the χ^2/ν values are summarised in Table 3.4 together with a comparison of the χ^2/ν values for a fit using the QGSJET-II simulations (the fit in the ζ distribution with proton simulations using the QGSJET-II model is shown in the Appendix in Fig. A.1).

The likelihood fit is cross-checked with a χ^2 fit and both fitting methods give consistent results[9].

3.3.2 Error Calculation

In the fitting procedure, errors are determined by taking the maximum extension of the 1σ contours of the likelihood function along the x axis as statistical errors for r. If there are

---

[9] See the systematic tests in Section 3.7.

Energy (TeV)	Data	Electrons	Protons
0.62-0.81	10435	3490	6934
0.81-1.0	6382	2230	4145
1.0-1.4	4385	1480	2901
1.4-1.8	2682	728	1951
1.8-2.3	1530	443	1086
2.3-3.0	913	168	744
3.0-3.9	485	60	424
3.9-6.6	439	90	348
6.6-14.5	267	36	231

Table 3.3: The measured number of data events and the calculated numbers of electrons and protons (with the SIBYLL interaction model) in the energy bands. Electron and proton events sum up to the true number of data events, which can slightly differ from the measured number of data events.

Energy (TeV)	SIBYLL	QGSJET-II
0.62-0.81	32.6/31 (0.39)	42.2/31 (0.09)
0.81-1.0	24.1/31 (0.81)	34.4/31 (0.31)
1.0-1.4	26.8/31 (0.68)	33.3/31 (0.36)
1.4-1.8	32.8/31 (0.38)	26.5/31 (0.70)
1.8-2.3	25.1/31 (0.76)	26.9/31 (0.68)
2.3-3.0	38.8/31 (0.16)	33.1/31 (0.36)
3.0-3.9	23.3/31 (0.84)	34.6/31 (0.30)
3.9-6.6	39.5/31 (0.14)	24.4/31 (0.79)
6.6-14.5	32.2/31 (0.41)	34.4/31 (0.31)

Table 3.4: The χ^2/ν values for the two different hadronic interaction models SIBYLL and QGSJET-II. The corresponding probabilities are given in brackets.

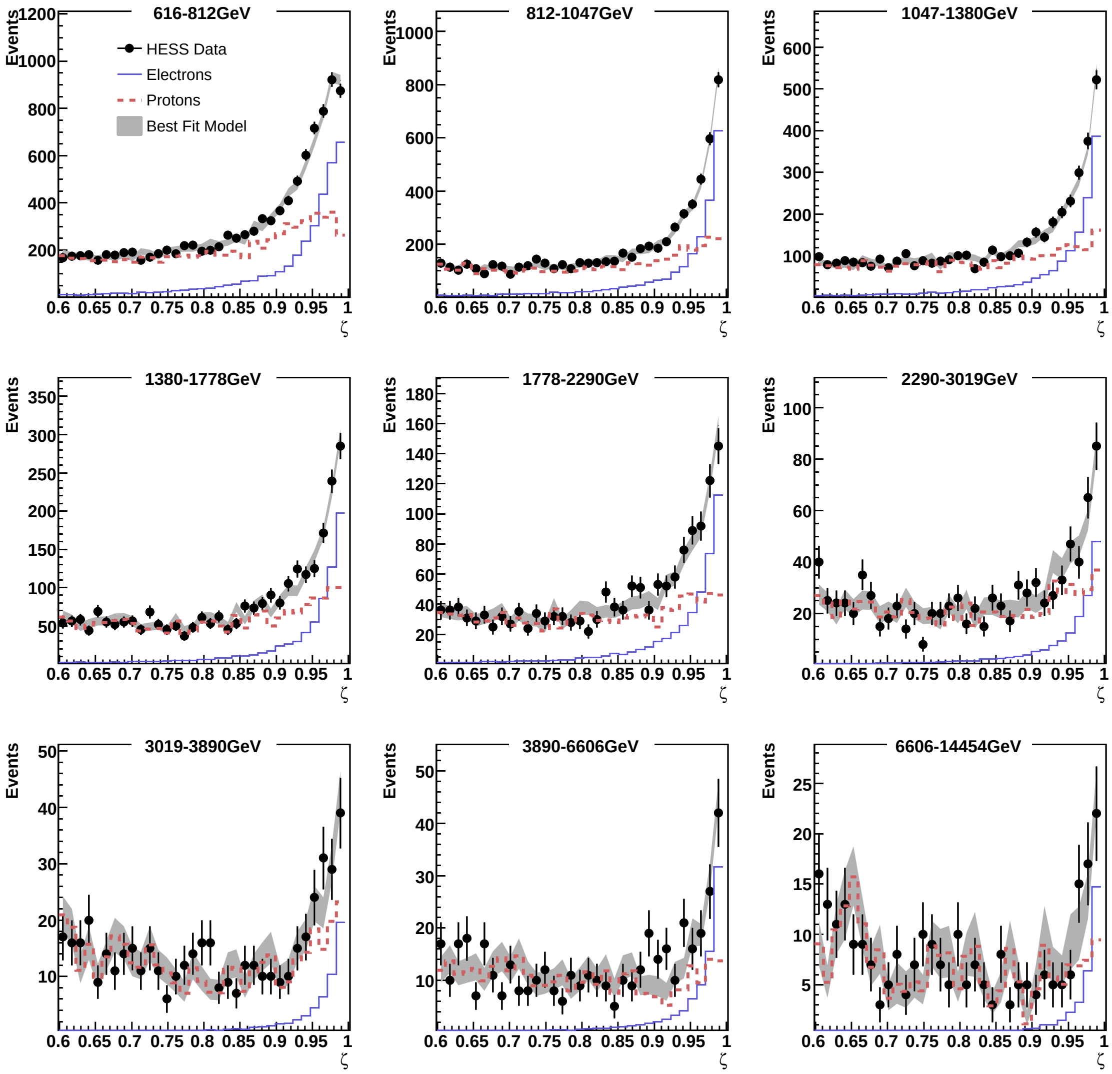

Figure 3.9: Fit in ζ distribution in the energy bands that are used for the spectrum. H.E.S.S. data are shown in black points, and the best fit model as shaded band. The contributions to the model by electrons are shown in blue, and the proton contribution in form of the red dashed line. Cuts A have been applied.

no correlations between the $2n$ true values of the electron and proton ζ simulations and r, this error represents the total statistical error of the electron fraction r. However, if there is a small correlation between r and any true value $\tilde{x}_i$ with $\tilde{x} = \tilde{p}$, $\tilde{e}$, and i an arbitrary bin number, the error on r will be underestimated by simply taking the optimised value for $\tilde{x}_i$ and continuing the calculation with this value. This can be seen from the schematic drawing of Fig. 3.10. Therefore, the deviations of the errors determined by the fitting procedure from the true errors are investigated separately.

The true errors are determined by the spread in the fitting results for generated Monte Carlo simulations that scatter with finite statistics around an assumed true distribution.

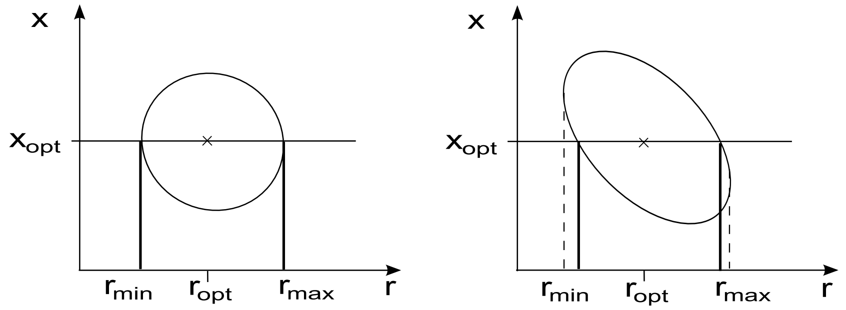

Figure 3.10: Illustration of the underestimation of errors in case of parameter correlation. On the left a situation is sketched where parameters x and r are independent. The maximum extension of the $1\,\sigma$ contours in r is reached at the optimised value x_{opt}. Thus, the error is estimated correctly. On the right, the parameters x and r are correlated. Here the determination of the errors r_{min} and r_{max} at the position of x_{opt} underestimates the errors (solid thick line). The true errors r_{min} and r_{max} are indicated by the dashed line.

For this purpose, the ζ distributions of Monte Carlo electrons and protons are fitted in each energy band that is used for the spectrum determination and in the following they are represented by their fitting functions $\tilde{e}$ and $\tilde{p}$. A model is constructed by the sum of $\tilde{e}$ and $\tilde{p}$ weighted by r and s resulting from the fit in each energy band: $r \times \tilde{e} + s \times \tilde{p}$. This model now matches approximately the data.

The fitted functions are assumed to correspond to the true distributions and they are used to generate Monte Carlo distributions with the statistics of the original distributions, Poisson distributed around the true values. This is done for the electron, proton, and the model distributions. The newly generated distributions are then fed into the fitting algorithm and new values for the electron and proton fraction r and s are determined. The scatter of these new electron and proton fractions, r_{MC} and s_{MC}, around the original ones, r_{true} and s_{true}, is a measure for the error of the fitting algorithm.

When plotting the deviation of the newly calculated electron fraction from the original value divided by the error of the best fit value of the Monte Carlo distributions $(r_{\mathrm{MC}} - r_{\mathrm{true}})/\Delta r$, a Gaussian distribution centered at zero is expected. This Gaussian has a root mean square (RMS) consistent with 1 if the errors of the fitting procedure were calculated correctly. If they are underestimated, the results of the fit of the Monte-Carlo-generated distributions scatter broader around their true value, and the RMS of $(r_{\mathrm{MC}} - r_{\mathrm{true}})/\Delta r$ is larger than 1. As the errors cannot be assumed to be symmetric, a separate treatment of the upper and lower error is necessary. Therefore, the data are split depending on whether the fitting procedure of the Monte Carlo simulations underestimates the true value or overestimates it. If $r_{\mathrm{MC}} > r_{\mathrm{true}}$ the data is used to investigate the lower error of r_{MC}. If $r_{\mathrm{MC}} < r_{\mathrm{true}}$ the data is used to investigate the upper error of r_{MC}.

The figures of the fits, the scattering plots of the r and s values, and the $(r_{\mathrm{MC}} - r_{\mathrm{true}})/\Delta r$ distributions are shown in the Appendix (Fig. A.2, A.3, A.4, A.5, A.6, A.7, and A.8). The RMS values for lower and upper errors come to $\approx$1.1. Therefore, the fitting procedure underestimates the errors by approximately 10%. This has to be kept in mind when interpreting spectra.

To a certain extend, this error calculation incorporates also a test of the fitting function: it proves that the fitting is reproducible in the sense that feeding into the algorithm a true value r_{true} results in a Monte Carlo distribution r_{MC} scattered around r_{true}, which can be seen in Fig. A.5.

3.4 Data Selection

The data set is selected carefully in order to minimise systematic effects and contamination of the data with background. Since γ rays are extremely difficult to distinguish from electrons but arrive at Earth anisotropically, the main task of the data selection is to avoid any region of γ-ray emission. Only *extragalactic* observations are included since diffuse γ-ray emission is expected from the Galactic plane. Also any known or potential γ-ray source is excluded. Possible contamination by diffuse extragalactic γ rays was already discussed in Chapter 1.4.

The quality of the data is also critical for the analysis. Since changes in the atmosphere influence the system trigger rate and therefore the total flux normalisation, the data selection is an important feature for any spectral analysis (in contrast to a source detection, where the aim is a high accumulated significance in the signal rather than a quantification of the flux). Therefore, special care has been taken in the selection of good-quality runs for this analysis.

Reasons for bad data quality can be either atmospheric conditions or technical reasons. Bad weather conditions can be identified by the total trigger rate, which is expected to be constant over time. A sudden drop in trigger rate indicate clouds or dust blocking the Cherenkov light and thus making spectral studies with the affected observation run impossible. Therefore, in the standard H.E.S.S. run selection a minimum trigger rate is defined and runs with trigger rates below this threshold are excluded. The minimum trigger rate is time dependent as the trigger rate itself decreases over time and reflects adjustments conducted at the cameras. For the electron analysis, this cut is tightened and the standard minimum trigger rate is increased by a factor of 1.2. Technical problems can occur due to failure of various components. Observations with fewer than four participating telescopes are excluded immediately from the data set. In a camera, single pixels can be switched off to avoid damages due to bright stars, shooting stars, or lightning. The deficiency of many pixels in a camera can result in distorted shower images and thus a faulty reconstruction.

In summary, the data used for this analysis fulfill the following criteria:

- Only extragalactic targets with a minimum of 7° distance to the Galactic plane are used,
- Only 4-telescope observations, and
- Only observations under good weather conditions (trigger rate $> 1.2\times$ minimum trigger rate of the H.E.S.S. standard run selection), with
- Less than 400 pixels in all four telescopes not operational.

In addition, the zenith angle range is restricted to angles smaller than 28° since proton simulations were available at 20° only. The zenith angle distribution of the data set is

shown in Fig. 3.11. The mean zenith angle of the observation is 17°.
The central 3° of the field of view was used; any known or potential γ-ray source was amply excluded within 0.4° radius. The resulting distribution of the square of the offset in the camera is shown in Fig. 3.12. Almost all extragalactic sources detected so far by H.E.S.S. are point-like, i.e. they cannot be resolved within the H.E.S.S. point spread function of $\sim 0.1°$. Since 4-telescope events generally have a good direction reconstruction, an exclusion radius of 0.4° guarantees the exclusion of γ rays even in the case of the bright flare of PKS 2155-304 in 2006[10].
Consistency checks with different data sets have shown that the electron spectrum obtained from the data does not depend on the target[11].
The above mentioned conditions result in a live-time of 239 hours and a total exposure at 1 TeV of $\approx 8.5 \times 10^7\ \mathrm{m}^2\,\mathrm{sr}\,\mathrm{s}$. The data set contains mostly AGN observations, a list of targets with their position and the observation time is given in Table 3.5. The distribution of the selected events in the sky is shown in Fig. 3.13.

With these data the spectrum of cosmic-ray electrons is now determined in the following section.

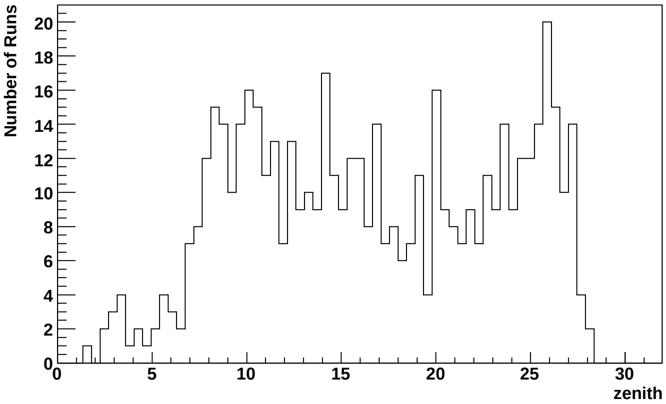

Figure 3.11: The distribution of the mean zenith angle per run of the data set specified in Table 3.5.

---

[10] For details see Chapter 2.2.6.

[11] See Section 3.7.

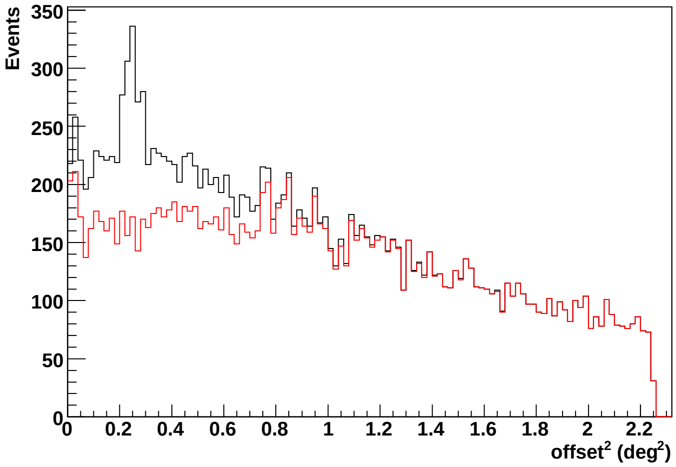

Figure 3.12: The distribution of offset^2 of the data set. Cuts A are applied additionally to the $\zeta > 0.6$ cut and only events with energies above 0.62 TeV are included. In the black histogram γ-ray sources are not excluded, and in the red histogram, sources are excluded with a radius of 0.4°. The contribution of γ-ray sources at an offset of 0.5° is clearly visible.

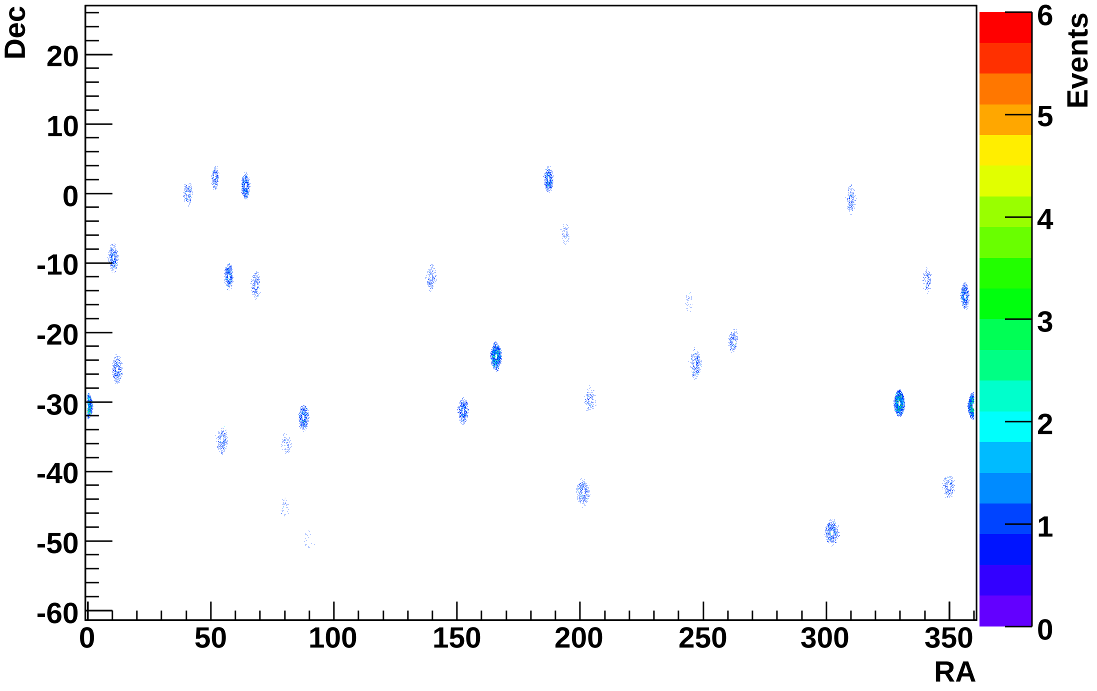

Figure 3.13: The distribution of the selected events in the sky. Coordinates are given in right ascension (RA) and declination (Dec).

Target	RA	Dec	Observation time (hours)
H 2356-309	359.7825	-30.6275	49.18
PKS 2155-304	329.7167	-30.2256	40.72
1ES 1101-232	165.9071	-23.4919	29.64
PKS 0548-322	87.6688	-32.7711	12.50
1RXS J101015.9-311909	153.1514	-31.3193	11.20
1ES 0414+009	64.2183	1.0900	11.13
1ES 0347-121	57.3467	-11.9908	9.50
PKS 2005-489	302.3558	-48.8314	9.86
NGC 253	11.8880	-25.2883	8.83
3C 273	187.2779	2.0524	9.37
1ES 2343-151	356.4075	-14.8194	9.39
ACO 85	11.1094	-9.3333	7.51
Cen A	201.3666	-43.0192	6.05
rho Oph B cloud	246.7958	-24.4750	5.40
NGC 1399	55.4843	-35.4500	5.24
PKS 2316-423	349.7750	-42.1133	3.21
Kepler SNR	262.6700	-21.4864	3.76
AE Aqr	310.0382	-0.8709	3.76
3C 218	139.5238	-12.7953	3.75
1ES 0323+022	51.5579	2.4206	3.62
RBS 1888	340.925	-12.5183	2.36
NGC 1068	40.6696	-0.5130	2.74
Abell 496	68.4075	-13.2619	2.82
M 83	204.2533	-29.8663	2.34
PKS 0521-365	80.7417	-36.4586	1.14
ACO 496	68.4000	-13.9333	1.41
3C 279	194.0461	-6.2891	1.26
Sco X-1	244.2648	-15.6433	0.47
PKS 0558-504	89.9474	-49.9475	0.47
Pictor A	79.9570	-45.7790	0.47

Table 3.5: Targets of the observation runs used for the electron analysis. Positions are given in right ascension (RA) and declination (Dec).

3.5 Spectrum Determination

After the number of electrons in each energy band is determined, a differential energy spectrum of cosmic-ray electrons can be calculated. The differential energy spectrum is defined as the number of electrons per energy bin and solid angle, unit time, and unit area:

$$\frac{dF}{dE} = \frac{N(E)}{A_{\text{eff}}(E) \cdot \Delta E \cdot T \cdot \Omega} \ . \tag{3.7}$$

Here, A_{eff} is the effective collection area, T the livetime of the observation, Ω the solid angle, and ΔE the size of the energy band. The effective collection area is the product of the total collection area (which itself is a function of energy) and the cut efficiency (which is also energy dependent). It is determined by means of simulations and is presented in Section 3.5.1.

Before a spectrum can be determined according to Eqn. (3.7), the effect of the degradation of mirrors over time[12] has to be corrected. Due to the steep spectrum of cosmic-ray electrons, this effect is large and needs a careful evaluation. This is described in Section 3.5.2.

3.5.1 Effective Collection Area

The effective collection area is determined from Monte Carlo electron simulations as the fraction of generated events per area that have triggered and passed all selection cuts:

$$A_{\text{eff}}(E) = \frac{N_e^{\text{sel}}(E) \cdot A^{\text{MC}}}{N_e^{\text{MC}}(E)} \ , \tag{3.8}$$

$A_{\text{eff}}(E)$ is a function of the true energy of the simulations. But because of the good energy reconstruction of the electron simulations, $A_{\text{eff}}(E_{\text{true}})$ can be approximated by $A_{\text{eff}}(E_{\text{reco}})$[13]. A^{MC} is the area over which simulations are generated. This definition comprises the collection area of the H.E.S.S. telescopes, the detection efficiency of the system, and the analysis cuts. The effective area depends on zenith angle, offset in the camera, and energy. In order to take into account the steep electron spectrum with a spectral index of $\approx$3.3 (while the simulations are generated with an index of 2.0), the events used for the effective area generation are weighted. This is done analogously to the weighting of the ζ distributions described in Chapter 3.2 with weighting factors of $(E_{\text{true}}/0.1\,\text{TeV})^{-1.3}$. For the normalisation, the effective areas are divided in each energy bin E_i by the weighting factor corresponding to this bin. Thus, the effective area in the energy bin E_i is the weighted sum over all selected electron events with reconstructed energy contained in this bin, $N_e^{\text{sel}}(E_{\text{reco}} \in \text{bin}\, E_i)$, scaled by the ratio of the simulated area over the number of generated electron events with energy in bin E_i and divided by the average weight:

$$A_{\text{eff}}(E_i) = \frac{A^{\text{MC}}}{N_e^{\text{MC}}(E \in \text{bin}\, E_i)} \left(\sum_{N_e^{\text{sel}}(E_{\text{reco}} \in \text{bin}\, E_i)} \left(\frac{E_{\text{true}}}{0.1\,\text{TeV}} \right)^{-1.3} \right) \Bigg/ \left(\frac{E_i}{0.1\,\text{TeV}} \right)^{-1.3} \ .$$

---

[12] See Chapter 2.2.

[13] The total number of simulated electrons $N_e^{\text{MC}}(E)$ is always a function of true energy. This is because not all events trigger the telescope array and are reconstructed, and therefore, they do not have a reconstructed energy.

(3.9)

As for all data sets the whole field of view is used (neglecting the small effect of the excluded γ-ray source regions) the offset distribution is always the same and taken into account by the use of diffuse simulations. Effective areas are determined for the zenith angles at which electron simulations are available (0°, 20°, 30°, 40°), and then interpolated to match the zenith distribution of the data. The zenith angle distribution of the data is used and for each bin in zenith angle, weighting factors are calculated as a linear combination of the contribution of the two neighbouring zenith angle bands. Summing over all bins, the smooth zenith distribution of the data is transformed into a discrete distribution of the bands of zenith angle. This discrete distribution now contains the relative contribution of each zenith band to the zenith distribution of the data.

An independent approach of determining the effective areas justifies the neglect of the offset effect of the exclusion regions. In this approach the field of view is divided in small bins and the effective areas and ζ distributions are determined for a small offset range by interpolating between bands of offsets. The comparison of the two methods is included in the systematic tests presented in Section 3.7.

The effective area as a function of energy is shown in Fig. 3.14 for different zenith angles. These effective areas contain only the standard $\zeta > 0.6$ cut and the requirement of all four telescopes triggering in the event. The effective areas displayed in Fig. 3.14 describe data taken at zenith angles of 0°, 20°, 30°, 40° for an optical efficiency of 100%. If applying

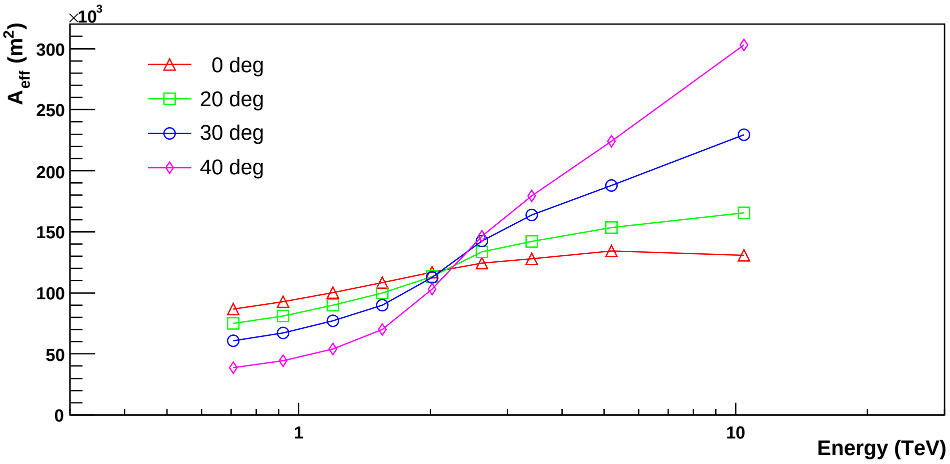

Figure 3.14: Effective areas for different zenith angles at 100% optical efficiency. Only the $\zeta > 0.6$ cut is applied.

additional hard event selection cuts, as done for the spectrum determination, the shape of the effective areas changes as shown in Fig. 3.15 for Cuts A and in Fig. 3.16 for Cuts B.

To determine now the effective areas not at fixed zenith angle and optical efficiency but with the zenith angle and optical efficiency distributions of the data set, the weighting in zenith angle that was described above has to be applied and the effective areas have to be corrected for the optical efficiency losses. The procedure of optical efficiency correction will be explained in the next section. The resulting effective collection area for the set of observation runs introduced in Section 3.4 is shown in Fig. 3.17, which illustrates the

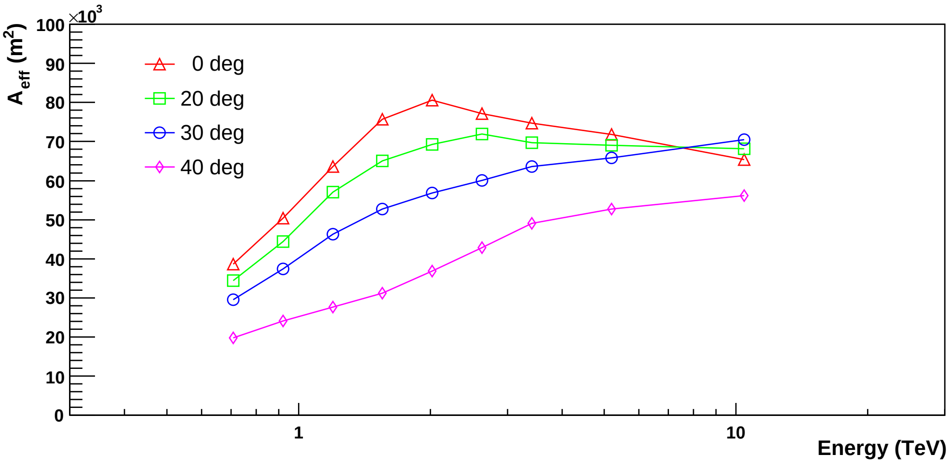

Figure 3.15: Effective areas with Cuts A for different zenith angles at 100% optical efficiency.

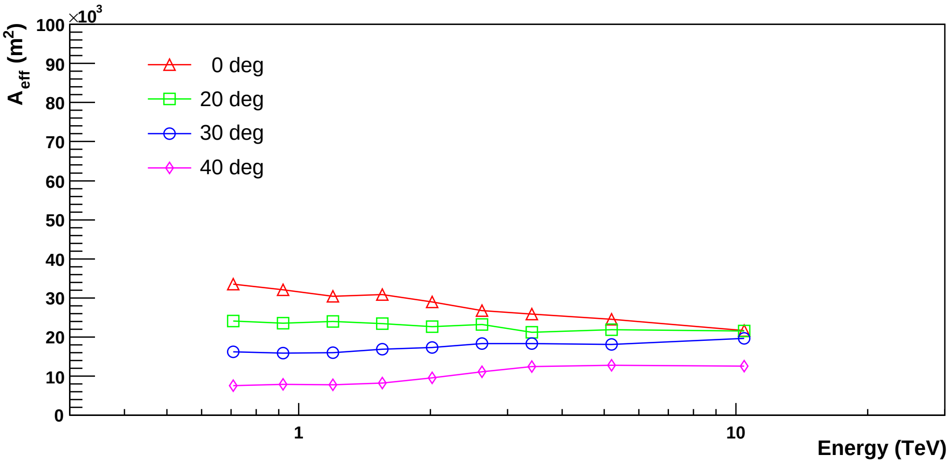

Figure 3.16: Effective areas with Cuts B for different zenith angles at 100% optical efficiency.

impact of different components of the event selection Cuts A on the chosen data set. The effective area for the low-energy spectrum with Cuts B is shown in Fig. 3.18. While at low energies it is the size cut that reduces the efficiency and therefore the effective areas, at high energies the cut on the shower's impact distance is the dominant effect. High energy showers are brighter and therefore on average detected at larger distances. The combined effect of size and impact distance cut reduces the number of detected electrons by more than a factor of two at most energies. This reduction of the number of events is justified because the analysis is not limited by statistics but systematic effects that are lessened by this event selection.

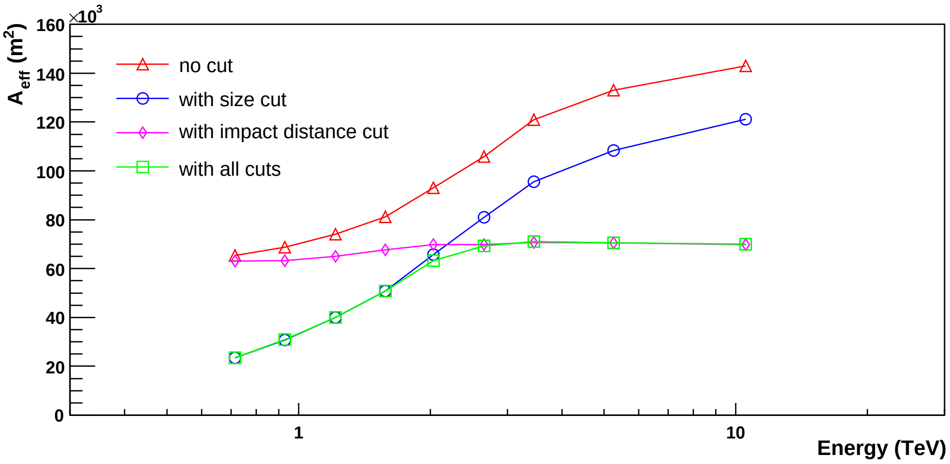

Figure 3.17: Effective areas for the data set used for this analysis. They contain the zenith angle distribution of the data set as well as corrections for a reduced optical efficiency. Shown are the effect of different cuts: Only a $\zeta > 0.6$ cut (red), additionally to the ζ cut a cut on the size of the camera image in each telescope of 200 p.e. (blue), a cut on the shower impact distance from the telescope array of 200 m (purple), and both the size and the distance cut (green).

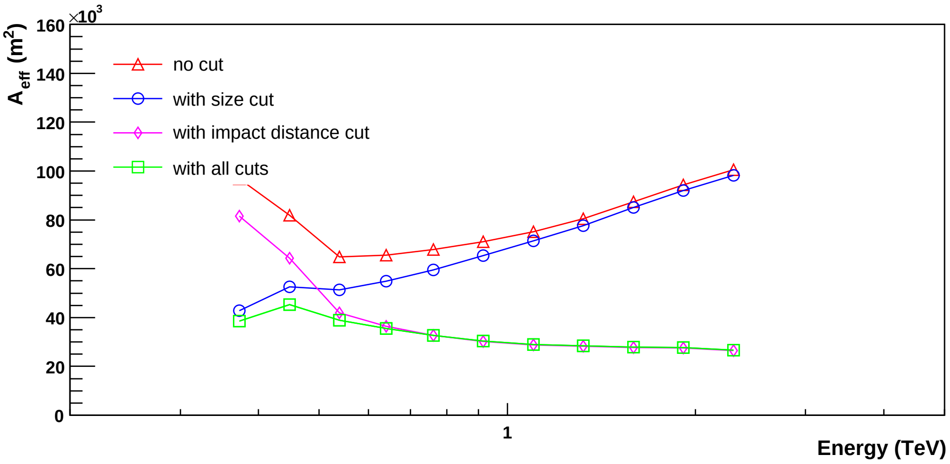

Figure 3.18: Effective areas for the low-energy spectrum. They contain the zenith angle distribution of the data set as well as corrections for a reduced optical efficiency. Shown are the effect of different cuts: Only a $\zeta > 0.6$ cut (red), additionally to the ζ cut a cut on the size of the camera image in each telescope of 80 p.e. (blue), a cut on the shower impact distance from the telescope array of 100 m (purple), and both the size and the distance cut (green).

3.5.2 Optical Efficiency Correction

In this analysis, simulations were used with a fixed optical efficiency of 100%, while the telescopes' efficiency slowly degrades over time. This degradation results in an energy that is reconstructed too low, which has to be corrected for in the analysis. While the determination of the energy correction factor from muon events was already mentioned in Chapter 2.2, this section is concerned with the application of this correction to the electron analysis and its energy dependent parameters.

A camera image taken with a telescope with reduced optical efficiency looks approximately like the image of a shower with less energy. This means that not only the shower's energy is reconstructed too low due to less intensity collected in the camera, but the whole shower image with all its other parameters appears like having lower energy. This is suggested by a comparison of ζ distributions of simulations with varying optical efficiency in Fig. 3.19. This finding implies that the (too low) reconstructed energy will determine the energy dependence of analysis parameters rather than the corrected energy. Thus, while the *corrected* energy is used to generate the energy spectrum, the *reconstructed* energy governs the energy dependence of any energy dependent parameter.

Since the data are collected over a time period of three years, a wide range of optical efficiencies are covered, thus having a spread of reconstructed energies corresponding to one corrected energy. This is shown in the distribution of the ratio of reconstructed energy E_{reco} to the corrected energy E_{corr} that is shown in Fig. 3.20. Energies are reconstructed between 20% and 40% too low. In order to be able to describe the data with simulations in energy dependent parameters like ζ, the same constellation of reconstructed energies is needed in the simulations and the data.

Energy dependent parameters in this analysis are the ζ distribution and the effective areas. The correction for both of them is described in the following.

Correction of the ζ distributions

In detail, the procedure to obtain the right ζ distribution of the simulations includes the following: the distribution of reconstructed energy is obtained from the relation of corrected to reconstructed energy of the data. For a chosen energy band of corrected energy the spread of reconstructed energies is determined. In Fig. 3.21 this is visualised exemplarily for the band of corrected energy 1.04–1.38 TeV. The corresponding range of reconstructed energies is 0.67–1.13 TeV. Each bin in the distribution of the reconstructed energy, E_i (see Fig. 3.21 right panel), contains the associated fraction f_i that gives the relative contribution of this reconstructed energy to the chosen band of corrected energy. These f_i are normalised: $\sum_i f_i = 1$.

To obtain the Monte Carlo ζ distribution corresponding to the chosen band in corrected energy (in the example this is 1.04–1.38 TeV), ζ distributions at reconstructed energies E_i, $\zeta(E_i)$, are determined and summed up, weighted by their relative contributions to the energy distribution f_i:

$$\zeta(E_{\mathrm{corr}}) = \left(\sum_i \zeta(E_i) \cdot f_i / N_i \right) \cdot \sum_i N_i \ , \tag{3.10}$$

with N_i being the sum of all entries in $\zeta(E_i)$. The division by N_i normalises the ζ distributions to 1. The single contributions to this sum for electrons and protons for the example of the band of corrected energy of 1.04–1.38 TeV are shown in the Appendix in Fig. A.9

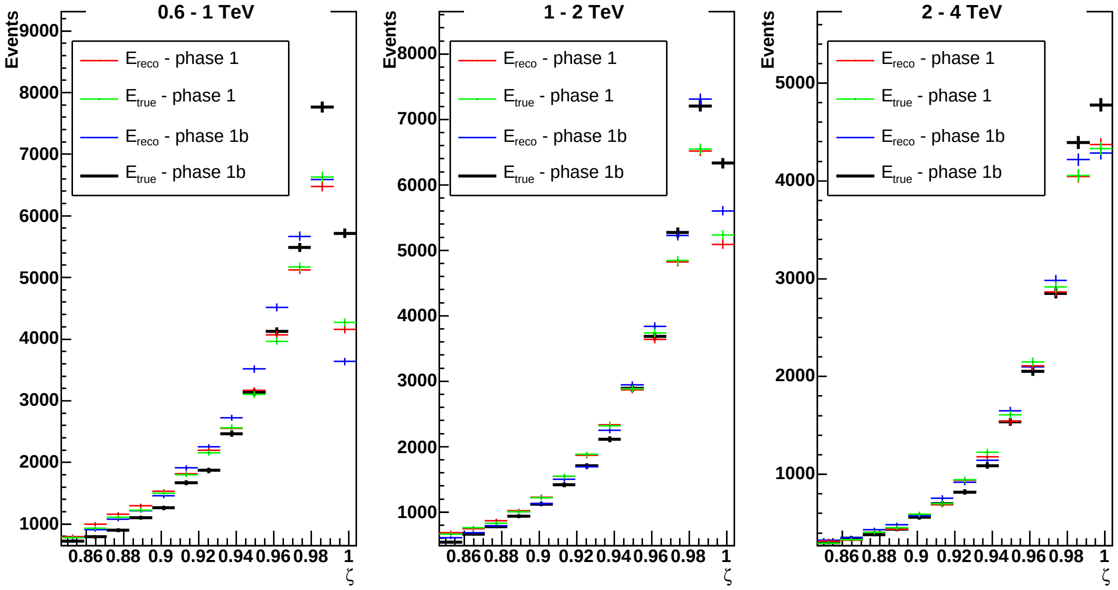

Figure 3.19: Test with γ-ray simulations with reduced optical efficiency. The ζ distributions are compared in three different energy bands for simulations with original (phase 1, red and green) and reduced efficiency of 70% (phase 1b, black and blue) with the energy cut applied to either reconstructed or true energy. As the energy is reconstructed using phase 1 simulations, the phase 1 ζ distributions do not differ much between true and reconstructed energy. The phase 1b simulations, however, show larger deviations. The best agreement of the phase 1b simulations with the phase 1 simulations is obtained by using the reconstructed energy, which validates the assumption that the reconstructed energy governs the energy dependence of parameters. However, the deviations demonstrate that this is only an approximation. This study is performed with γ rays because no electron simulations with reduced efficiency have yet been generated.

and A.10 respectively.

As the Poisson distribution of the fit in ζ needs the ζ distributions to have their original statistics, unweighted ζ distributions are finally used to approximately restore the statistics of the simulations. The unweighted ζ distributions are processed in the same way, i.e. summed over different reconstructed energies to determine the distribution in corrected energy. As Eqn. (3.10) keeps track of the total number of events by the means of the normalisation, $\sum_i N_i$, the statistics of the unweighted ζ distribution is restored and can be used to scale the weighted ζ distributions by the number of events in the unweighted distribution.

This method of weighted sums and subsequent restoration of the statistics by scaling with an integral value, which is applied here, is only approximately true because in the process of summing, the shape of the distributions is altered and only the integrated number of events is restored but not the bin-wise numbers. Therefore, this method contains the implicit assumption that the shape does not change dramatically, so the bin-wise numbers

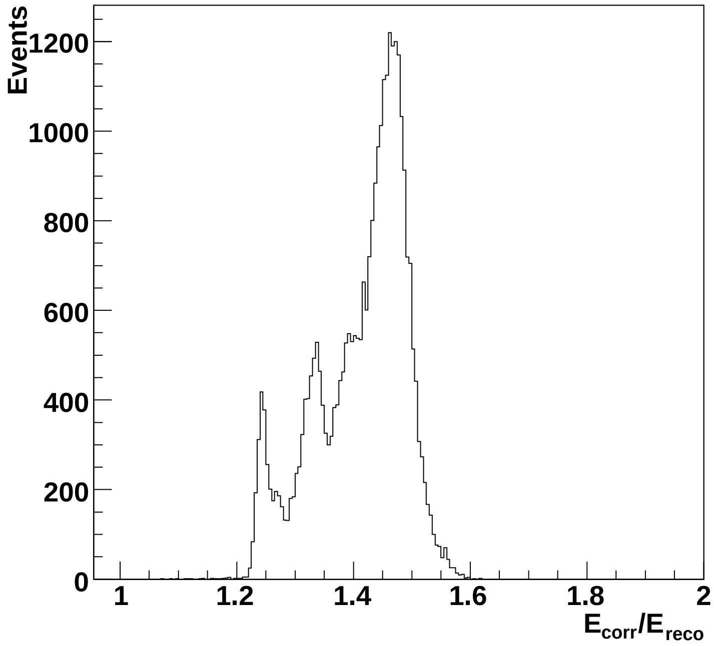

Figure 3.20: Distribution of the energy correction factor $E_{\mathrm{corr}}/E_{\mathrm{reco}}$ of the data set used for the spectrum determination.

are still approximated by this method. This seems justified by the similar shapes of the distributions shown in Fig. A.9 and A.10.

Correction of the effective areas

Regarding the effective areas, the correction is applied in an analogous way. The determination of corrected effective areas is furthermore simplified by the reduction by one dimension: for each reconstructed energy there is exactly one value for the effective area instead of a distribution as in the case of ζ. Effective areas as function of corrected energy are determined analogously to Eqn. (3.10):

$$A_{\mathrm{eff}}(E_{\mathrm{corr}}) = \sum_i A_{\mathrm{eff}}(E_i) \cdot f_i \; . \tag{3.11}$$

The corrected effective areas for the used data set were already shown in Fig. 3.17.

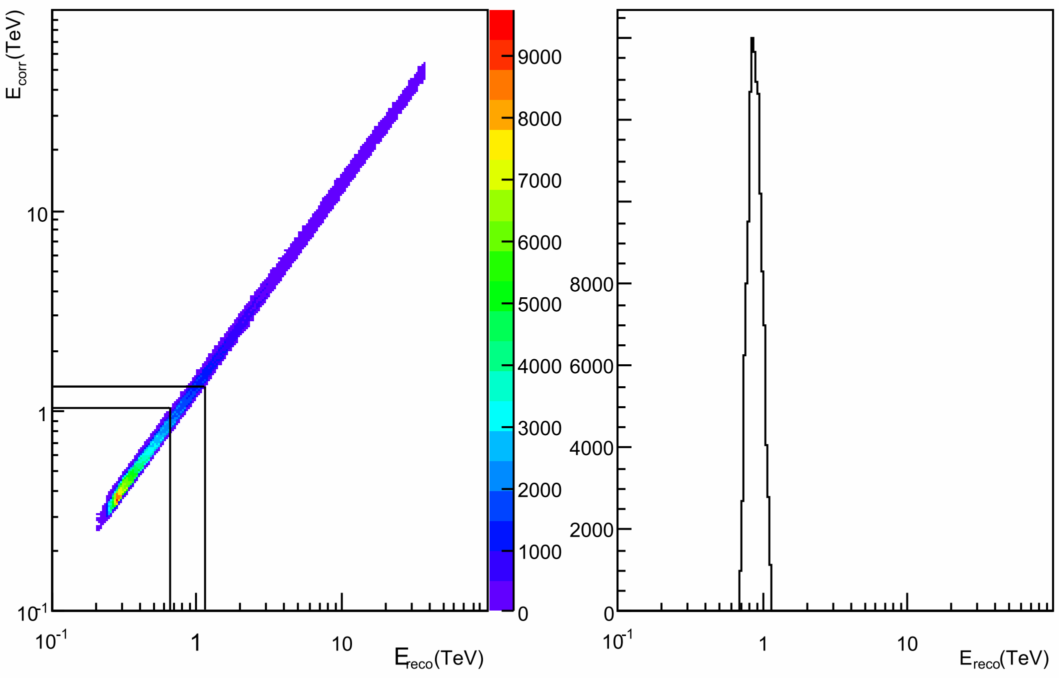

Figure 3.21: An example of the determination of the distribution of reconstructed energies for a chosen band of corrected energies: shown are in the left panel the relation between corrected and reconstructed energy of the data set. The black lines mark a band of corrected energy of 1.04–1.38 TeV and the corresponding range of reconstructed energies. The distribution of reconstructed energies in this band is shown in the right panel.

3.6 The Electron Spectrum

After the preparatory steps of the determination of the background and effective areas, and the correction for optical efficiency losses, now the spectrum of cosmic-ray electrons can be calculated according to Eqn. (3.7). The data set used for the spectrum generation is described in Chapter 3.4. The hard event selection cuts (Cuts A) specified in Table 3.1 are applied. The background estimation is by default done with proton simulations using the SIBYLL hadronic interaction model.

The cosmic-ray electron spectrum is shown in Fig. 3.22. In the left panel, the spectra obtained with both hadronic interaction models, SIBYLL and QGSJET-II, are shown. In the right panel, the electron spectra of independent data sets are compared. The error bars reflect the 1σ statistical errors obtained from the likelihood distribution as explained in Chapter 3.3. How this relates to prior, direct measurements can be seen in Fig. 3.23 and a zoom in the high-energy region of the spectrum in Fig. 3.24. At low energies, the spectrum has a steep slope. It exhibits a distinctive break at an energy of ≈3 TeV. At

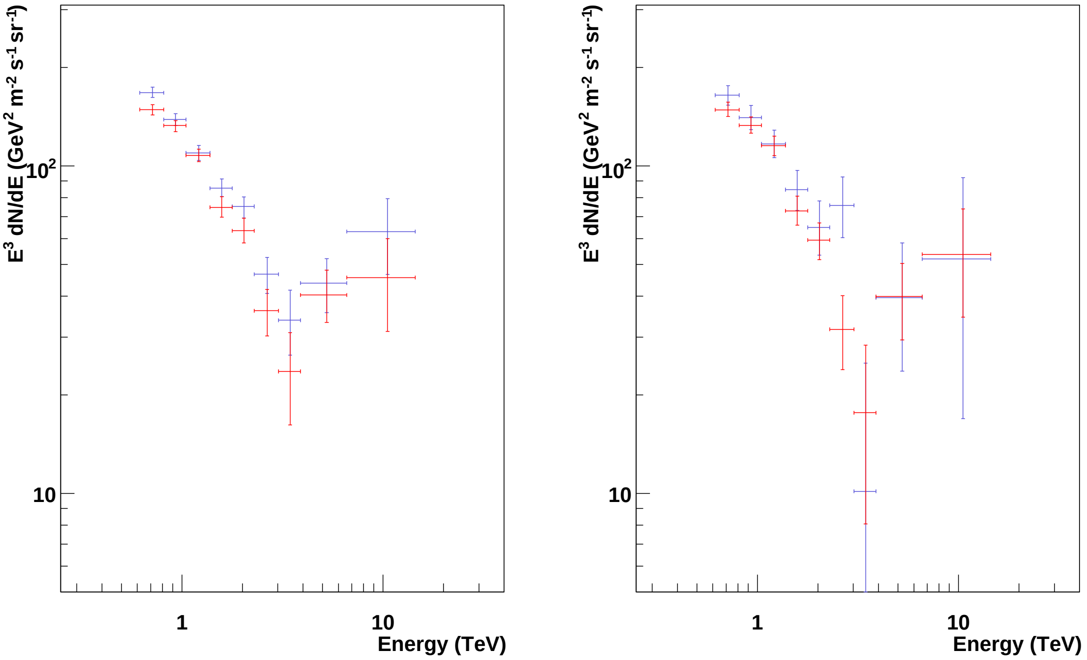

Figure 3.22: The electron spectrum. *Left*: Reconstructed with two different hadronic interaction models: SIBYLL (red) and QGSJET-II (blue). *Right*: Obtained from two different data sets: observations of the period between April 2004 to April 2005 (blue) and between April 2006 to April 2007 (red) obtained with the SIBYLL interaction model.

higher energies, the spectrum hardens considerably.
The measured spectrum can be fitted by a broken powerlaw (Fit A in Fig. 3.23):

$$dF/dE = k \cdot (E/E_{\mathrm{b}})^{-\Gamma_1} \cdot (1 + (E/E_{\mathrm{b}})^{1/\alpha})^{-(\Gamma_2 - \Gamma_1)\cdot\alpha} \tag{3.12}$$

with a normalisation $k = (3.7 \pm 0.6) \times 10^{-5}$ TeV^{-1} m^{-2} sr^{-1} s^{-1}, a break energy $E_{\mathrm{b}} = 3.4 \pm 0.4$ TeV, where the transition between the two spectral indices $\Gamma_1 = 3.9 \pm 0.05$ and $\Gamma_2 = 2.8 \pm 0.3$ occurs. The variable α denotes the sharpness of this transition. The goodness-of-fit is $\chi^2/\nu = 18.3/4$ (p=0.001). While this fit does not perfectly describe the data, it provides a first and easy approximation.
The statistical errors of the H.E.S.S. spectrum are much smaller than those of direct measurements. However, the systematic effects dominate over statistical errors. Therefore, detailed systematic studies have been performed to test this result and determine the systematic uncertainties of the measurement.

Systematic uncertainties

This sub-section summarises the main systematic uncertainties and describes the determination of the systematic error on the measurement resulting in the band of systematic

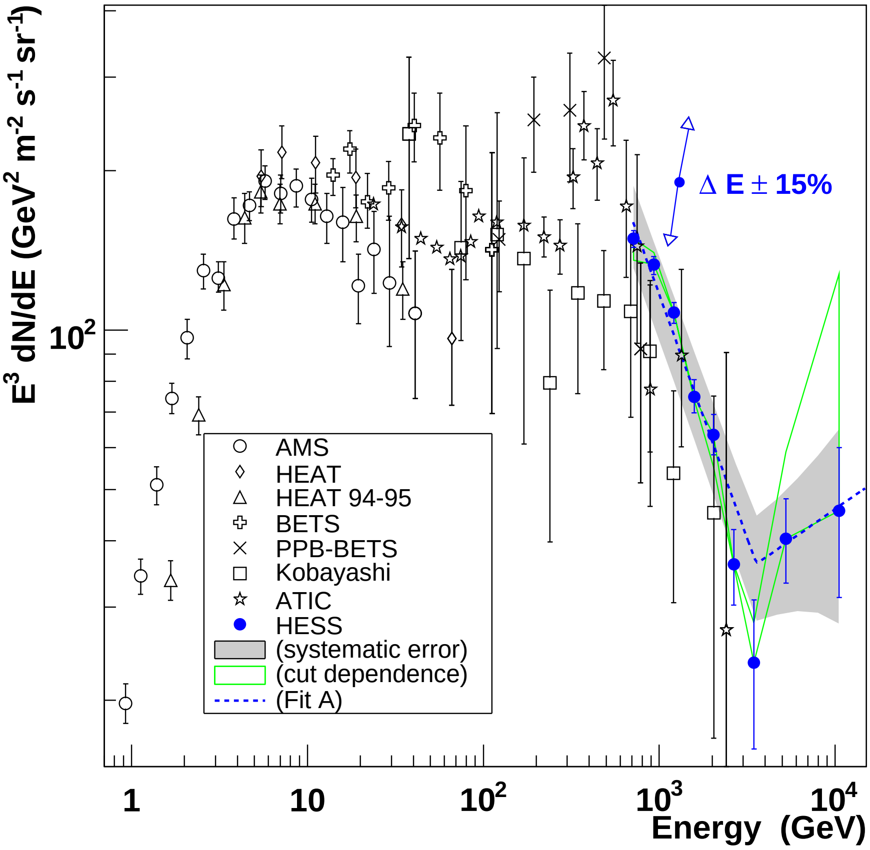

Figure 3.23: The energy spectrum E^3 dF/dE of cosmic-ray electrons as measured by H.E.S.S. in comparison with previous measurements. The H.E.S.S. data are shown as solid points. Fit A is a broken powerlaw fit. The fit is described in the main text. The shaded band indicates the approximate systematic error arising from uncertainties in the modelling of hadronic interactions and in the atmospheric model described later. The green bordered band visualises the cut dependence. The double arrow indicates the effect of an energy scale shift of 15%, the approximate systematic uncertainty on the H.E.S.S. points. Previous data are reproduced from: AMS (Aguilar et al. (2002)), HEAT (Barwick et al. (1998)), HEAT 94-95 (DuVernois et al. (2001)), BETS (Torii et al. (2001)), PPB-BETS (Torii et al. (2008)), Kobayashi (Kobayashi et al. (2004)) and ATIC (Chang et al. (2008)).

uncertainty shown in Fig. 3.23 and a systematic error on the spectral index. More detailed systematic studies and cross-checks are presented in Section 3.7. The main source of systematic errors are the use of proton simulations and the atmospheric model, which assumes constant atmospheric conditions in all observation runs. In the following, the systematic error on this measurement is determined by evaluation of the differences between the spectra shown in Fig. 3.22.

The dependence on the hadronic interaction model of the proton simulations is evaluated by a comparison of the spectra obtained with the SIBYLL and the QGSJET-II interaction

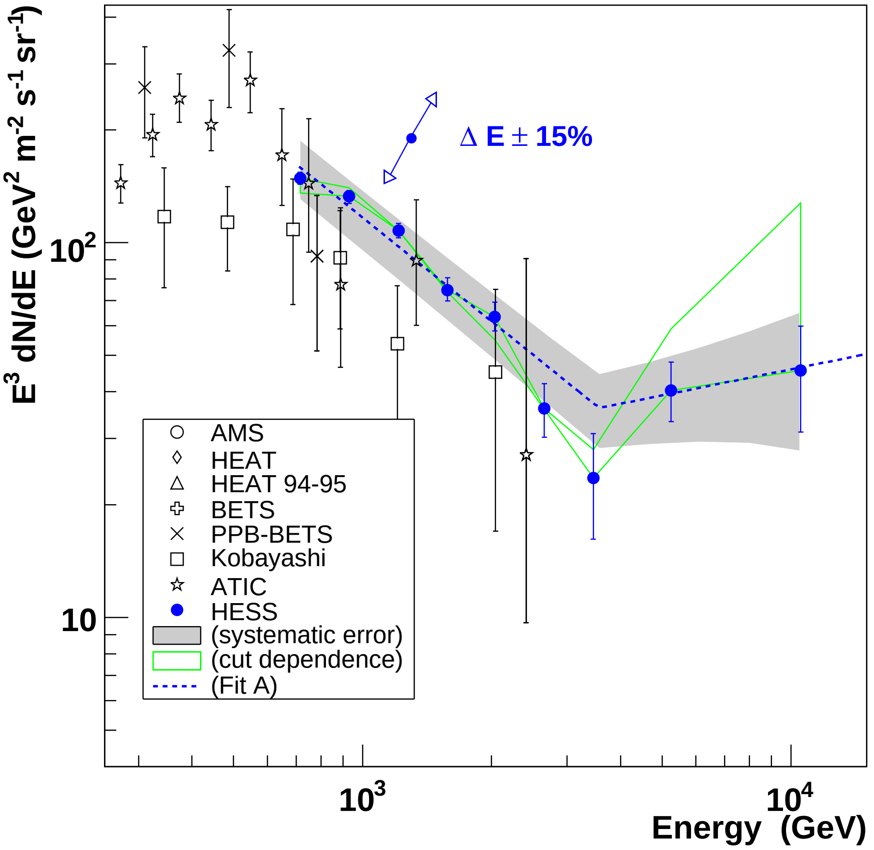

Figure 3.24: Zoom in the high-energy region of Fig. 3.23.

model. In order to estimate the effect of uncertainties in the atmospheric modelling, the data set is split and different years of observations are compared. Since these two effects are independent, they are added in quadrature to obtain the total systematic error.
For each energy band the ratio of the two compared fluxes of Fig. 3.22 is determined and then the logarithm of this ratio is fitted by a first order polynomial (see Fig. 3.25). These fits are then used to evaluate the size of the systematic uncertainty at a particular energy. As the two data sets of different years are both contained in the data set of the final spectrum and therefore their spectrum is averaged, their deviations contribute with a factor of 1/2. On the contrary, the deviation of the hadronic models fully contribute, because only one hadronic model (the SIBYLL interaction model) is used for the final spectrum determination.
The systematic error is indicated by the grey shaded band in Fig. 3.23 and 3.24, which is centered around the broken powerlaw fit (Fit A).

At higher energies, beyond the break in the spectrum, another effect has to be considered. The flux becomes dependent on the event selection cuts. This is demonstrated in a comparison of spectra obtained with different cuts in Fig. 3.26. The dependence on the event selection cuts is investigated by a comparison of the spectrum obtained with the

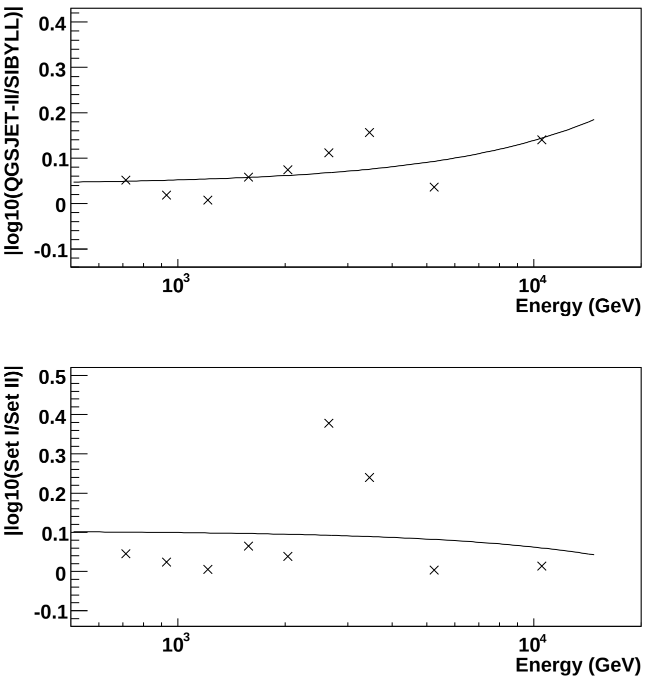

Figure 3.25: Determination of systematic error band: fits in the ratios of spectra obtained with different interaction models and from different data sets. *Top*: the logarithm of the ratio of flux points generated with SIBYLL and QGSJET-II hadronic interaction model. *Bottom*: the logarithm of the ratio of flux points of two data sets taken between April 2004 and April 2005 (Set I) and between April 2006 and April 2007 (Set II).

Cuts A to the one obtained with only the ζ cut. While at low energies the effect of event selection is irrelevant, at energies of more than 4 TeV, the flux becomes dependent on the chosen cut and this effect dominates the uncertainty of the high-energy part of the spectrum. However, the detection of an electron excess is present for any chosen cut up to energies of 10 TeV, where the statistics become too low for conclusive results. The effect of this cut dependence is demonstrated by the green bordered band in Fig. 3.23 and 3.24. Finally, the uncertainty on the H.E.S.S. energy scale amounts to 15% and is indicated by the blue arrow in Fig. 3.23 and 3.24.

To investigate the influence of the proton simulations further, the fraction of electron-like events in the proton ζ distributions is artificially increased. An increase in the electron-like component of the protons should affect the electron spectrum directly and is therefore an important measure of the stability of the spectrum determination facing the uncertainty of the hadronic interaction model.

For this purpose the ζ distribution of protons is first fitted in the $\zeta > 0.6$ region with a flat profile plus an electron component. The flat component is assumed to represent the ideal proton background, whose distribution is peaked at 0 and has a long tail towards

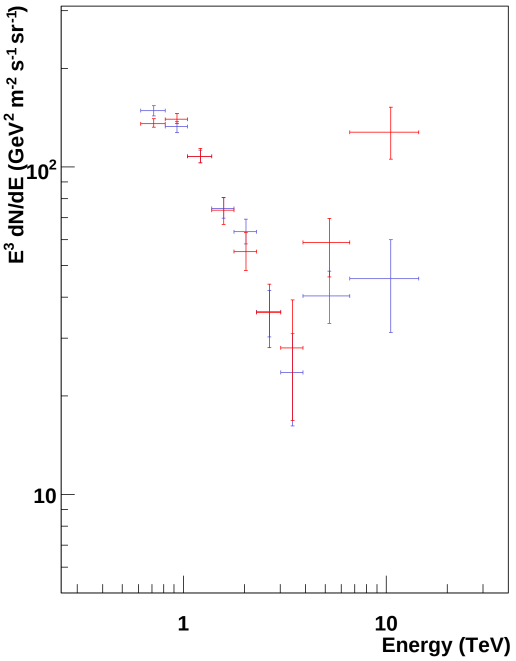

Figure 3.26: The electron spectrum with different event selection cuts: with Cuts A in blue and with the ζ cut only in red.

$\zeta = 1$. The electron-like component presumably reflects events where a large fraction of proton energy is transformed to a single π^0. This electron component is somewhat more pronounced for SIBYLL as compared to QGSJET-II, giving rise to the model dependence. The energy dependent ratio of the electron component in the background and the flat component is fitted (Fig. A.11 in the Appendix) and the fit is used to artificially alter the electron-like component of the proton simulations. The modified proton distribution in ζ is then used to fit the data. A comparison of spectra obtained with different electron components in the background is shown in Fig. A.12 in the Appendix. If the ratio of the electron component to the flat component is doubled, i.e. the cross-section of the π^0 events is assumed to be 100% larger than implemented in the respective interaction model, while the energy dependence of the cross-section is unchanged, this reduces the electron flux by $\approx$30% for the case of the SIBYLL interaction model without a significant change in spectral shape. The systematic error on the spectral index is $\Delta\Gamma(\text{syst.}) \lesssim 0.3$.

A combined fit

In order to parametrise the H.E.S.S. data together with direct measurements, the combined data of the lower energy part of the H.E.S.S. spectrum and the direct measurements are fitted. Since ATIC data with their bump in the spectrum show a rather peculiar feature they are not included in the fit. Since the H.E.S.S. data are dominated by systematic errors, the errors used for the fitting are the systematic errors rather than the statistical ones. The H.E.S.S. fluxes are relatively high, and therefore, the energy scale between 0 and 15% is included in the fit as a free parameter. A powerlaw fit with exponential cutoff

$$dF/dE = k \cdot E^{-\Gamma} \cdot \exp(-E/E_c) \tag{3.13}$$

can describe the data with a normalisation $k = (1.2 \pm 0.1) \times 10^{-5}\ \mathrm{TeV}^{-1}\,\mathrm{m}^{-2}\,\mathrm{sr}^{-1}\,\mathrm{s}^{-1}$, a spectral index of $\Gamma = 3.08 \pm 0.03$, and a cutoff energy $E_\mathrm{c} = 2.5 \pm 0.5$ TeV with a shift in energy of -11%[14]. This fit is shown in Fig. 3.27 (Fit B).

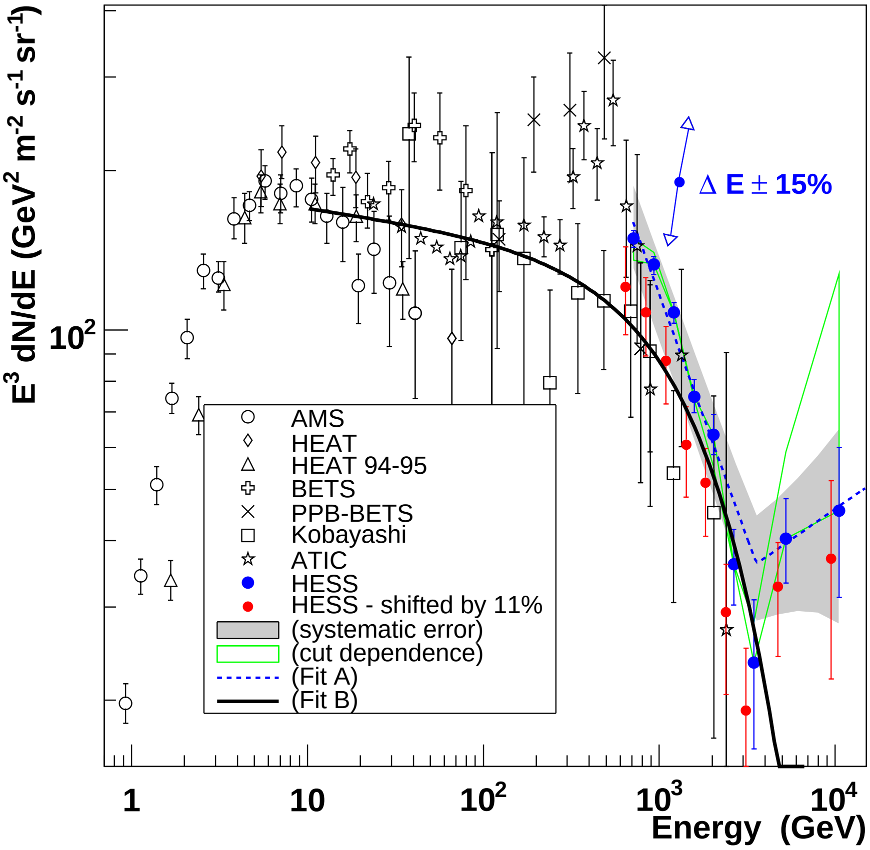

Figure 3.27: Combined fit to the H.E.S.S. spectrum and direct measurements (Fit B). Red points show the H.E.S.S. data shifted by 11% in energy with error bars representing the systematic errors.

3.6.1 Extension to Lower Energies

The recent ATIC detection of a "bump" in the cosmic-ray electron spectrum between 300 and 800 GeV (Chang et al. (2008)) and its possible interpretations as signature of dark matter has stirred considerable interest. It is therefore desirable to extend the H.E.S.S. electron spectrum to lower energies. This is not possible with the Cuts A, because they

---

[14] Numbers differ from those published in Aharonian et al. (2008a) because here ATIC data are excluded while the paper fit contains ATIC data of Chang et al. (2005).

are optimised for high energies and the large size cut increases the energy threshold significantly. Therefore, a second set of cuts (Cuts B) are chosen to reach lower energies. The influence of this modification in event selection on the energy threshold was already shown in Fig. 3.1.
Another problem for reaching lower energies is the degradation of the mirrors and the resulting reduction of the light yield in the camera, which increases the energy threshold. In order to avoid this, a smaller data sample is used that was taken between spring 2004 and summer 2005. The muon correction factor for this data set is shown in Fig. 3.28. Compared to the correction factor for the whole data set shown in Fig. 3.20, large correction factors disappeared, thus decreasing the energy threshold of the data set.
The spectrum obtained from this data set with Cuts B applied is displayed in Fig. 3.29. The ζ distributions of the fit are shown in Fig. 3.30. The band of systematic uncertainty is determined in the same way as before, i.e. by comparing spectra obtained with the SIBYLL and QGSJET-II interaction models and two independent data sets (data taken in summer and autumn 2004).
While at higher energies the spectrum is consistent with the one determined previously, at lower energies a clear break is observed at ≈900 GeV. However, the H.E.S.S. data does not confirm the peak observed by the ATIC collaboration.

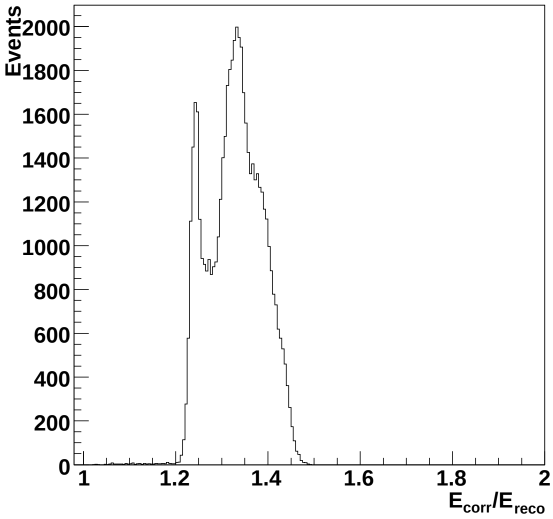

Figure 3.28: Distribution of muon correction for the data set optimised for low energies.

3.6.2 Verification

In the previous sub-sections the electron spectrum was derived, including an extension to lower energies. However, electron-initiated air showers are in practice extremely difficult to separate from γ-ray showers. It was already discussed in Chapter 1.4 that a γ-ray origin of the observed signal is unlikely because theoretical predictions of the diffuse extragalactic γ-ray flux are much lower than the cosmic-ray electron flux. Nonetheless, it is worthwhile to attempt an empirical investigation of the γ-ray fraction in the data set.

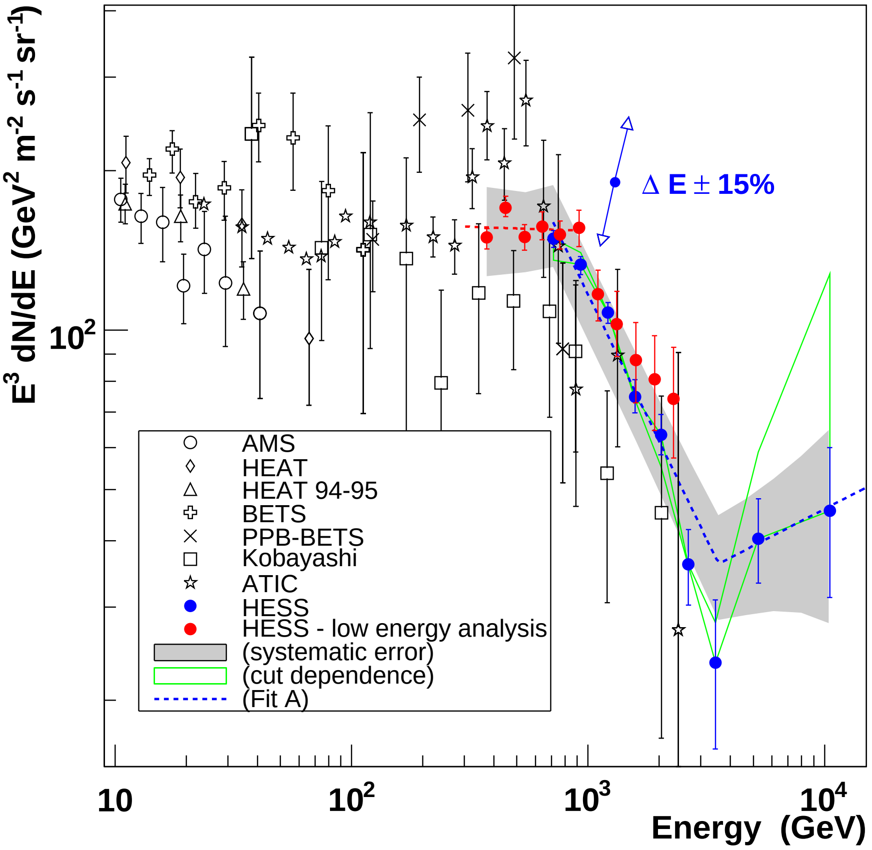

Figure 3.29: Electron spectrum with extension to lower energies. Red spectral points have smaller energy bands, and are generated from a reduced data set with the use of Cuts B.

Essentially the only useful separation parameter is the depth of shower maximum (X_{max}), which occurs on average ≈20 g cm^{-2} (or ∼ half a radiation length) higher in the atmosphere for electrons[15]. Therefore, the X_{max} distribution of an enhanced electron data sample with $\zeta > 0.9$ is compared with simulations. The simulations are a combination of protons and electrons and a combination of protons and γ rays with the relative contributions obtained from the fit in ζ in this energy range and corrected for the harder cut of $\zeta > 0.9$. The energy dependence of X_{max} is corrected for by the empirically determined elongation rate of 93 g cm^{-2}/decade that is expected for electron primaries.

For the low-energy part of the spectrum, this is shown in Fig. 3.31. The left hand side shows the X_{max} distribution of the data together with the models of simulations. Also the shift between the pure electron and γ-ray distributions is shown. A fit of the X_{max} distribution with the electron/γ-ray fraction as a free parameter results in a maximum 10% contribution of γ rays to the signal (for a confidence level of 90%). However, taking into account a conservative systematic uncertainty in the determination of X_{max} of 5 g cm^{-2} due to atmospheric uncertainties, a significant contamination of ≈50% of this electron

---

[15] See Chapter 2.1.

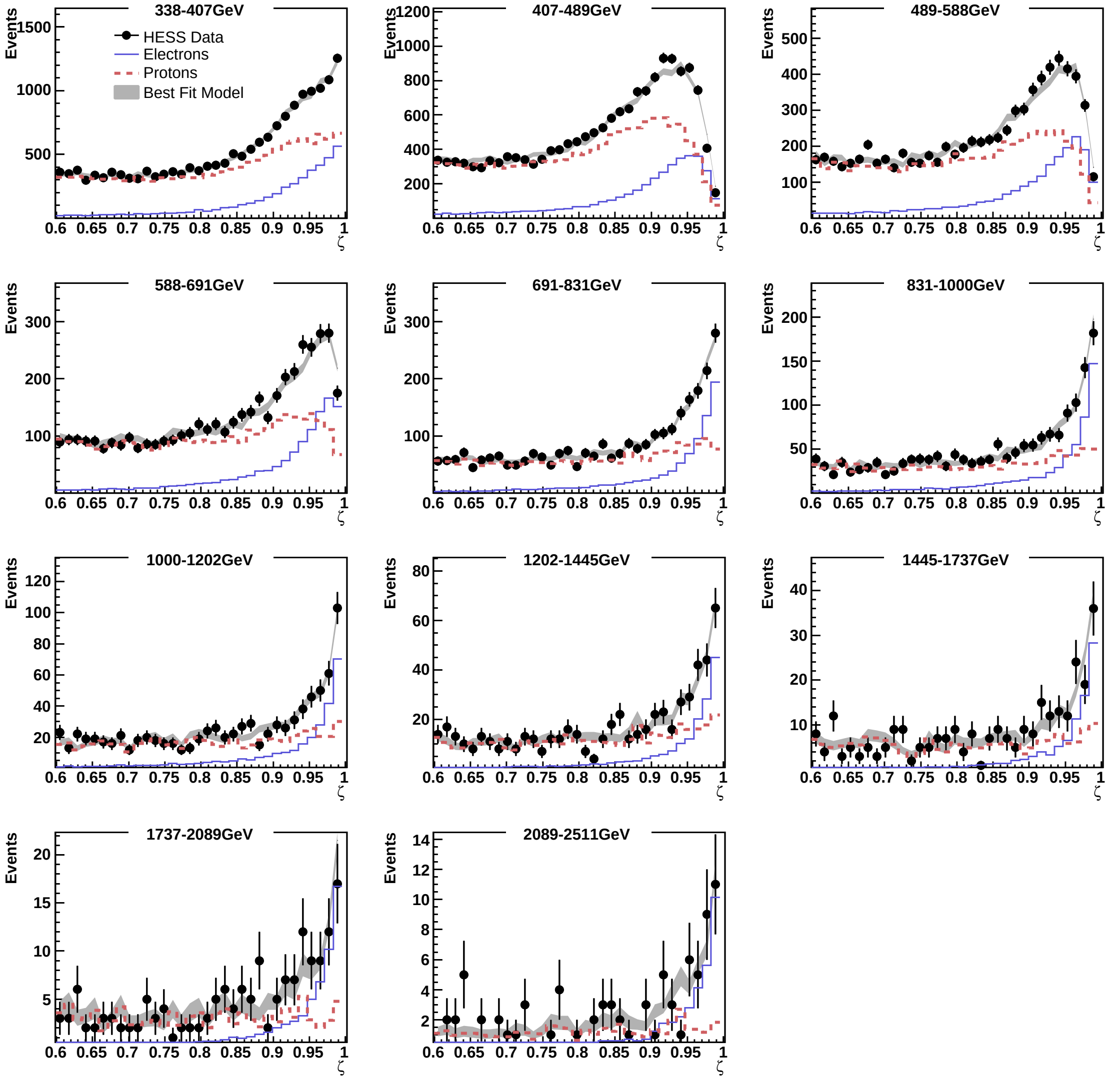

Figure 3.30: Low-energy spectrum: fit in the ζ distribution in the energy bands that are used for the spectrum. H.E.S.S. data are shown in black points, and the best fit model as shaded band. The contributions to the model by electrons are shown in blue, and the proton contribution in form of the red dashed line. Cuts B have been applied.

measurement by the diffuse extragalactic γ-ray background cannot be excluded. Systematic uncertainties in the hadronic modelling are not considered.
The right hand side of Fig. 3.31 shows a comparison with data only: a γ-ray rich data set from regions within 0.15° radius of γ-ray sources is compared to the data set used for the analysis. A displacement of the maximum of the two distributions is visible, which can be an indication of an electron nature of the signal or simply an artefact due to different atmospheric conditions existent in the two data sets.
In Fig. 3.32 the $X_{\max}$ distribution is shown for the high-energy part of the spectrum between

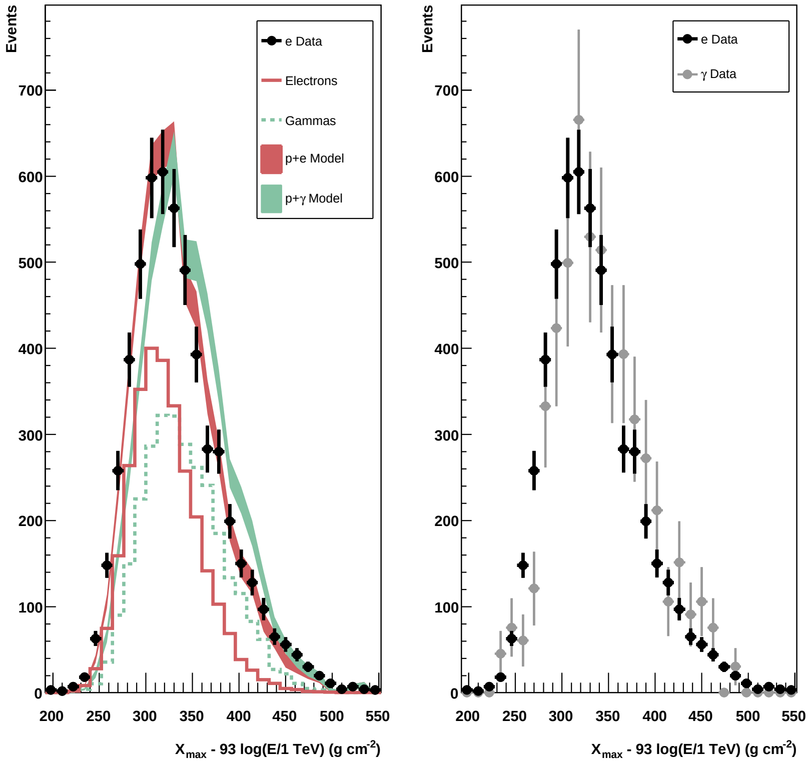

Figure 3.31: *Left*: The distribution of reconstructed shower maximum (X_{max}) for H.E.S.S. data compared to simulations. For each shower the measured X_{max} is corrected for the energy dependent shower elongation. Showers with reconstructed energies between 1 and 4 TeV are included. The bands show the combination of electrons and protons (simulated using SIBYLL) and of γ rays and protons, with a ratio determined by a fit to the ζ distribution of the data in this energy range. The distributions of electrons and γ rays are shown for comparison. *Right*: A comparison of this data (black) with a γ-ray rich data set taken from regions $< 0.15°$ from γ-ray sources (grey).

3 and 14 TeV. It can be seen that the data are described better by the model constructed with electrons than by the γ-ray model, and also a displacement between the electron data and a γ-ray rich data set is visible. However, since at these energies there are less events and large statistical errors, the situation is even less conclusive than for the case of the low-energy spectrum.

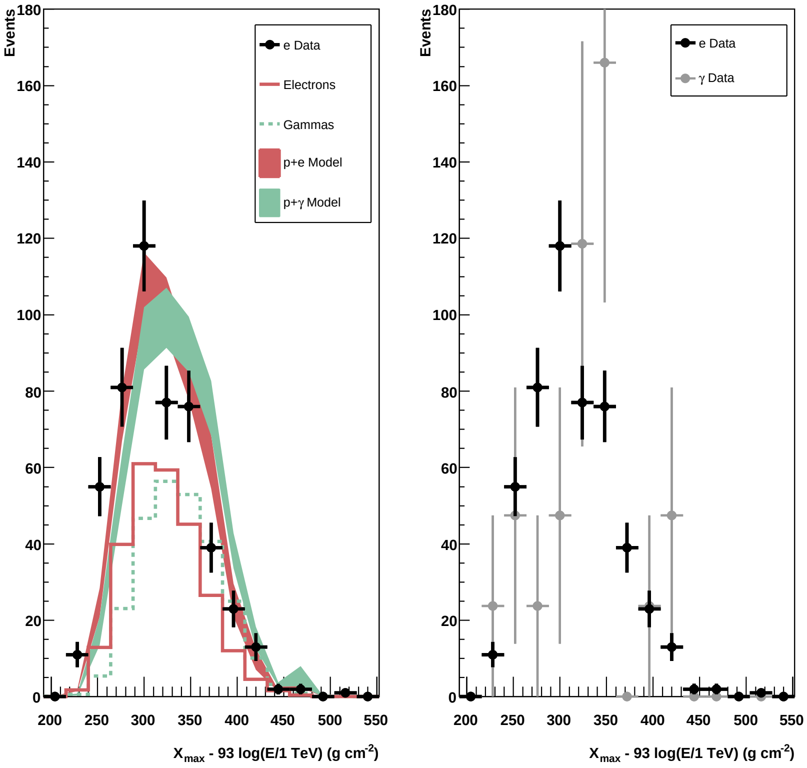

Figure 3.32: *Left*: The reconstructed depth of the shower maximum $X_{\max}$ of the H.E.S.S. data after a ζ cut of 0.9 in the energy range of 3–14 TeV together with two models: a combination of protons (simulated using SIBYLL) and electrons and a combination of protons and γ rays. Also the distributions of electron and γ-ray simulations are shown. *Right*: Comparison between data (black) and a γ-ray rich data set (grey) containing only events within 0.15° of a γ-ray source. $X_{\max}$ is corrected for the energy dependent elongation rate of 93 $\mathrm{g\,cm^{-2}}$.

3.7 Systematic Tests

Because of the intrinsic difficulty of the measurement mentioned before, multiple tests are required to cross-check the applied method and the results. Selected tests are presented in this section.

3.7.1 Testing the Method

The analysis method has been tested by varying single parts of the analysis, for instance the classifier, the fitting algorithm, or the method of the effective area determination. The complete analysis is cross-checked by an application to γ-ray sources with well determined spectra and cosmic-ray protons.

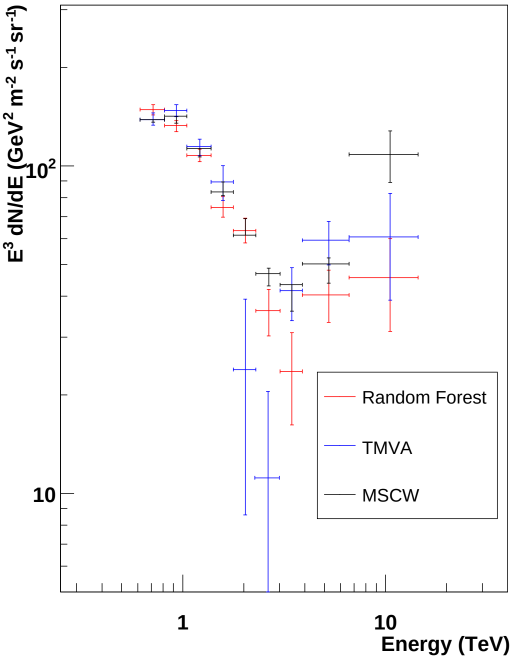

Figure 3.33: Comparison of different classifiers: the Random Forest output parameter ζ is compared to a TMVA classifier and the mean scaled width (MSCW).

The Classification Method

As the Random Forest is used for the first time for a H.E.S.S. data analysis, it is desirable to do a cross-check with different methods. For this purpose, the fitting algorithm presented in Section 3.3 was used to fit distributions of two other classifiers: the output parameter of the neural network MLP contained in the Toolkit for Multivariate Analysis (TMVA) package[16] (Hocker et al. (2007)), and the standard parameter of γ-hadron separation in the H.E.S.S. analysis, the mean scaled width[17].

Since the MSCW does not have the strong background suppression of multivariate analysis techniques like Random Forest and the TMVA neural network, an additional hard cut on the mean scaled length (MSCL) was applied (MSCL<0.6). The comparison of the three spectra can be seen in Fig. 3.33.

The fit in the single energy bands in the distributions of the TMVA classifier and the MSCW is displayed in Fig. 3.34 and Fig. 3.35, respectively. Looking at the TMVA classifier, the main problem is the similarity of the electron and proton distributions. In addition, both, the TMVA classifier and MSCW, have the problem of a high level of background as they have not been optimised for this analysis nor any systematic studies have been performed. Especially in the MSCW distributions, the combined model of electrons and protons does not always describe the data. This can be due to the effect of heavier nuclei

---

[16] http://tmva.sourceforge.net/

[17] MSCW, for the definition see Eqn. (2.3).

in the background, which are not as efficiently suppressed as by the Random Forest. However, despite their obvious shortcomings, the spectra obtained with both classifiers agree fairly well with the electron spectrum derived previously in this chapter.

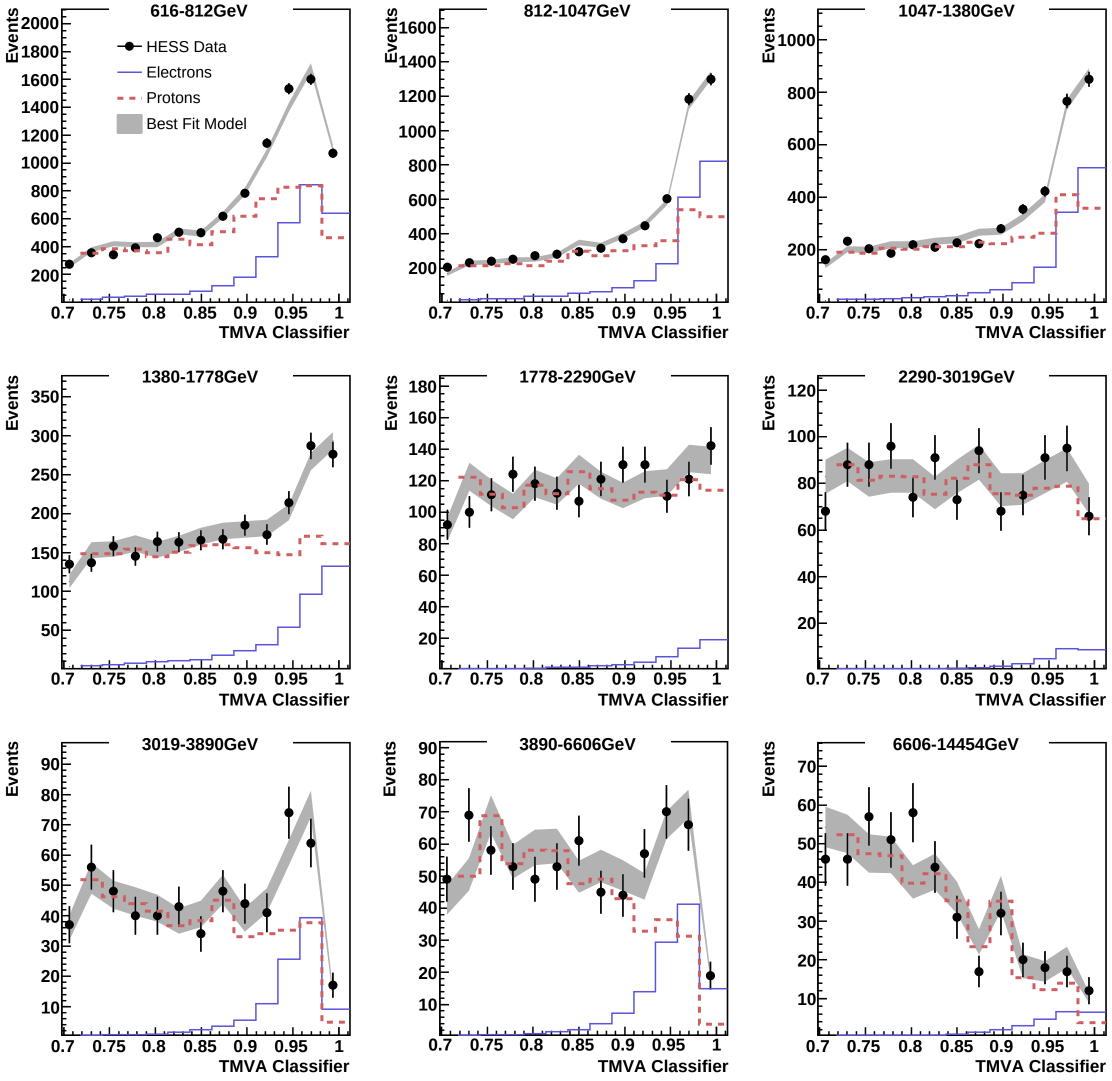

Figure 3.34: Fit in the TMVA classifier in the energy bands.

The Fitting

The fitting procedure was tested by a comparison with a χ^2 fit. The spectra obtained with the χ^2 fit and the likelihood fit are shown in Fig. 3.36. Both methods yield an excellent agreement.

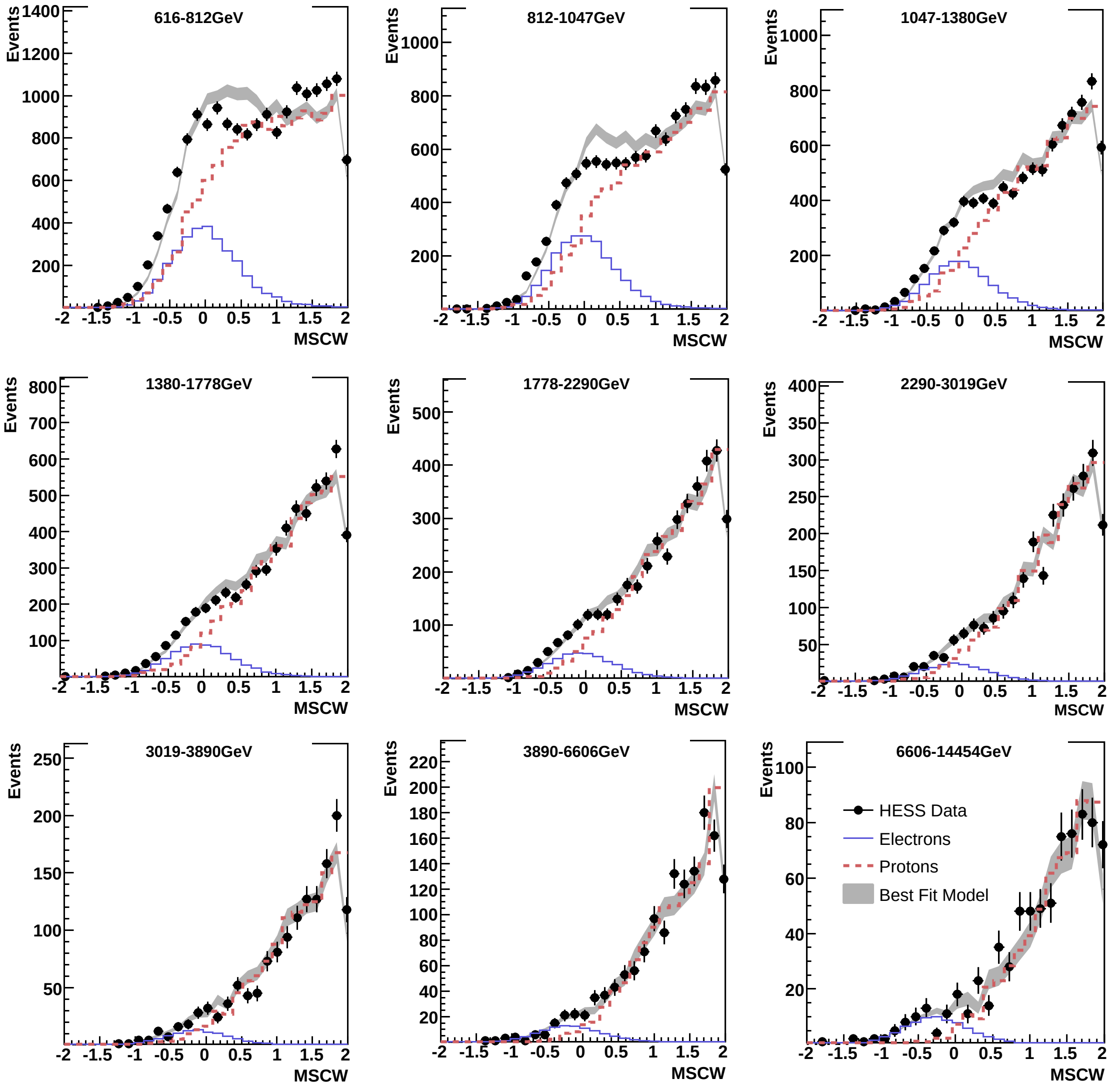

Figure 3.35: Fit in MSCW in the energy bands. A cut of $MSCL < 0.6$ is applied. A mismatch of the best fit model and data is observed, especially in the three lowest energy bands, which is possibly due to a component of heavier nuclei that is not as efficiently suppressed as in the Random Forest analysis.

Effective Areas

In order to investigate the effect of the change in offset due to the excluded source position, which is neglected in the analysis, a method is implemented that determines effective areas (as well as ζ distributions) in offset bands and then interpolates between these bands[18]. The field of view is divided into small bins. For each bin, the offset interpolation is carried out separately and the resulting effective areas are summed weighted by the bin's solid angle. While this increases the computing time significantly, it provides a more accurate

---

[18] This method will also be used for the diffuse γ-ray analysis in Appendix B.

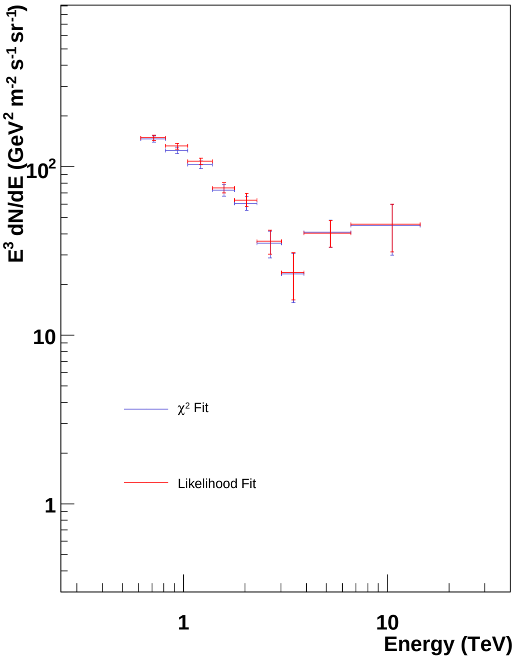

Figure 3.36: Comparison of a χ^2 fit (blue) and the likelihood fit (red).

analysis. At the same time, the method wastes data, because the circular shape of the used field of view and the exclusion regions is approximated by squares and only squares that do not extend into the exclusion region and that are fully contained in the central 3° of the camera are used for the analysis.
The comparison of the two methods can be seen in Fig. 3.37. A good agreement is obtained between the methods, justifying the simpler approach used throughout this work.

Cross-Checks I: Tests on γ-ray Sources

For a cross-check of the complete analysis chain, two known H.E.S.S. sources are analysed and the spectra compared with the ones of the H.E.S.S. standard analysis. The two sources are HESS J1745-290 and RX J1713-3946. HESS J1745-290 is positioned in the Galactic centre and coincident with Sgr A*. For the H.E.S.S. angular resolution it is a point source. RX J1713-3946 is a shell-type SNR and has an extension of 0.6°.
These sources were analysed in two ways: First, the regular electron analysis was applied to the data sets of the sources, including electron ζ distributions and electron effective areas for a uniform offset distribution between 0° and 1.5°. With this method, an approximate agreement of the spectra with the standard H.E.S.S. source analysis was obtained.
Secondly, for further improvement, the electron ζ distributions and effective areas were replaced by ζ distributions and effective areas obtained by γ-ray simulations for a fixed offset of 0.5°. The fits in the ζ distributions are shown in the Appendix in Fig. A.13 and A.14. A very good agreement of this analysis with the H.E.S.S. standard analysis can be

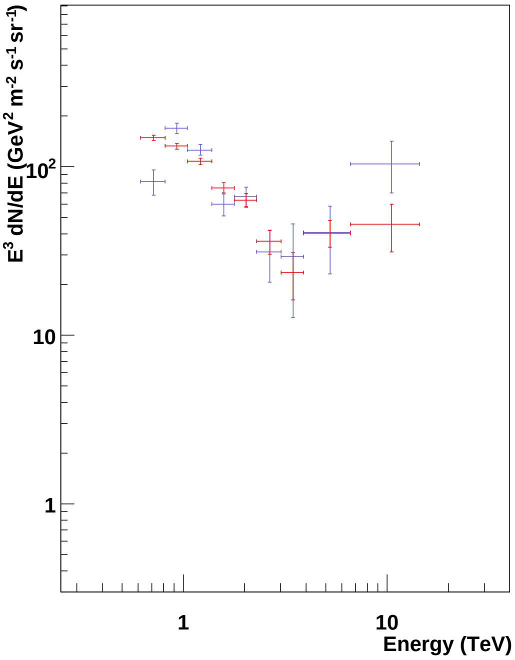

Figure 3.37: Spectra obtained by two different methods for effective area determination: the standard effective areas (red) and an interpolation between offset bands (blue). The much larger statistical errors of the blue spectrum are caused by the method.

seen in Fig. 3.38.
The difference between a spectrum obtained with the standard analysis and one obtained with an electron-type analysis is the cosmic-ray electron component, which is subtracted in the standard analysis but contained in the spectrum of an electron-like analysis (since the background is modelled by proton simulations only). For the case of Sgr A*, this component is of the order of a few percent of the total flux and thus completely negligible. For RX J1713-3946, however, due to its large extension, the electron contribution amounts to $\sim 20\%$ at 1 TeV, which should be visible in the spectrum in form of a significantly higher normalisation and a slightly steeper slope to account for the steeper electron spectrum. While the slightly steeper slope can be found in the spectrum, the normalisation is rather lower than the standard analysis. This can be explained by the simplification that effective areas are used for an offset of $0.5°$, while, due to the source extension, the data covers an offset range of $0° - 1.2°$ (the source being positioned at $0.5°$ offset). Since the camera acceptance in dependence of the offset is essentially flat at values $< 0.5°$ and then decreases, effective areas of the electron-type analysis are overestimated, leading to smaller fluxes compared to the standard analysis that handles the source extension appropriately.

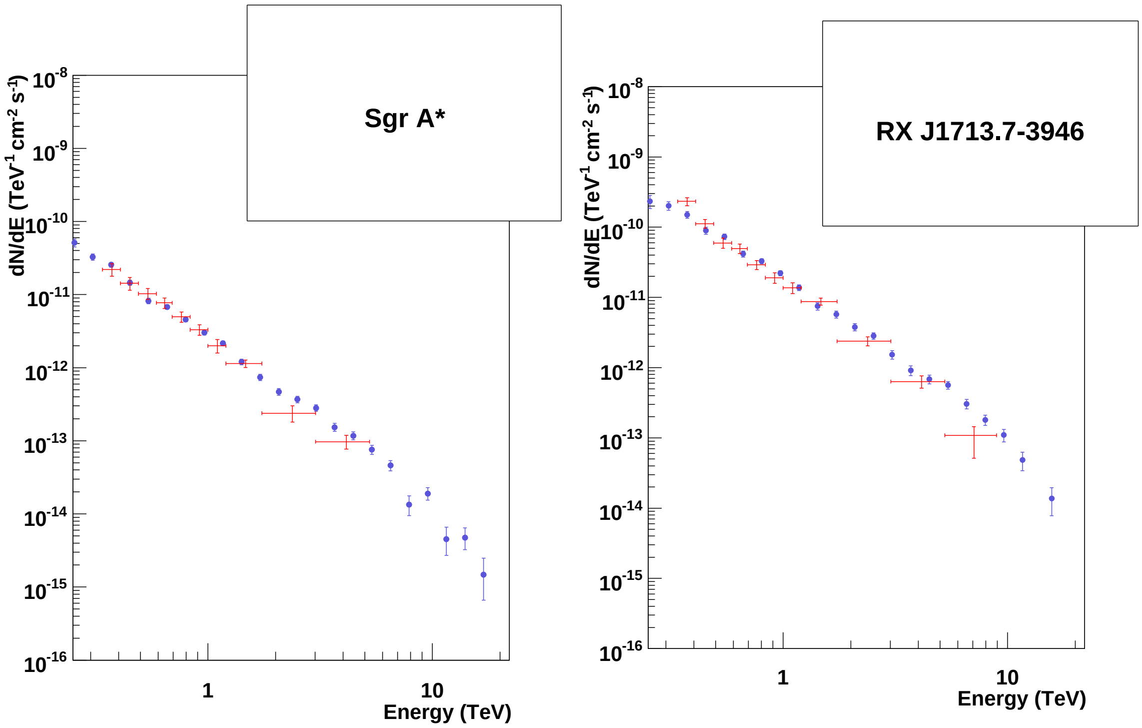

Figure 3.38: Systematic test: Spectra of Sgr A* and RX J1713-3946. Blue i the H.E.S.S. standard analysis, red are the spectral points of an electron-type analysis with ζ distributions and effective areas obtained from γ-ray simulations for a point source at an offset of 0.5°.

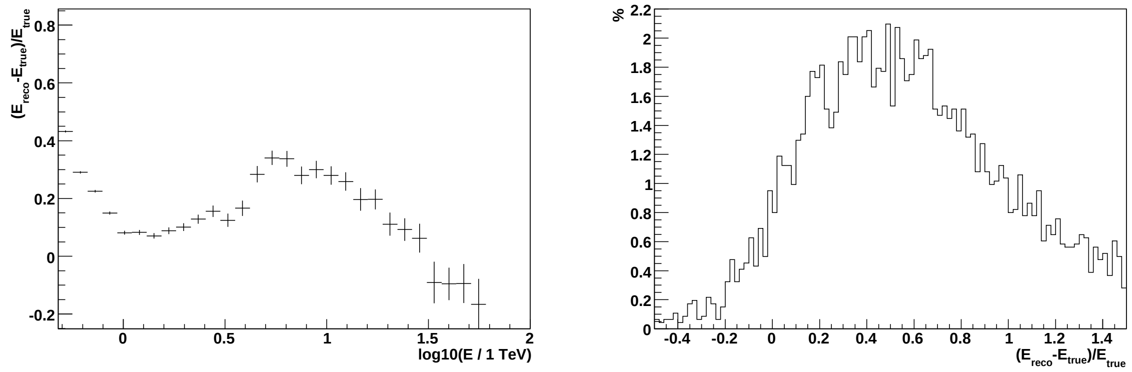

Figure 3.39: The energy reconstruction with proton energy lookups for the SIBYLL interaction model. *Left*: The energy bias. In the range of 1–50 TeV used for the spectrum determination, the bias is not larger than 40% (the number reduces to 20% if QGSJET-II simulations are considered). *Right*: The energy resolution. The root mean square of the distribution is 40%.

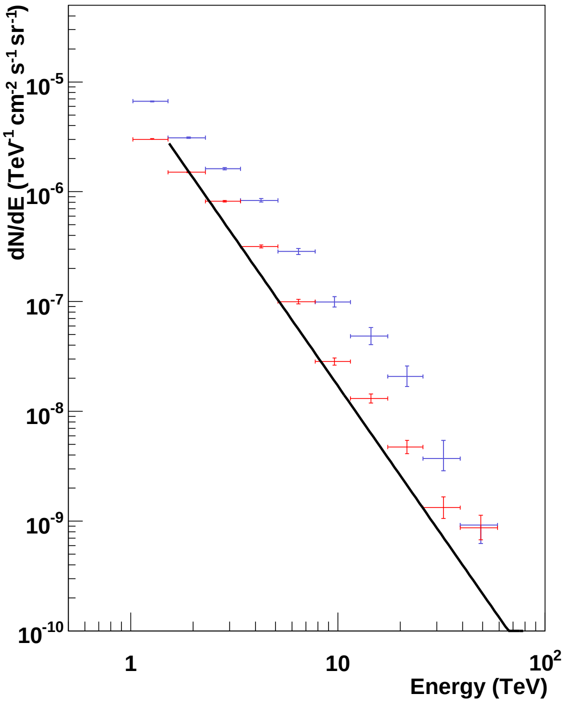

Figure 3.40: Proton spectrum obtained with ζ distributions and effective areas of protons using SIBYLL (red) and QGSJET-II (blue).

Cross-Checks II: a Proton Spectrum

Since in the electron analysis a two parameter fit is applied with the electron and proton fractions as degrees of freedom, the derivation of a cosmic-ray proton spectrum is a further systematic check of the method. For this purpose, the proton fraction s, which was not used further for the electron analysis, is used to determine the number of cosmic-ray protons in the data set. For a result to be meaningful, energy lookups have to be produced for an energy reconstruction specific to protons, and the effective areas have to be produced by proton simulations reflecting the detection probability and cut efficiency of protons rather than electrons. For the generation of the energy lookup, the QGSJET-II simulations are used because they were generated up to an energy of 100 TeV (as opposed to 60 TeV for the SIBYLL interaction model). As the predefined fitting range of $\zeta > 0.6$ is used, lookups are generated for events passing this cut. The energy reconstruction of these lookups for the SIBYLL interaction model is shown in Fig. 3.39. The energy reconstruction works not as well as for the case of electrons, and in the range relevant for the spectrum (1–50 TeV), the energy bias lies between 5% and 40%. For the case of the QGSJET-II model, the maximum bias reduces to 20%.

Data, electron and proton simulations are reconstructed by the use of these lookups and fitted in independent energy bands. The spectrum obtained by coupling the proton effective areas with the most likely number of proton events in the data are shown in Fig. 3.40.

Compared are spectra obtained with SIBYLL and QGSJET-II ζ distributions and effective areas (the effective areas for the SIBYLL interaction model are shown in Fig. 3.41) together with a parametrisation of the proton spectrum obtained from Hörandel (2005).
The deviations between the different interaction models are extremely large (about a factor of 3). This can be understood if considering that only the extremely small fraction of electron-like events is determined and from this small part ($\sim 1\%$ of the proton events) of rather special events, the number of all events is deduced via the proton simulations (i.e. the proton effective areas). Even though the spectrum of the SIBYLL interaction model is already about a factor 2 higher in flux than the reference spectrum, this is, considering the method and the poor energy reconstruction, a good agreement achieved by this method.

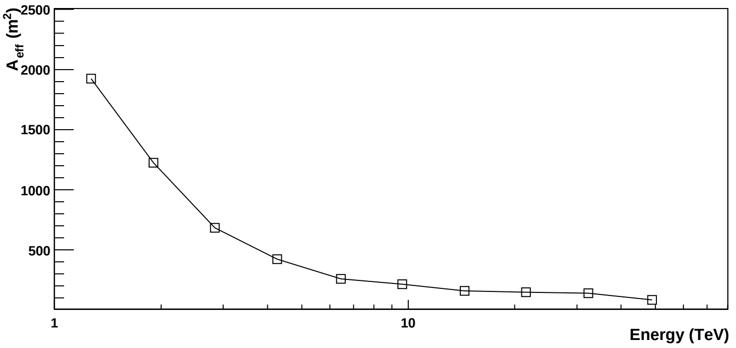

Figure 3.41: Effective areas for a proton spectrum obtained by the SIBYLL interaction model. Due to the $\zeta > 0.6$ cut, the effective areas are reduced by a factor of 10^{-2} to ~ 200 m^2 beyond 10 TeV (compared to $\sim 6 \times 10^4$ m^2 for electron effective areas).

3.7.2 Tests on the Data Set

Further systematic studies on the shape of the spectrum have been performed: a list of tests and their results is given in Table 3.6. The deviations given in Table 3.6 are determined by a comparison of the spectra of two independent data sets. The difference between the flux points of the two spectra is scaled by the reference spectrum of Fig. 3.23. The errors are calculated from the statistical errors of each flux point. As sub-sets of the data set are used, with some of them being quite small, the statistical errors are much larger than the ones from the reference spectrum.
The effect of the season of the observation time is investigated by a comparison of spectra obtained from data taken in summer and in winter. The zenith angle dependence is studied by a comparison of two distinct data sets at zenith angles of $0° - 18°$ and $18° - 28°$. In order to test the influence of the Galactic plane, the data set was split in two, separated according to low ($< 40°$) and high ($> 40°$) Galactic latitude values. Different spatial positions are investigated by the use of three data sets with observations targeting the AGN H 2356-309, PKS 2155-304, and 1ES 1101-232 (obviously, the sources do not contribute to the data set). For the comparison in Table 3.6 the data sets of H 2356-309 and PKS 2155-304 are chosen, which showed the largest deviations and the best statistics. To test the hypothesis

of a γ-ray halo origin of the high-energy part of the spectrum[19] also the influence of the distance to the target position is investigated and data sets with detected/not detected targets compared. Finally, observations targeting AGN are compared to different types of sources.

Since these tests all use a comparison of distinct data sets taken at different times under different atmospheric conditions, their results are subject to the atmospheric uncertainty. Within the systematic uncertainty, all tests demonstrate a good agreement.

---

[19] See Section 3.8.

Energy (TeV) Test	0.62-0.81	0.81-1.0	1.0-1.4	1.4-1.8	1.8-2.3	2.3-3.0	3.0-3.9	3.9-6.6	6.6-14.5
Season	0.10 ± 0.10	0.04 ± 0.12	0.23 ± 0.14	0.18 ± 0.23	0.20 ± 0.26	0.52 ± 0.50	0.15 ± 0.75	0.15 ± 0.56	1.99 ± 1.41
Zenith	0.10 ± 0.07	0.10 ± 0.08	0.05 ± 0.10	0.09 ± 0.15	0.10 ± 0.18	0.23 ± 0.32	0.29 ± 0.63	0.03 ± 0.38	1.15 ± 0.71
Galactic latitude	0.08 ± 0.07	0.02 ± 0.07	0.13 ± 0.09	0.07 ± 0.14	0.13 ± 0.17	0.02 ± 0.32	0.14 ± 0.62	0.40 ± 0.38	0.33 ± 0.64
Position	0.09 ± 0.11	0.25 ± 0.12	0.33 ± 0.15	0.35 ± 0.22	0.68 ± 0.30	0.33 ± 0.53	1.23 ± 0.74	0.77 ± 0.63	0.34 ± 0.92
Distance to target	0.08 ± 0.15	0.11 ± 0.15	0.29 ± 0.16	0.12 ± 0.20	0.40 ± 0.27	0.29 ± 0.55	1.16 ± 1.18	0.36 ± 0.87	1.39 ± 1.53
Detected/not detected	0.24 ± 0.13	0.04 ± 0.15	0.11 ± 0.19	0.38 ± 0.26	0.17 ± 0.32	1.03 ± 0.66	1.70 ± 1.20	0.03 ± 0.63	1.09 ± 1.17
Source type	0.11 ± 0.16	0.46 ± 0.18	0.44 ± 0.22	0.10 ± 0.34	0.27 ± 0.37	0.42 ± 0.73	0.00 ± 0.32	0.79 ± 1.02	0.79 ± 0.94

Table 3.6: The maximum deviations obtained from various systematic tests involving different data sets, relative to the spectral points of Fig. 3.23, in the energy bands of the spectrum. The errors are statistical errors only. Details of the tests are described in the main text.

3.8 Interpretation

Because of the different behaviour of the low-energy and high-energy part of the spectrum in the systematic studies, the interpretation of the spectrum is split in a discussion of the low-energy spectrum up to 3.4 TeV and a high-energy part above that energy.

3.8.1 Low-Energy Spectrum

At energies below 3.4 TeV the spectrum is stable with very small statistical errors and systematic errors of the order of 20%. The H.E.S.S. spectrum shows some overlap with direct measurements and demonstrates a good agreement within the systematic uncertainties. Regarding the extension of the spectrum to lower energies, the H.E.S.S. data agrees well with the measurements of emulsion chambers (Kobayashi et al. (2004)), but contradicts the ATIC data (Chang et al. (2008)). While the H.E.S.S. spectrum has large uncertainties in the total flux normalisation due to the large systematic uncertainties and the H.E.S.S. energy scale uncertainty of 15%, the spectral shape is well measured. Furthermore, it is to be expected that the hadronic background is smooth and therefore, features as the ATIC bump should be observable with H.E.S.S. despite the use of hadronic interaction models for the background determination. The pending question of the authenticity of the ATIC peak might be solved by the cosmic-ray electron measurement of FERMI.

At TeV energies, sources of cosmic-ray electrons originate from nearby and recent sources. The measurement of 3 TeV electrons therefore allows conclusions to be drawn on the existence of local accelerators. This can be seen exemplarily in Fig. 3.42, where a calculation of the contribution of sources with distances larger 1 kpc and older than 10^5 years is added from Kobayashi et al. (2004). The H.E.S.S. data represent a significant excess in flux compared to these flux predictions. Therefore, the H.E.S.S. electron measurement proves the existence of a local cosmic-ray electron accelerator within 1 kpc distance.

3.8.2 High-Energy Spectrum

While the low-energy part of the electron spectrum measured by H.E.S.S. has proven consistent in various tests, the hardening of the spectrum above 4 TeV has to be considered as uncertain. The analysis gave large deviations depending on the chosen event selection cut. However, the signal of electromagnetic showers is persistent throughout the tests. Shown in the spectrum of Fig. 3.29 are the flux points corresponding to the hardest cuts. Since the cuts improve the quality of the data set, these flux points are assumed to be the most reliable. The most influential cut at these energies is the distance of the shower's impact point from the array. Far away showers are usually not as well reconstructed. Even harder cuts, which could demonstrate a convergence, cannot be applied due to a lack of statistics at these energies. In the following, several possible explanations of the apparent excess above 4 TeV are discussed.

Fake Signal due to Incorrect Background Subtraction

A critical point of the analysis is the modelling of the rate of cosmic-ray induced showers which mimic electron showers, most likely because early in the development of the shower a large fraction of energy is transferred to electromagnetic sub-showers or even a single π^0. The rate of cosmic-ray showers mimicking electrons is extremely small, and it is

conceivable that models err by a factor of a few when estimating this contribution (see Fig. 2.3). However, it has to be noted that this analysis does not rely on the prediction of the absolute level of contamination but only on the prediction of the shape of the discriminant variable ζ in the critical region of $\zeta > 0.6$.
An unaccounted cosmic-ray component at a level of 0.03% of the total primary proton flux can account for the observed excess (assuming that the fraction of background events not described by simulations is energy independent). This is illustrated in Fig. 3.42.

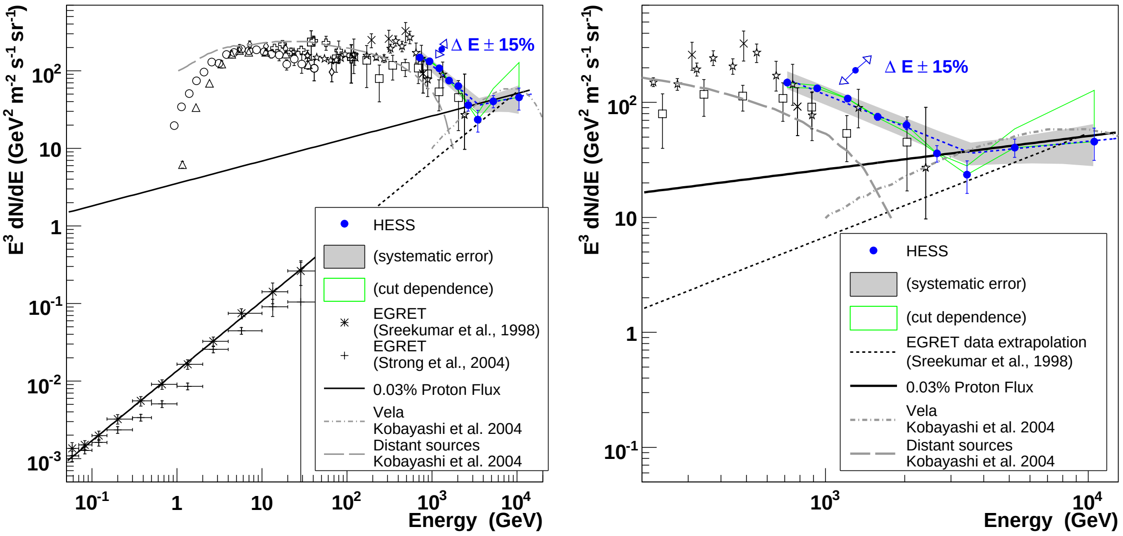

Figure 3.42: *Left*: Spectrum of cosmic-ray electrons together with the EGRET measurement of the extragalactic γ-ray background (Sreekumar et al. (1998), Strong et al. (2004), dashed line is an extrapolation of the fit of Sreekumar et al. (1998)). Also shown is a fraction of 0.03% of the proton flux (thick solid line) and a calculation of the electron flux contribution of distant sources ($d >$1 kpc and $T > 1 \times 10^5$ years) and of the Vela supernova remnant, taken from Kobayashi et al. (2004) (Fig. 6, grey dashed and point-dashed line). *Right*: Zoom in the high-energy region.

Real Signal of Gamma-Ray Showers

If the excess at high energies is not an artefact of the background estimation but really induced by electromagnetic showers, the primary particle is either a γ ray or an electron. As the $X_{\max}$ analysis of Section 3.6.2 showed that a γ-ray origin of the signal cannot be excluded, possible origins of γ rays at these energies are investigated in the following:

- **γ-ray halo around the target source (instrumental or real)**
  Since all observations used for this analysis targeted some known or potential γ-ray source, γ-ray halos that extend beyond the 0.4° of the excluded region can account for the measured signal. These halos could either be technical artefacts due to a poor direction reconstruction or physically motivated in the form of pair halos around AGN (see e.g. Aharonian et al. (1994)). In order to test this hypothesis, spectra are

compared that were obtained from data of fields with a detected target and with no detected target. The high-energy part of the spectrum exists consistently in both data sets. Also variations in the angular cut around the target source as well as a comparison of different types of targets (i.e. AGN vs. other sources that are not expected to exhibit pair halos) did not result in large deviations. Therefore, γ-ray halos around the target sources appear to be an unlikely explanation.

- **Unknown sources in the field of view**
  Since a comparison of spatially different regions yields consistent results, a single source at a particular position can be excluded.
  Multiple sources have to be weak enough as not to be detected and distributed evenly as to feign a diffuse emission from distinct regions. The flux of the measured signal above 3.4 TeV is $\frac{dF}{dE} \approx 2 \times 10^{-11} \left(\frac{E}{1\,\mathrm{TeV}}\right)^{-2.8}$ TeV^{-1} cm^{-2} s^{-1}. If this flux is attributed solely to undetected sources in the field of view (i.e. a cutoff of the electron signal at 3.4 TeV is assumed), this compares to the spectrum of the Crab nebula of $\frac{dF}{dE} = 3.45 \times 10^{-11} \left(\frac{E}{1\,\mathrm{TeV}}\right)^{-2.63}$ TeV^{-1} cm^{-2} s^{-1} (Aharonian et al. (2006a)). For the data set of H 2356-309, which has the highest livetime, the sensitivity of a H.E.S.S. standard analysis is of the order of $\lesssim$ 1% Crab (see Fig. 2.5), which implies the need of $\approx$60 point sources in the field of view to explain the measured flux without significant detection. This appears to be an unreasonably high number.

- **Diffuse extragalactic, galactic background**
  Even if truly diffuse, the emission could be attributed to the diffuse galactic or extragalactic background radiation. However, a galactic diffuse γ-ray origin can be excluded because no dependence on the distance from the Galactic plane was observed. If the signal was of Galactic origin, it would have been expected to drop off with increasing distance to the Galactic plane.
  The extragalactic γ-ray background, which was already discussed in Chapter 1.4, is another potential source of isotropic γ-ray events. The extragalactic γ-ray background as derived from EGRET data is shown in Fig. 3.42 in two different interpretations by Sreekumar et al. (1998) and Strong et al. (2004). The extrapolation of the $E^{-2.1}$ powerlaw derived by Sreekumar et al. (1998) to TeV energies gives a flux which is of the same order as the measured flux. However, extragalactic absorption due to electron-positron pair production should cause spectra of extragalactic γ rays to drop sharply at energies around 100 GeV and 1 TeV (Kneiske & Mannheim (2008), Kneiske (2007)), so that they cannot account for the measured flux.
  Also the local background due to inverse Compton up-scattered solar photons off cosmic-ray electrons is predicted to be negligible due to the strong flux suppression for large angles from the Sun (Moskalenko & Porter (2006), Orlando & Strong (2007)).

Real Signal of Electrons

If the observed signal at energies above 4 TeV is due to cosmic-ray electrons as indicated by the $X_{\max}$ distributions, it can be interpreted as contribution of a very close and recent source of cosmic-ray electrons. Such sources are expected to leave an individual imprint on the spectrum in the TeV domain, which was discussed in Chapter 1. Exemplarily, such a local source contribution is shown in Fig. 3.42 taken from Kobayashi et al. (2004). The observed excess could thus be the contribution of the Vela SNR to the locally measured electron spectrum. However, as a hadronic origin of the signal cannot be excluded with certainty this remains a speculation.

If the spectrum could be extended to higher energies and a cutoff of the signal were observed (as indicated in the Fig. 1.9 and 3.42), this would be a good indication for an electron origin, because a hadronic component is expected to continue just as the hadronic cosmic-ray spectrum does. This is a perspective for future IACT arrays with effective areas beyond 10^6 m^2 like CTA, which should be able to extend the spectrum to 10 TeV and higher using the technique presented in this work.

Chapter 4

Conclusion

This work presents the first measurement of cosmic-ray electrons from ground level, performed with the H.E.S.S. experiment. It extends the measured cosmic-ray electron spectrum to $\approx$10 TeV. How this measurement contributes to the existing picture of cosmic rays is shown in Fig. 4.1.

In contrast to direct measurements with balloon and satellite experiments, this measurement uses air showers that cosmic-ray electrons initiate in the atmosphere. This has the advantage of large effective collection areas of $\approx 10^5$ m^2 compared to only ≈ 1 m^2 of balloon experiments, and is therefore ideally suited to measure the low fluxes of TeV electrons.

The main challenge of this measurement is the determination of the vast hadronic background. Therefore, a new analysis technique was developed that determines the background by a fit of the data with simulations in the classifier ζ obtained from the machine-learning algorithm Random Forest. It is shown that this technique can also be applied to the analysis of diffuse γ rays from the Galactic plane.

The use of simulations for the background determination, however, introduces systematic uncertainties in the analysis because the differential cross sections for hadron production at TeV energies are not exactly known. Proton simulations are based on extrapolations and models are used to describe hadronic interactions. For this analysis, the SIBYLL interaction model was used and, to estimate the effect of model uncertainties, compared with the QGSJET-II model. Additional uncertainties are caused by changes in the atmosphere and the H.E.S.S. energy scale uncertainty.

In addition to the large systematic uncertainties, the indistinguishability of cosmic-ray electrons and γ rays is another major challenge. The analysis makes use of the anisotropic nature of γ rays and amply excludes any γ-ray sources (including the complete Galactic plane) from the data set. The only useful parameter to discriminate between γ rays and electrons is the depth of the shower maximum in the atmosphere. However, due to systematic uncertainties a significant contribution of γ rays seems unlikely but cannot be excluded with certainty. Nonetheless, the diffuse extragalactic γ-ray background is expected to be much lower due to pair production on the cosmic microwave background.

The spectrum measured by H.E.S.S. extends from 300 GeV to $\approx$10 TeV. At energies between 0.3 and 2 TeV there is an overlap with direct measurements of cosmic-ray electrons and a good agreement is observed within the systematic uncertainties. However, the "bump" feature in the electron spectrum that was observed by the ATIC experiment, is not confirmed by the H.E.S.S. data. The H.E.S.S. measurements show a steepening of the

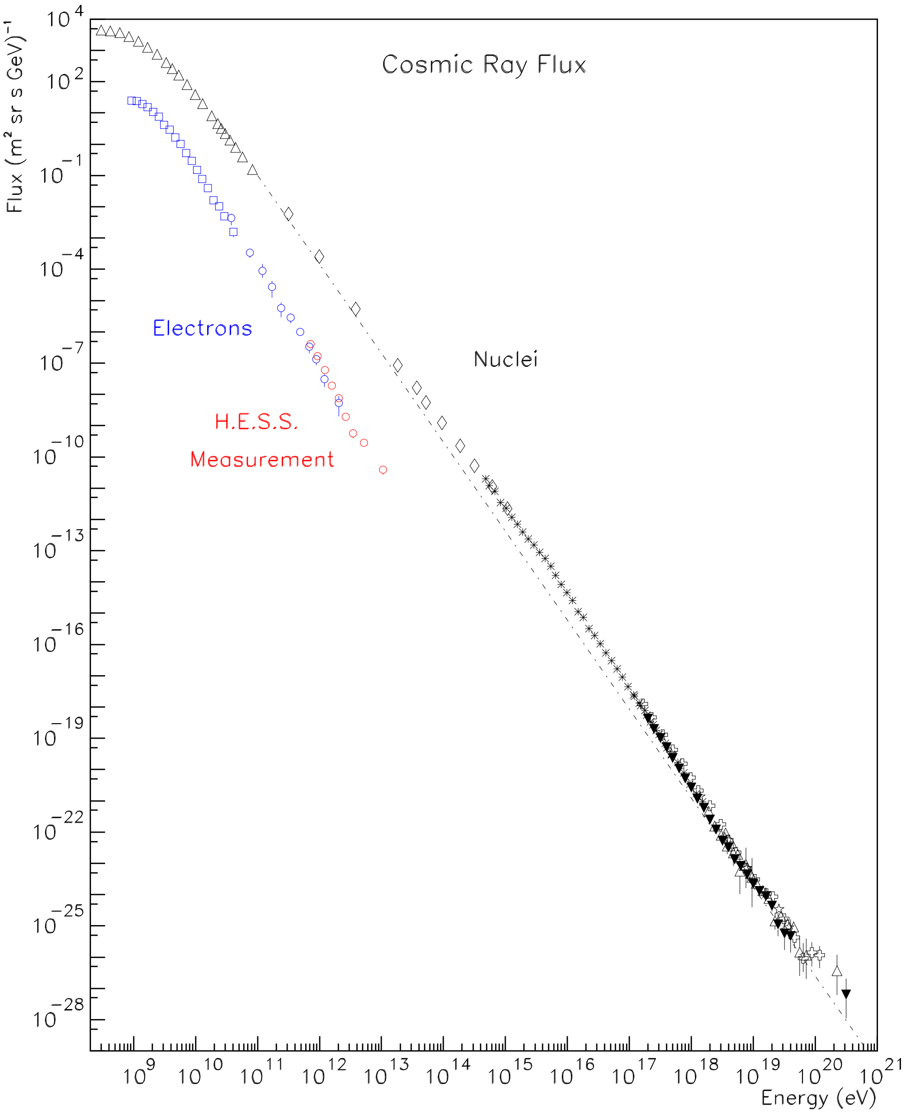

Figure 4.1: The spectrum of cosmic rays [adapted from S. Swordy]. The H.E.S.S. data are shown as red circles.

electron spectrum at ≈900 GeV and at energies beyond 4 TeV a subsequent hardening. Already at a few TeV, the measurement of cosmic-ray electrons implies the existence of a local cosmic-ray electron accelerator within ≈1 kpc distance as VHE electrons lose their energy rapidely via inverse Compton scattering and synchrotron radiation.
Various systematic tests have been performed on the complete electron spectrum, establishing the result as quite stable in the low-energy part and with larger systematic uncertainties in the harder high-energy part. Therefore, the hardening of the spectrum could be due to

an unaccounted proton contribution in the data caused by imperfect simulations. If the signal is of electron origin, it could be the contribution of a very nearby and recent source as the Vela SNR, for example.

If the measurement of cosmic-ray electrons could be extended to higher energies of 10–20 TeV, a cutoff in the spectrum would be a good indication for an electron origin, while a continuation would be evidence for protons causing the spectral hardening. Such measurements can be expected with future IACT arrays with effective areas beyond 10^6 m^2 like CTA or AGIS. With their improved sensitivity they will be able to resolve such features in the high-energy spectrum and possibly measure the end of the cosmic-ray electron spectrum using the technique presented in this work.

Appendix A

Supplementary Figures

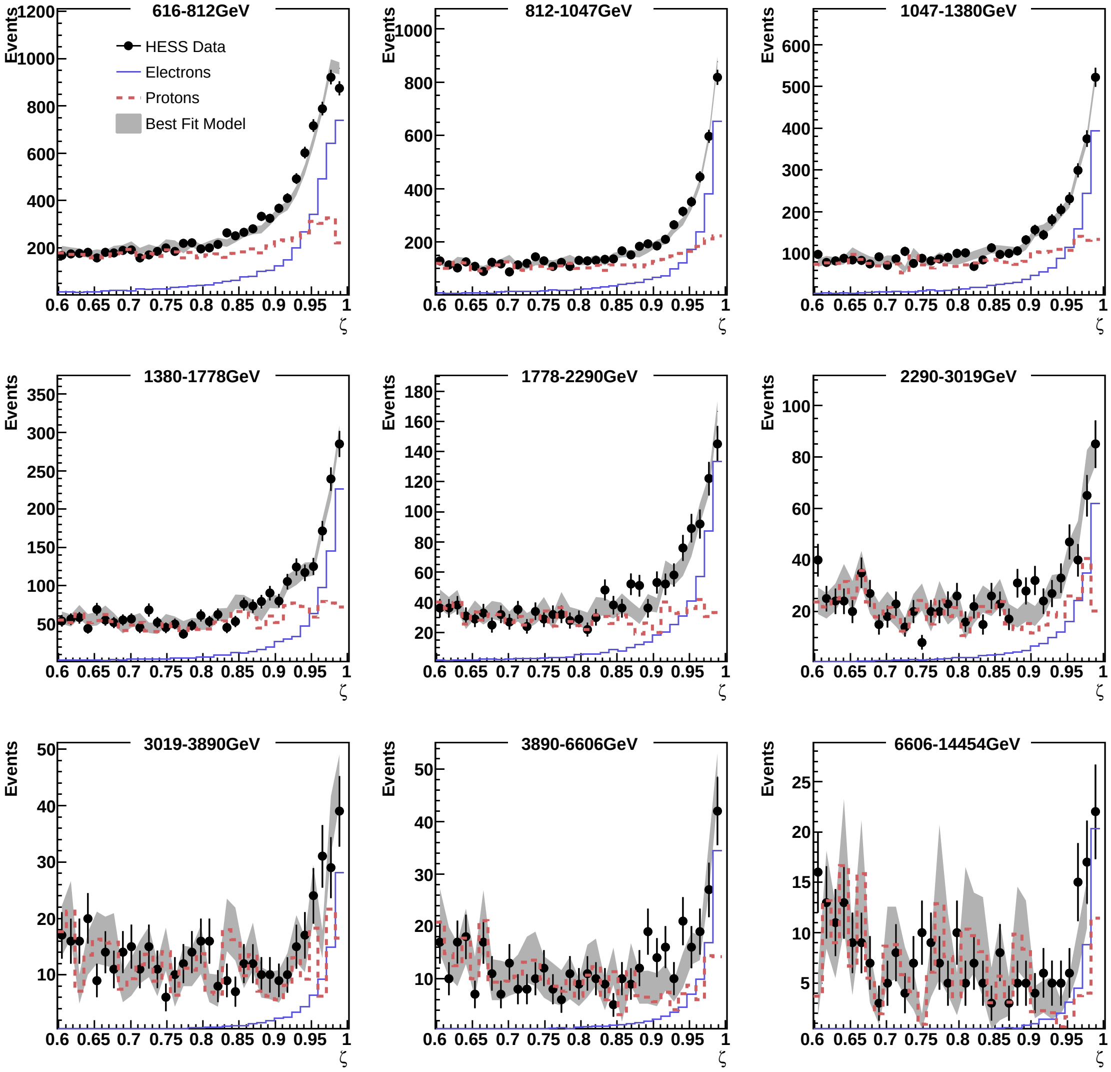

Figure A.1: Fit in the ζ distribution in the energy bands that are used for the spectrum generated with the QGSJET-II hadronic interaction model. H.E.S.S. data are shown in black points, and the best fit model as shaded band. The contributions to the model by electrons are shown in blue, and the proton contribution in form of the red dashed line. Cuts A have been applied.

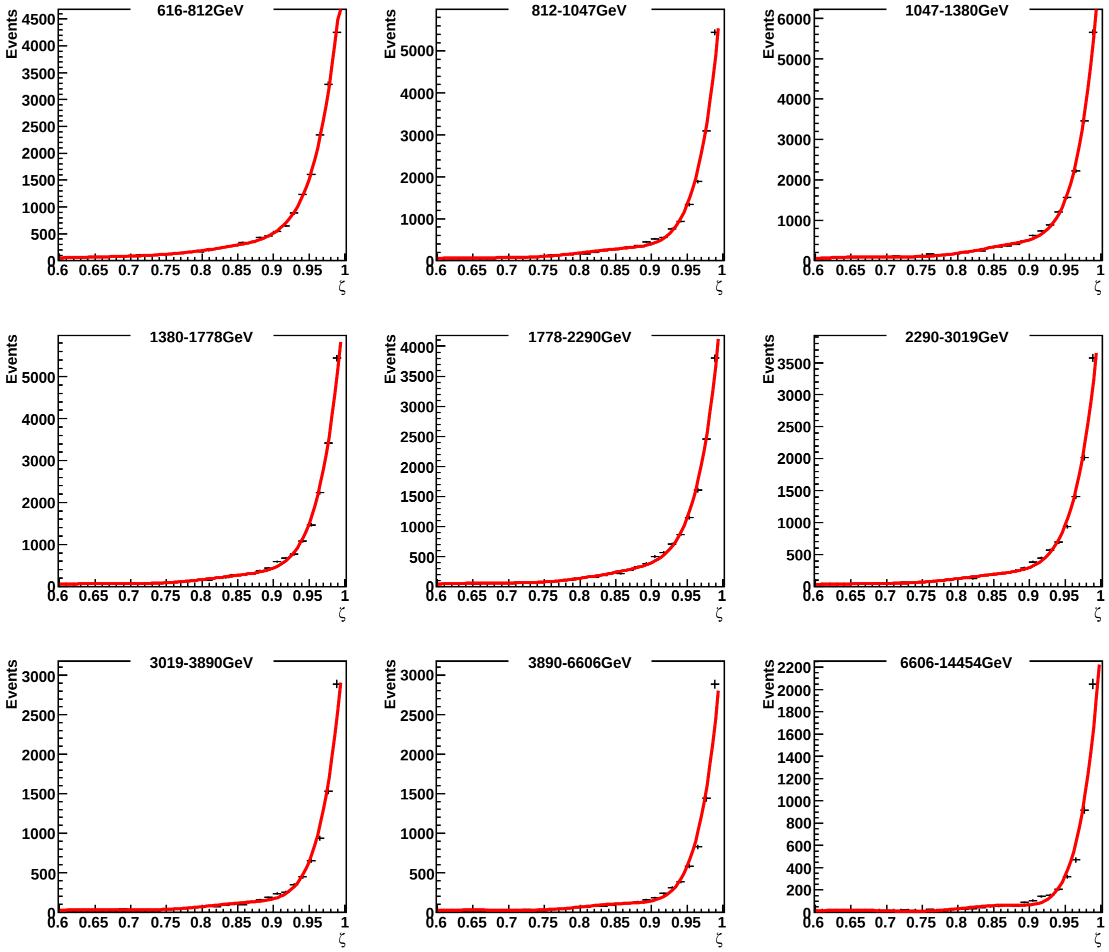

Figure A.2: Error determination: the ζ distribution of simulated electrons in the energy bands together with the fit (red line). Fitted is a 9th order polynomial. The fit is assumed to represent the true values of the ζ distribution.

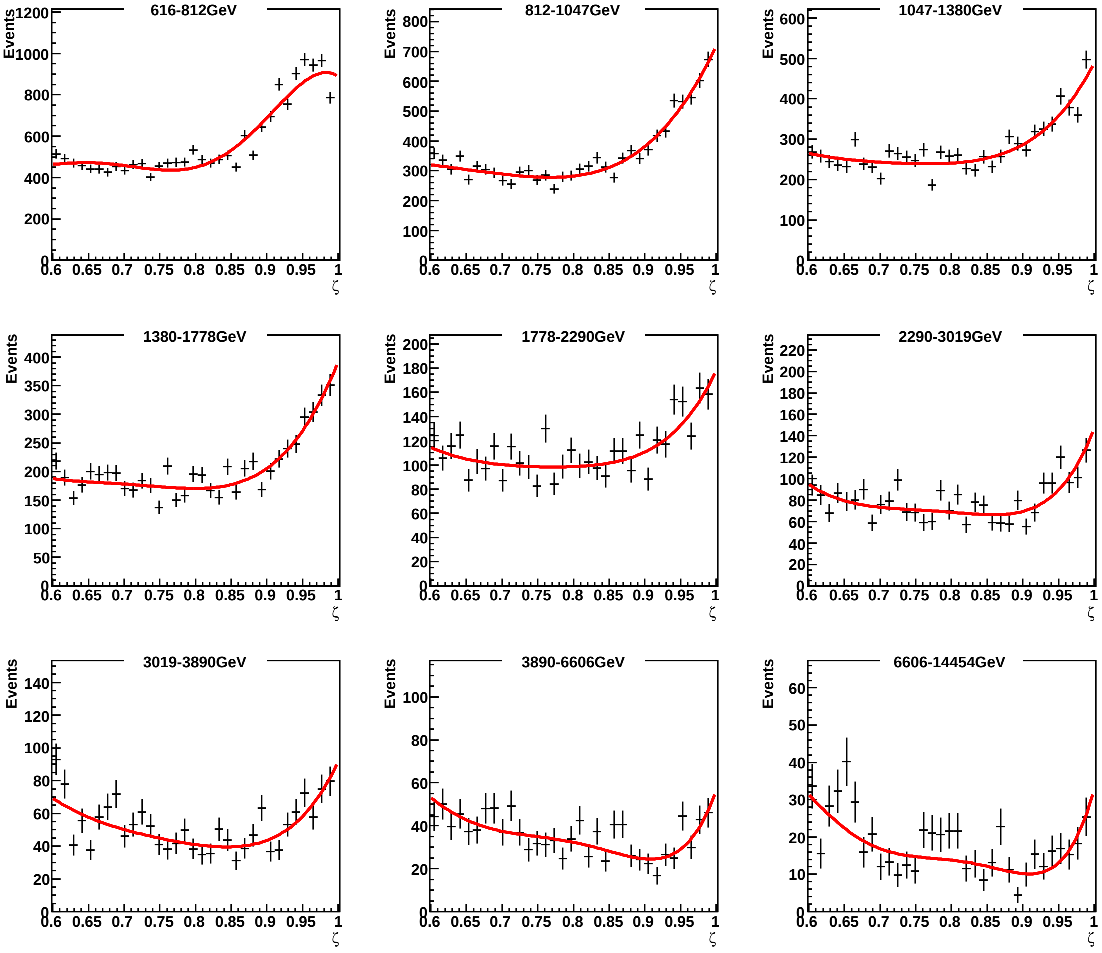
616-812GeV

812-1047GeV

1047-1380GeV

1380-1778GeV

1778-2290GeV

2290-3019GeV

3019-3890GeV

3890-6606GeV

6606-14454GeV

Figure A.3: Error determination: the ζ distribution of simulated protons in the energy bands together with the fit (red line). Fitted is a 5th order polynomial. The fit is assumed to represent the true values of the ζ distribution.

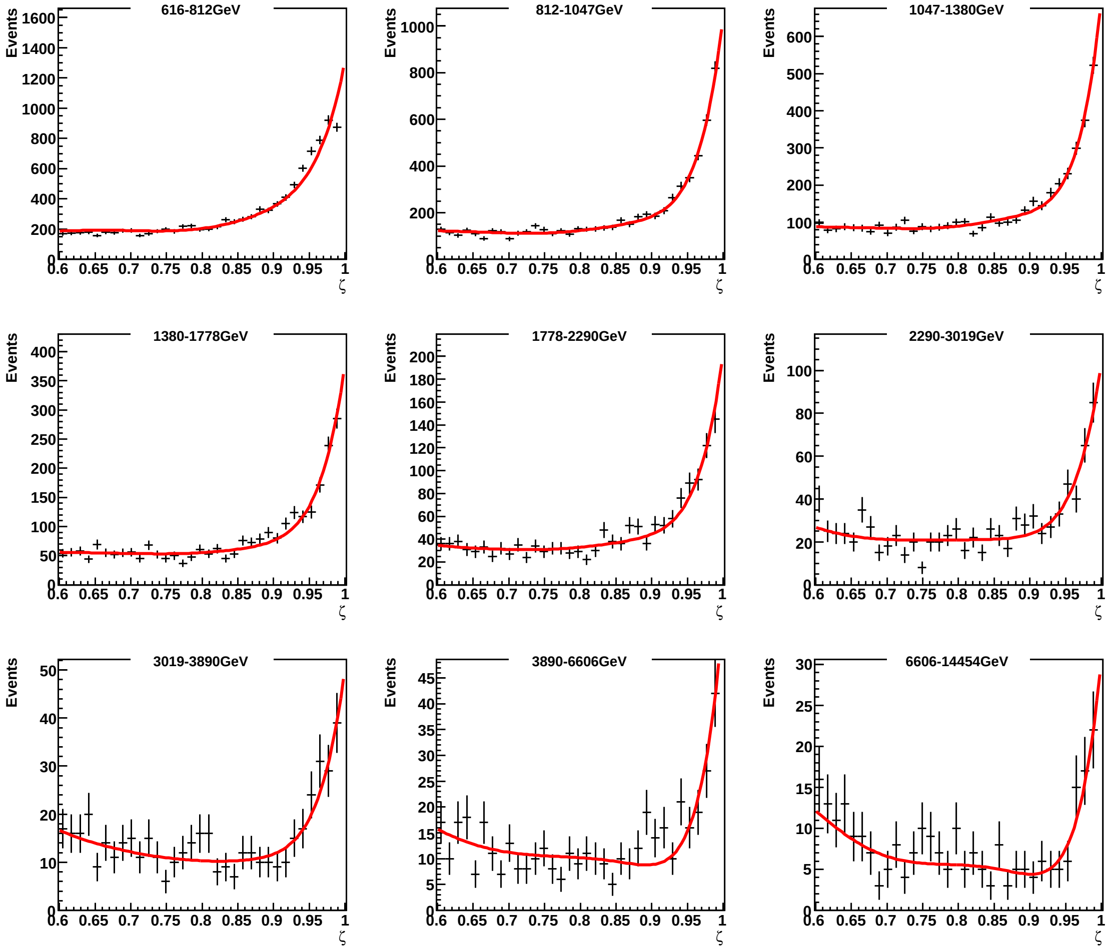

Figure A.4: Error determination: data ζ distribution in the energy bands together with the model $r \cdot e + s \cdot p$ (red line). The model is *no* fit to the data but obtained from the sum of the fits to electron and proton distributions.

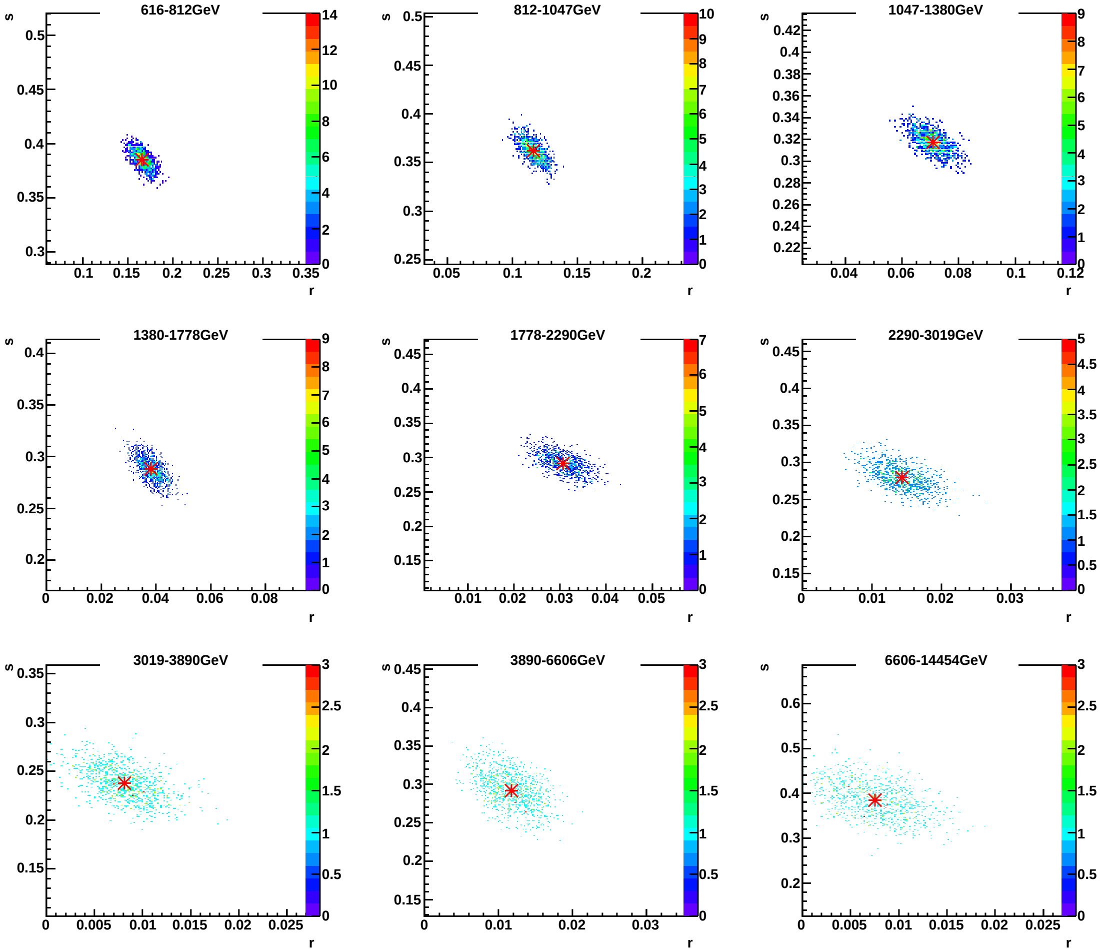

Figure A.5: Error determination: scatter of the $(r,\, s)$ pairs in the different energy bands. The position of $(r_{\text{true}},\, s_{\text{true}})$ is marked by a red star.

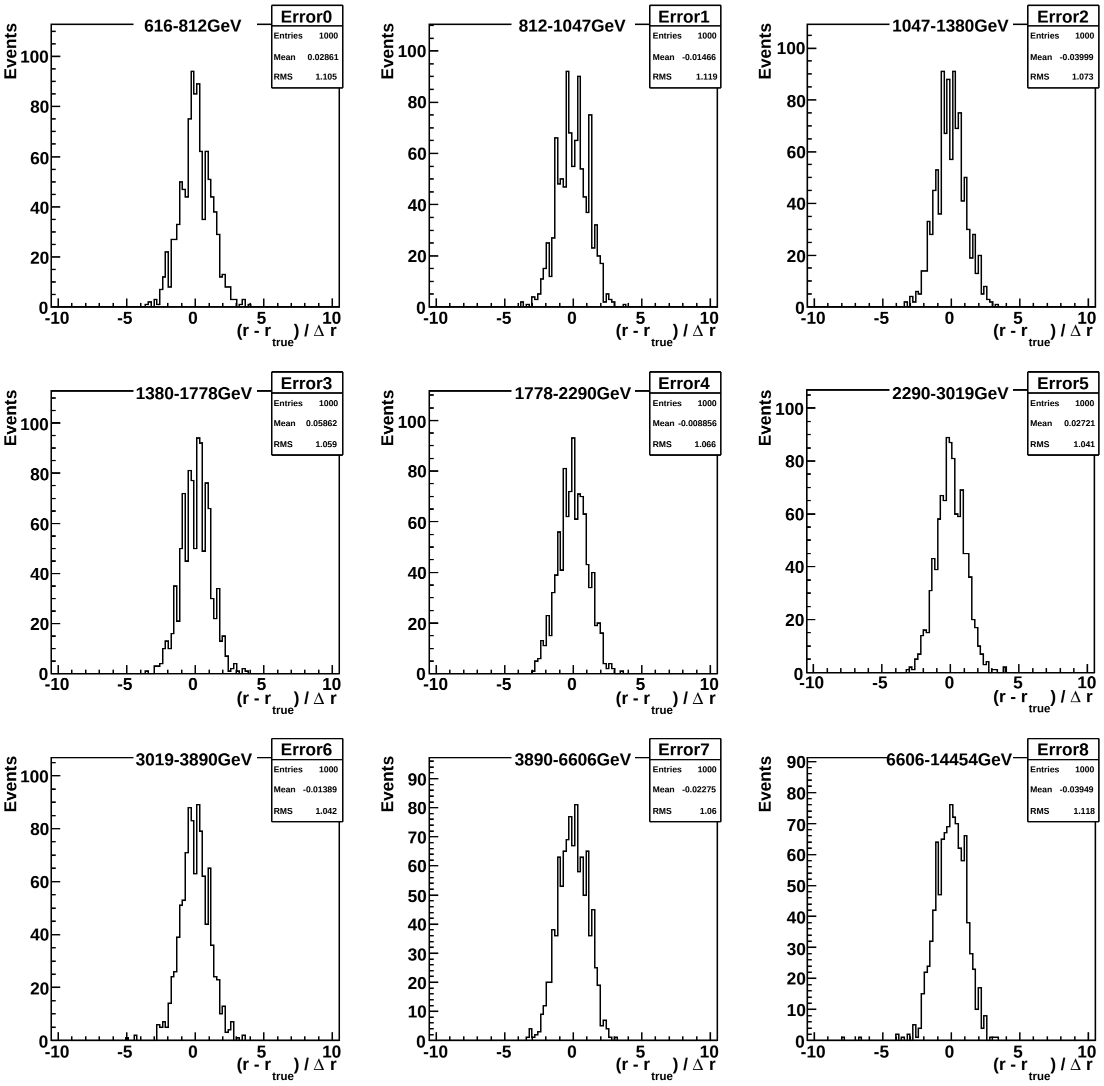

Figure A.6: Error determination: scatter of $(r_{\mathrm{MC}} - r_{\mathrm{true}})/\Delta r$ for both lower and upper errors in the different energy bands.

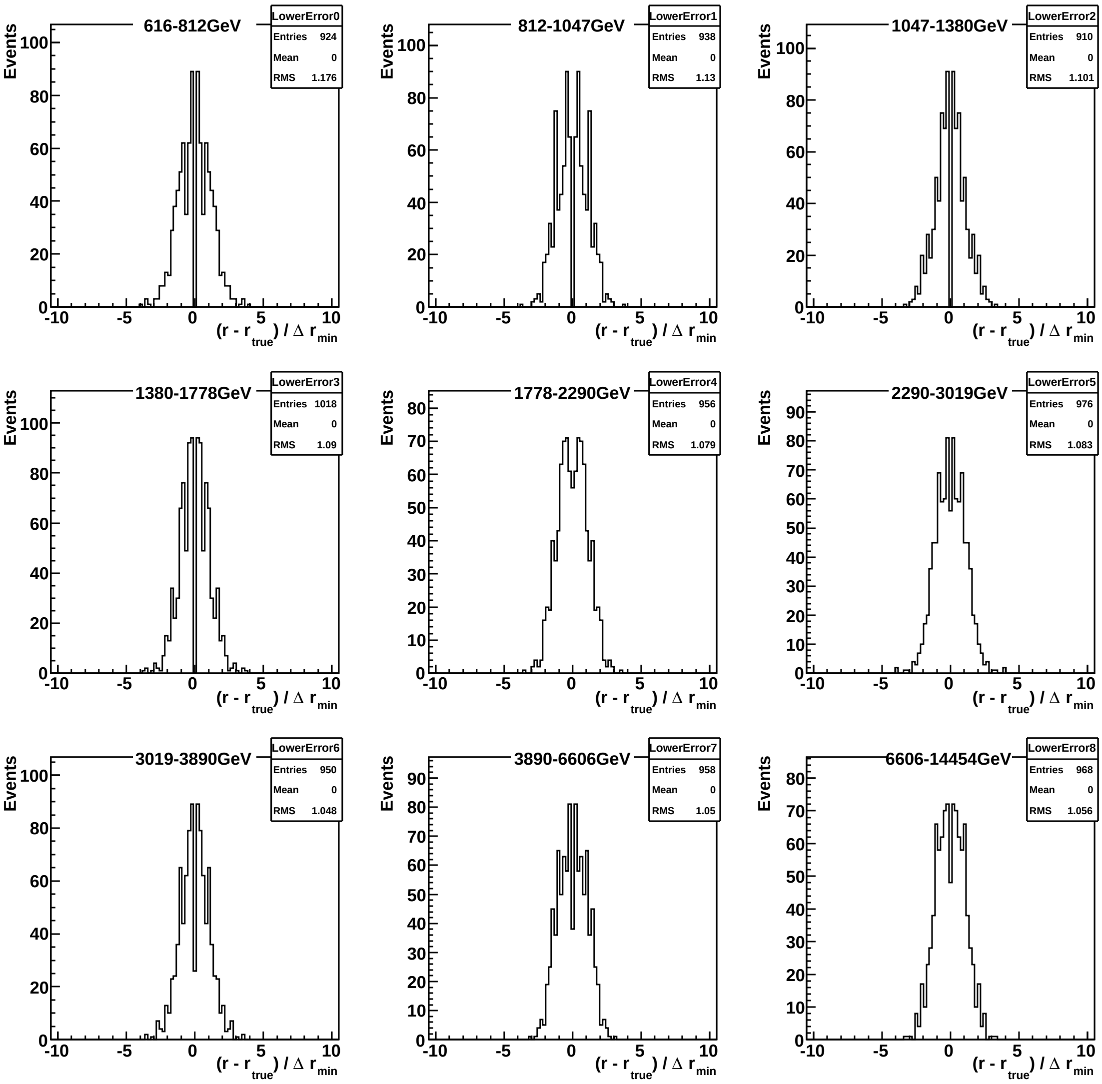

Figure A.7: Error determination: scatter of $(r_{\text{MC}} - r_{\text{true}})/\Delta r$ for the lower errors in the different energy bands. Entries are mirrored at zero in order to obtain the correction factor on the statistical error directly from the RMS. Entries at 0 are missing because the condition r_{MC} strictly larger than r_{true} is used; for the case $r_{\text{MC}} = r_{\text{true}}$, values are recorded in the distributions of Fig. A.8, resulting in the enhancement of the peak at 0 there. However, this is irrelevant for the RMS.

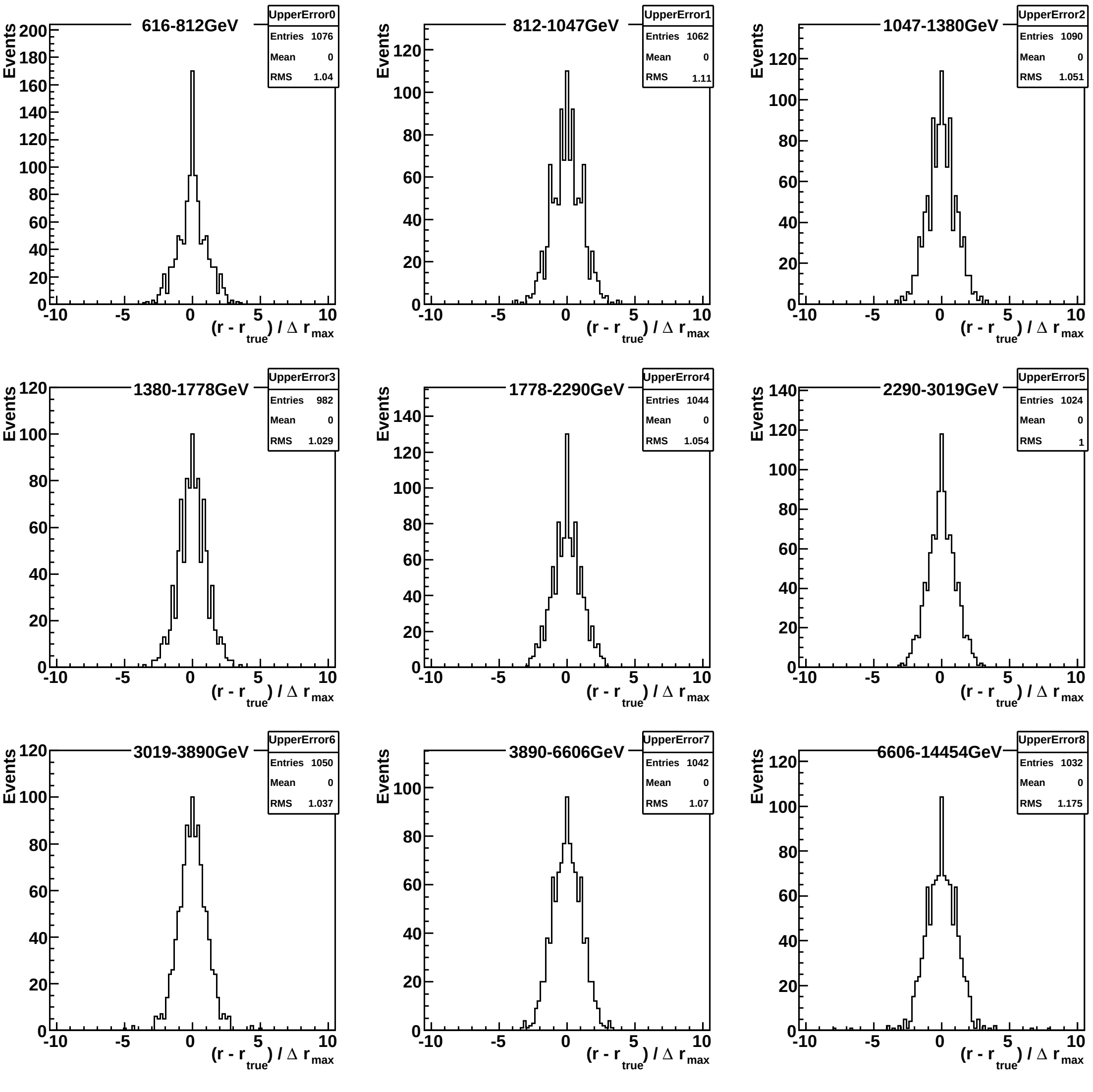

Figure A.8: Error determination: scatter of $(r_{\mathrm{MC}} - r_{\mathrm{true}})/\Delta r$ for the upper errors in the different energy bands. Entries are mirrored at zero in order to obtain the correction factor on the statistical error directly from the RMS. The spikes at 0 are caused by the condition $r_{\mathrm{MC}} \leq r_{\mathrm{true}}$.

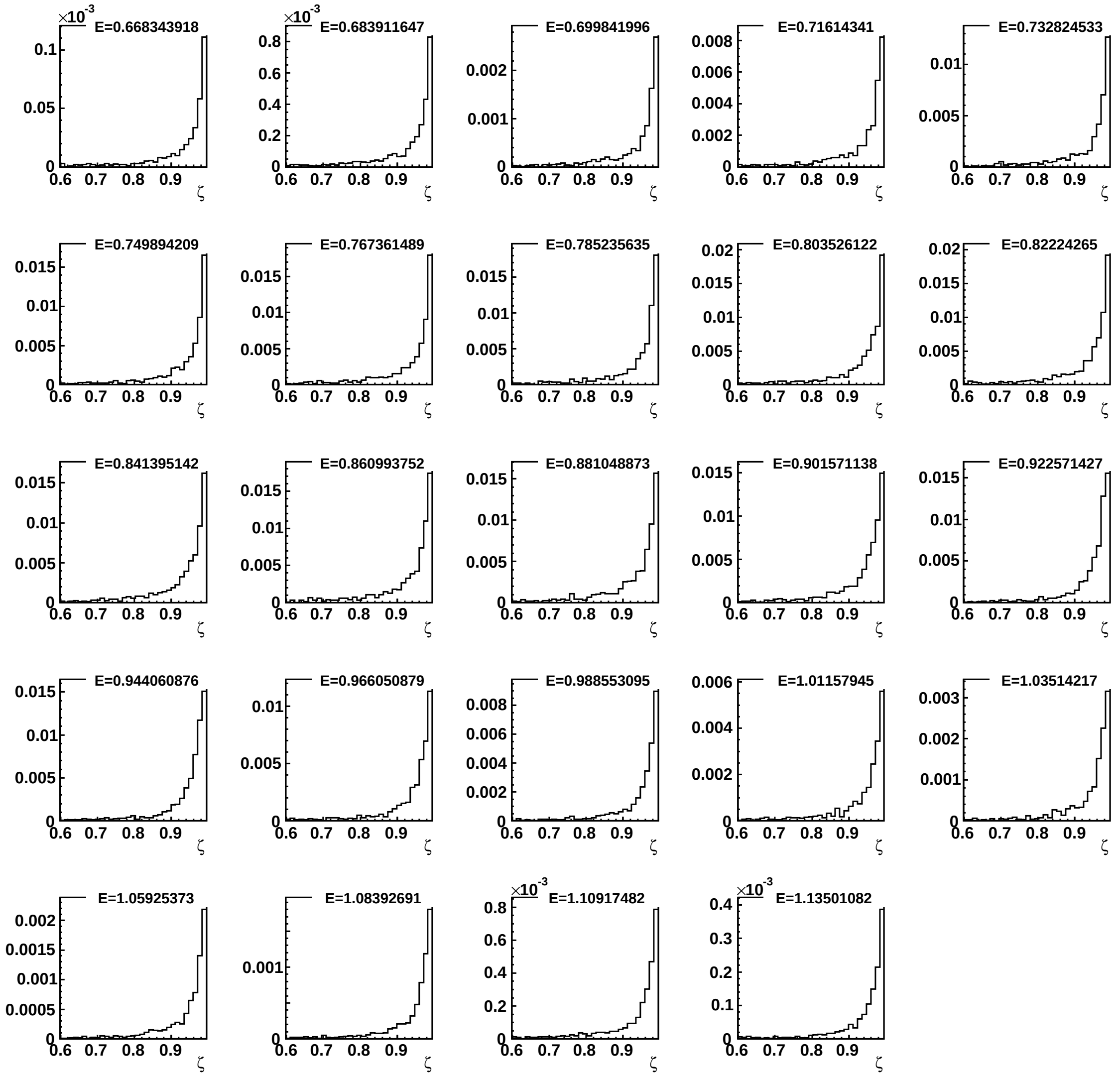

Figure A.9: Muon Correction Mechanism: contributions to the sum of Eqn. 3.10 for the example of the band of corrected energy of 1.04–1.38 TeV for electrons. The distributions are already normalised and scaled by the weighting factor f_i.

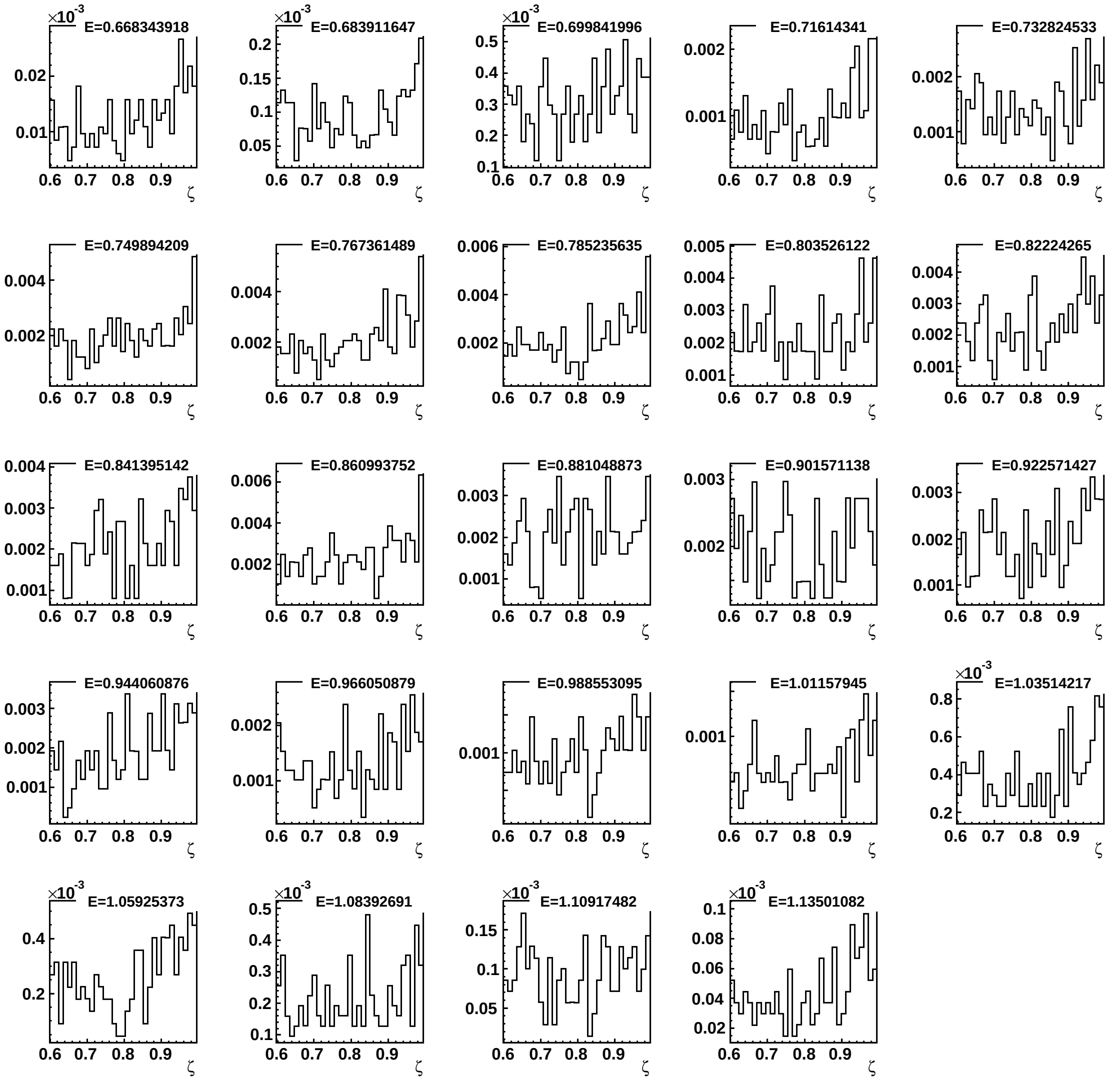

Figure A.10: Muon Correction Mechanism: contributions to the sum of Eqn. 3.10 for the example of the band of corrected energy of 1.04–1.38 TeV for protons. The distributions are already normalised and scaled by the weighting factor f_i.

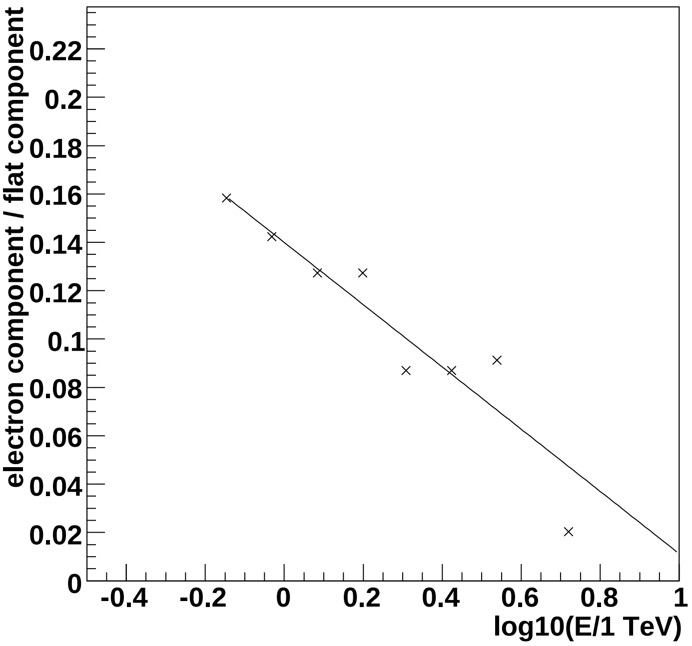

Figure A.11: Systematic test: the ratio of the electron contribution in the proton simulations to the flat component. Fitted is a first order polynomial in the logarithm of the energy. This fit is used to artificially alter the electron component in the proton simulations.

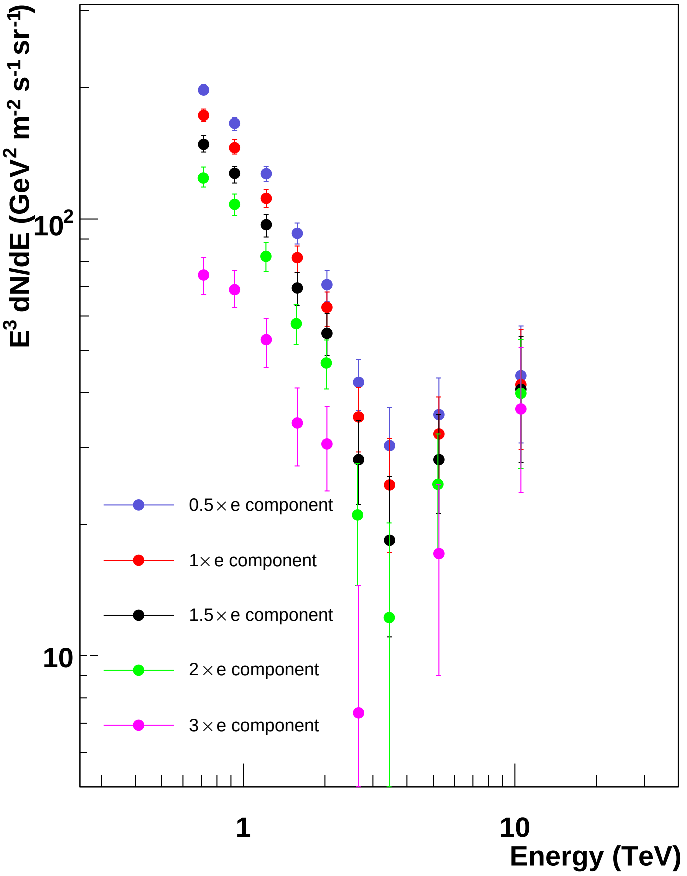

Figure A.12: Systematic test: spectra with modified proton distributions. The ζ distributions of the protons are fitted by a flat and an electron-like component and the electron component is artificially altered for the fit in the data. Shown are spectra obtained with protons with only half of their electron-like component (blue), with once their electron-like component (red, differences to the spectrum of Fig. 3.23 are caused by the generation of the proton distributions with electron-to-flat ratios according to the fit of Fig. A.11 instead of their original values), 1.5 times their electron-like component (black), two times (green), and three times (pink) their electron-like component.

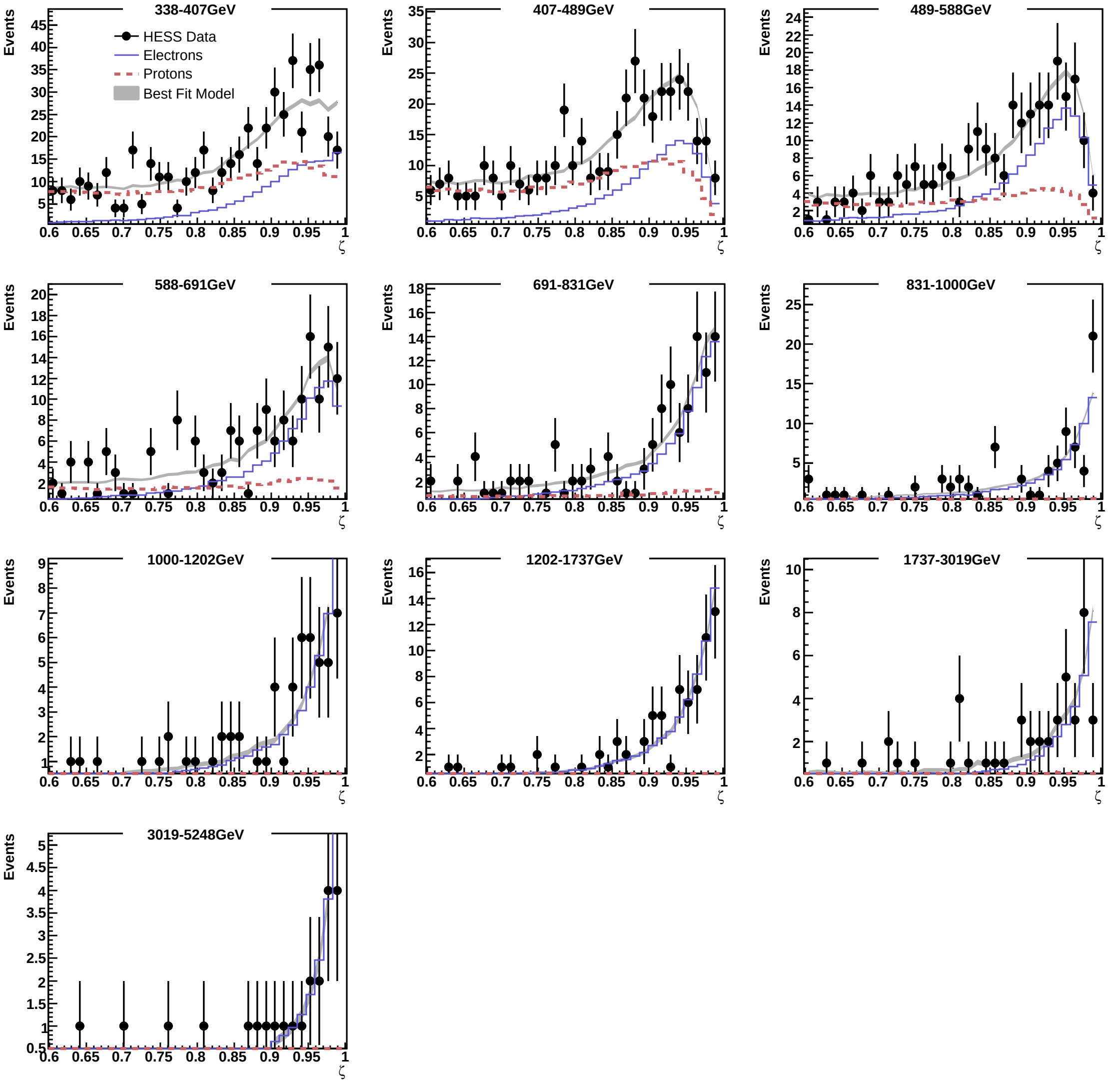

Figure A.13: Systematic test: fits in ζ for the analysis of Sgr A*.

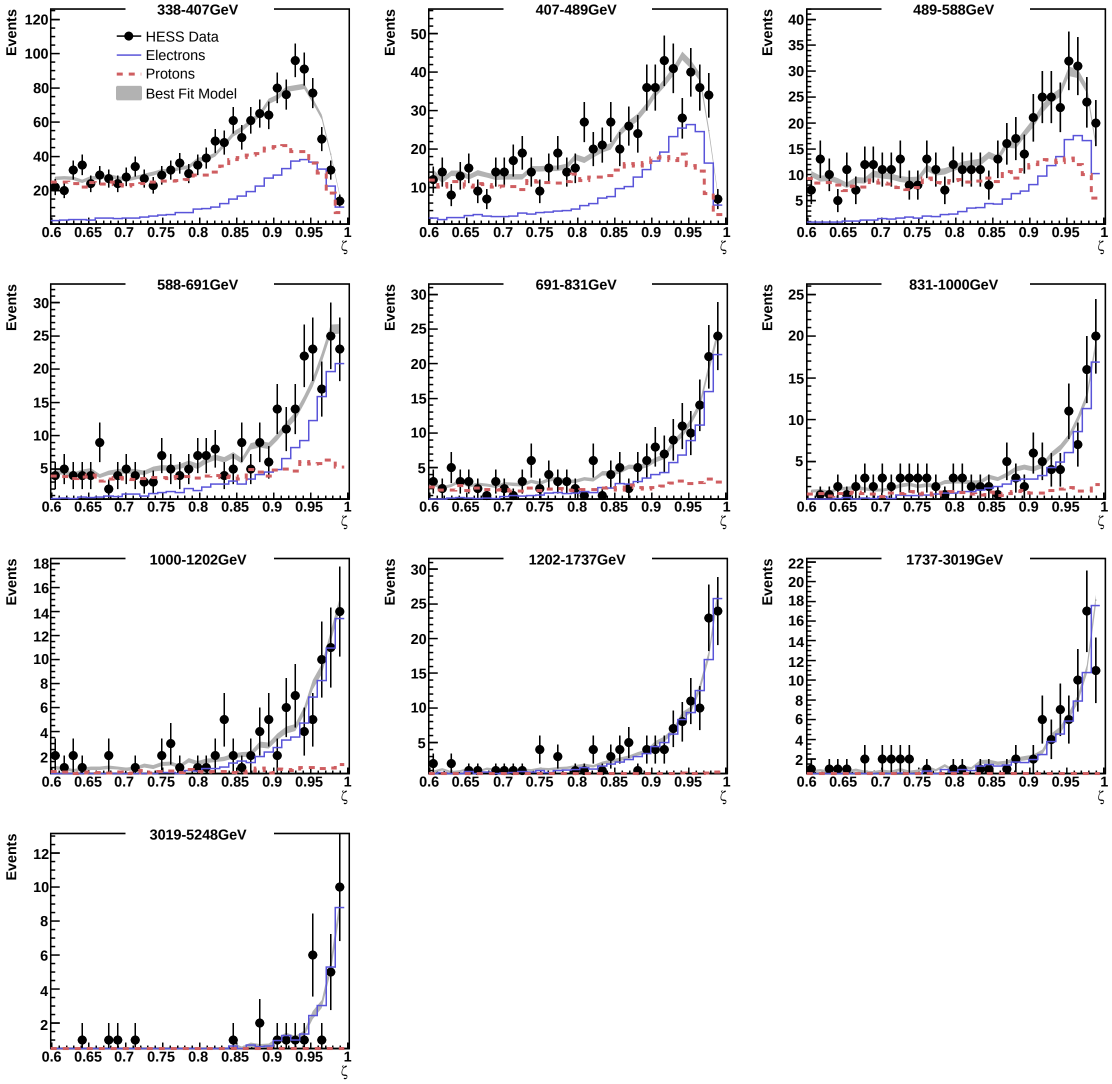

Figure A.14: Systematic test: fits in ζ for the analysis of RX J1713.7-3946.

Appendix B

Application to the Diffuse γ-Ray Emission from the Galactic Plane

For the analysis of cosmic-ray electrons, an analysis method was developed that determines the background of diffuse emission from the phase space of a classifying parameter. This tool can now be used for other applications, too.

For the electron analysis, the region of the Galactic plane was amply excluded from the data set in order to avoid background of diffuse γ rays from the Galactic plane. Although diffuse γ rays are background for the electron analysis, the diffuse γ-ray emission is itself an interesting subject to study.
Diffuse γ rays are closely connected to cosmic rays since they are produced in the interactions of cosmic rays in interstellar clouds. While diffusing through the Galactic Disk, cosmic rays traverse interstellar gas and radiation fields. Protons interact with the ISM via the production of charged and neutral mesons (mainly π) with π^0 decaying to γ rays. Electrons generate γ rays in the interaction with gas by emission of bremsstrahlung and with radiation fields (the cosmic microwave background, starlight and emission from dust at near and far infrared frequencies) via inverse Compton scattering. Therefore, diffuse γ rays can potentially reveal much about cosmic-ray densities and spectra in the central regions of the Galaxy. Diffuse γ-ray emission from the Galactic plane has been first observed by SAS-2, later COS-B and finally, with much increased angular resolution, the EGRET experiment on board the Compton Gamma Ray Observatory in the energy range of 30 MeV–50 GeV (Hunter et al. (1997)). The sky as seen by EGRET is shown in Fig. B.1. If the analysis chain presented in the last chapter is applied to the Galactic plane, it can be used to measure diffuse γ-ray emission. Especially the diffuse emission on large scales is extremely difficult to detect since it is readily subtracted together with the background. For this case a background subtraction that does not rely on spatially displaced background measurements is very convenient.
A few modifications to the analysis are needed in order to obtain spatial information of the γ-ray emission and incorporate the cosmic-ray electrons in the background estimation. These modifications are discussed in Section B.1. In Section B.2, the latitude flux profiles of the Galactic plane between $-48^\circ - 40^\circ$ Galactic longitude as well as an averaged profile are presented.

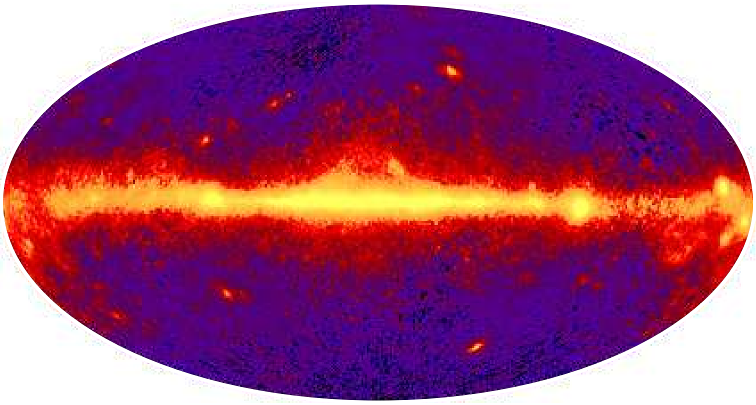

Figure B.1: The EGRET sky with diffuse emission. The Galactic Centre lies in the middle of the image. Taken from Thompson (2008).

B.1 Diffuse γ-Ray Analysis

For the analysis of diffuse γ rays, the methods described in Chapter 3 are used. Especially the background estimation obtained from a fit in the ζ distribution is applied in the same way as described in Chapter 3.3.

Modifications that are needed for this analysis are described in the following sub-sections.

Definition of the Grid

For the electron analysis the energy was the key feature of an event since the measurement aimed at the spectrum. For a measurement of diffuse γ rays, however, this key feature is the direction, since the measurement aims at the spatial distribution of diffuse emission in the Galactic plane. While electrons arrive isotropically and data can therefore be added from different regions in the sky, for diffuse γ rays the direction is crucial. As explained in Chapter 2.2, each recorded event has its direction reconstructed within 0.1°. But since multiple events are needed for the background determination using the fit in the ζ distribution, this accuracy cannot be achieved. Instead, a coarse grid is defined and events having their direction lying in one square are used to determine the γ-ray flux coming from this grid square. The size of the grid squares is chosen such that a reasonable number of events can be found in each single grid square. This is illustrated in Fig. B.2. Observation runs can only contribute to a square if their observation position is close enough that the square fits completely into the central 3° of the field of view. This condition is needed in order to determine the flux per solid angle correctly. For a coarse binning this results in a tremendous loss of data. Therefore, each grid square is further subdivided into smaller divisions not larger than $0.2° \times 0.2°$. In each of these divisions, the runs that fully contain this division are selected. Therefore, different divisions contain data from different runs with different livetimes. The ζ distributions for the fitting procedure and the effective area A_{eff} for the spectrum determination are obtained for each single division (ζ_{div}, $A_{\text{eff, div}}$) and

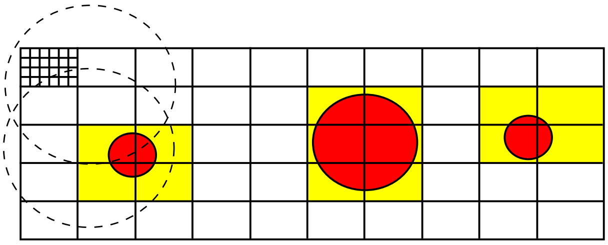

Figure B.2: Schematic drawing of the grid over the Galactic plane. In the upper left corner, the smaller subdivisions of a grid square are illustrated. Red circles symbolise the exclusion regions around γ-ray sources, the grid squares belonging to the extended exclusion region for the analysis of diffuse emission are marked in yellow. Dashed circles indicate the area of one observation run.

summed over all divisions of a square, weighted by the livetime of each division. The ζ distributions are scaled down afterwards to obtain the original statistics of the distributions for the fitting:

$$\zeta_{\text{square}} = \frac{\sum_{\text{div}} \zeta_{\text{div}} \cdot T_{\text{div}}}{\sum_{\text{div}} T_{\text{div}}} \ . \tag{B.1}$$

The effective areas already contain now the livetime information:

$$A_{\text{eff, square}} = \sum_{\text{div}} A_{\text{eff, div}} \cdot T_{\text{div}} \ . \tag{B.2}$$

The fit is then performed in each square of the predefined grid for energies between 0.7 TeV[1] and 4 TeV.

The Offset Dependence

Since not the full field of view is used (as in the case of the electron analysis) but the small divisions of a single grid square, the offset dependence, which was negligible in the electron analysis, becomes relevant. This is of special importance for the effective areas, since the offset dependence of the ζ parameter is only weak (see Fig. 3.5). For completeness, the offset of the ζ distribution is also considered.

To take the offset into account, effective areas and ζ distributions are determined in five offset bands and then interpolated: the bands are equidistant in the square of the offset θ^2 (0–0.45, 0.45–0.9, 0.9–1.35, 1.35–1.8, 1.8–2.25), because the dependence is strongest at large θ and additionally this guarantees an approximately equal number of events in each band due to the quadratic increase of events with offset. The average offset in each band is now $\theta_{av} = \sqrt{\overline{\theta^2}}$, i.e. the square root of the average of the square offset. This offset is assumed to be representative for the data set of the whole band and used for a linear interpolation between the five θ_{av}. In case of the ζ distributions, the original number of events is restored as not to manipulate the statistics for the fitting algorithm. Effective areas are directly multiplied by the solid angle and therefore need no normalisation. A second interpolation is performed between zenith angles as already described in Chapter 3.5.

---

[1] see discussion of the energy threshold in Chapter 3

The Model Components

Also the components of the model that are fitted to the data differ from the electron analysis. In the electron analysis, electron and proton simulations are used. For this analysis, diffuse γ-ray simulations should model the signal. However, the diffuse electron simulations described in Chapter 3.4 are used. The reason is the lack of diffuse γ-ray simulations in all zenith bands. While this looks like an obvious drawback, it is justified by a comparison of the ζ distributions of diffuse electrons and γ rays as is shown in Fig. B.3. Although the two distributions differ significantly, their shape is in a first approximation similar enough to use electron simulations to model γ rays. For an improvement of this method the use of diffuse γ rays is obviously desirable.
For the modelling of the background contribution, extragalactic data excluding the source positions are used. There are two motivations for this approach: firstly, this avoids the systematic uncertainty introduced by the use of proton simulations that was persistent throughout the electron analysis. Secondly, the extragalactic data already contain cosmic-ray electrons, which allows a modelling of the complete background of hadronic and electron cosmic-rays at once. The good agreement resulting from this background modelling can be seen in Fig. B.4.

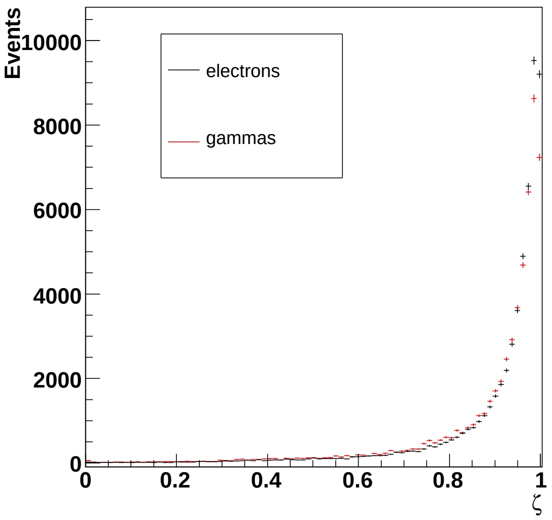

Figure B.3: Comparison of the ζ distributions of electron and γ-ray simulations in the energy range of 0.7–4 TeV. The distributions differ significantly, but are still similar enough to use electron simulations as approximation for diffuse γ rays.

Modification in the Fitting Algorithm

Crucial for the averaging over Galactic longitude slices that is done in Section B.2 is the extension of the fitting range to allow for negative γ-ray contributions and therefore negative fluxes. This guarantees that in the process of averaging, fluctuations cancel out

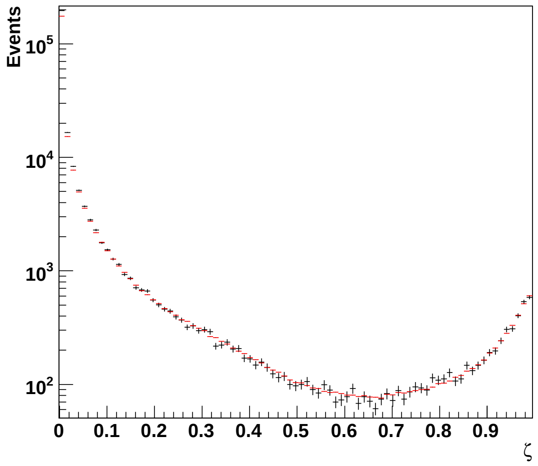

Figure B.4: Comparison of data from the Galactic centre and the best fit model consisting of extragalactic data and a strong γ-ray component modelled by electron simulations. Besides the very low ζ values, which do not participate in the fit, a very good agreement is obtained.

instead of summing up. This is only a minor change: In the definition of the bin likelihoods (Eqn. (3.2)),

$$\mathrm{L}_i = P(p_i|\tilde{p_i}) \cdot P(e_i|\tilde{e_i}) \cdot P(d_i|r \cdot \tilde{e_i} + s \cdot \tilde{p_i}) \ , \tag{B.3}$$

the value of r has to be allowed for negative values, the Poisson distributed values p_i, e_i, and d_i remain positive. This works only if the background dominates.

Data Selection

For the γ-ray analysis, data of the Galactic plane between a Galactic longitude of $-48°$ and $40°$ are used. The zenith angle cut is loosened, since the extragalactic data used for the background modelling is available at many zenith angles. Limiting factor are now the electron simulations that are available only up to $40°$ zenith angle. Therefore, only data at zenith angles $< 35°$ are chosen. This reduces the available data by $\approx$40%. The same data quality criteria as described in Chapter 3.4 are applied.

These data are now used to determine the flux between 0.7 and 4 TeV according to Eqn. (3.7) for a grid over the Galactic plane.

B.2 Results

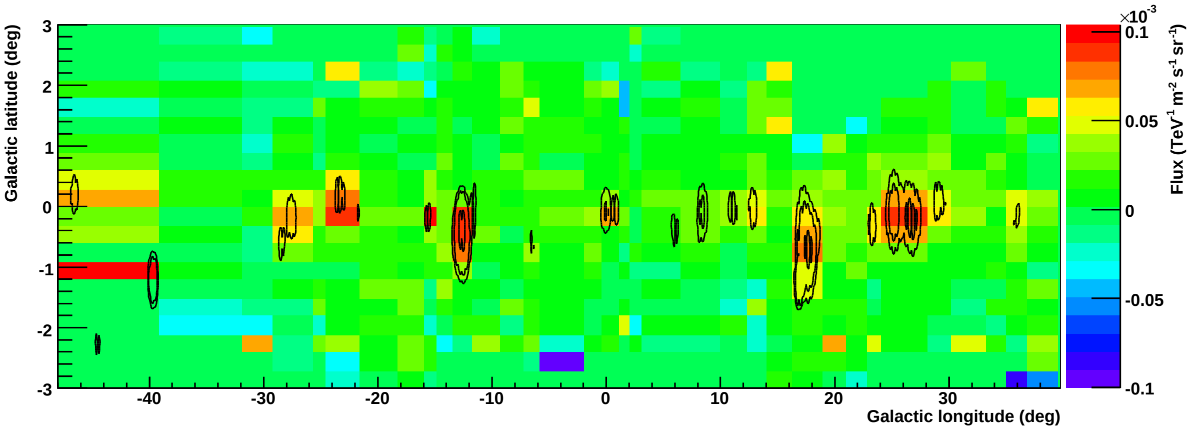

Figure B.5: Flux distribution in the Galactic plane obtained by an analysis of diffuse emission using a fit in the ζ classifier. Overlaid are contours of excess events obtained by the H.E.S.S. standard analysis of the Galactic plane.

The result of this analysis of the Galactic plane is shown in Fig. B.5. Overlaid in contours are a map of background subtracted γ-ray events obtained by the H.E.S.S. standard analysis. Clearly visible are the bright H.E.S.S. sources of the Galactic plane, which coincide with the areas of high fluxes obtained with this analysis. This agreement is a first check on the presented method. Besides this agreement, the meaning of this map is very limited as there is no means of visualising the errors on the flux values. The single high fluxes or negative fluxes are generally not significant.

B.2.1 Latitude Slices

To obtain a meaningful presentation of this result, single slices in latitude are shown in Fig. B.6, B.7, B.8, B.9, and B.10. The positions of the exclusion regions around H.E.S.S. sources and *hot spots* (regions of enhanced γ-ray emission with a significance below $5\,\sigma$) are marked with a red line, the corresponding source is indicated above. Any large deviations of the fluxes from zero are at the positions of these γ-ray sources. Although a few slices seem to show some excess outside the exclusion regions, the significance of these excesses is always very limited.

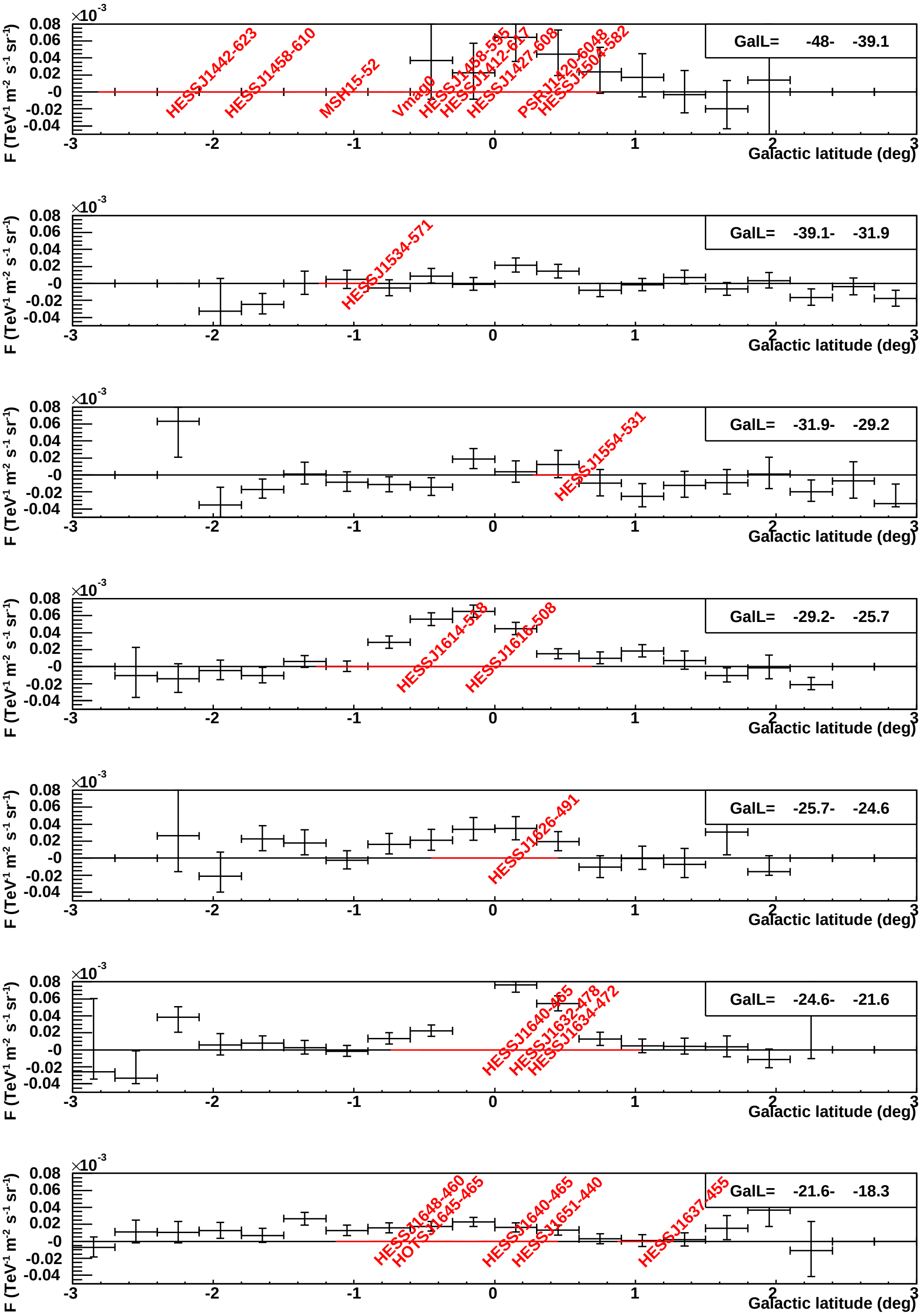

Figure B.6: Slices through the Galactic plane, for Galactic longitude bands between $-48°$ and $-18.3°$.

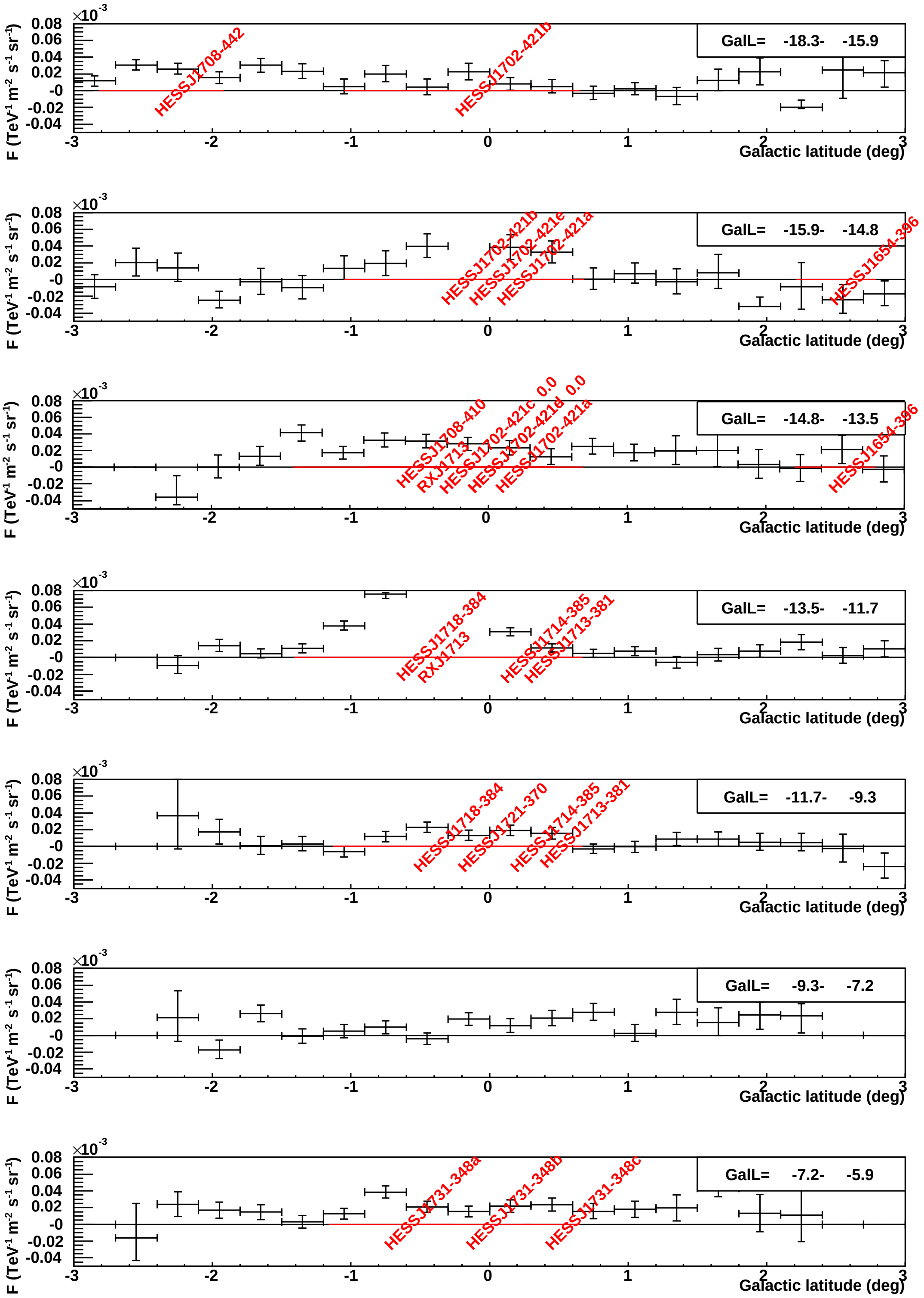

Figure B.7: Slices through the Galactic plane, for Galactic longitude bands between -18.3° and -5.9°.

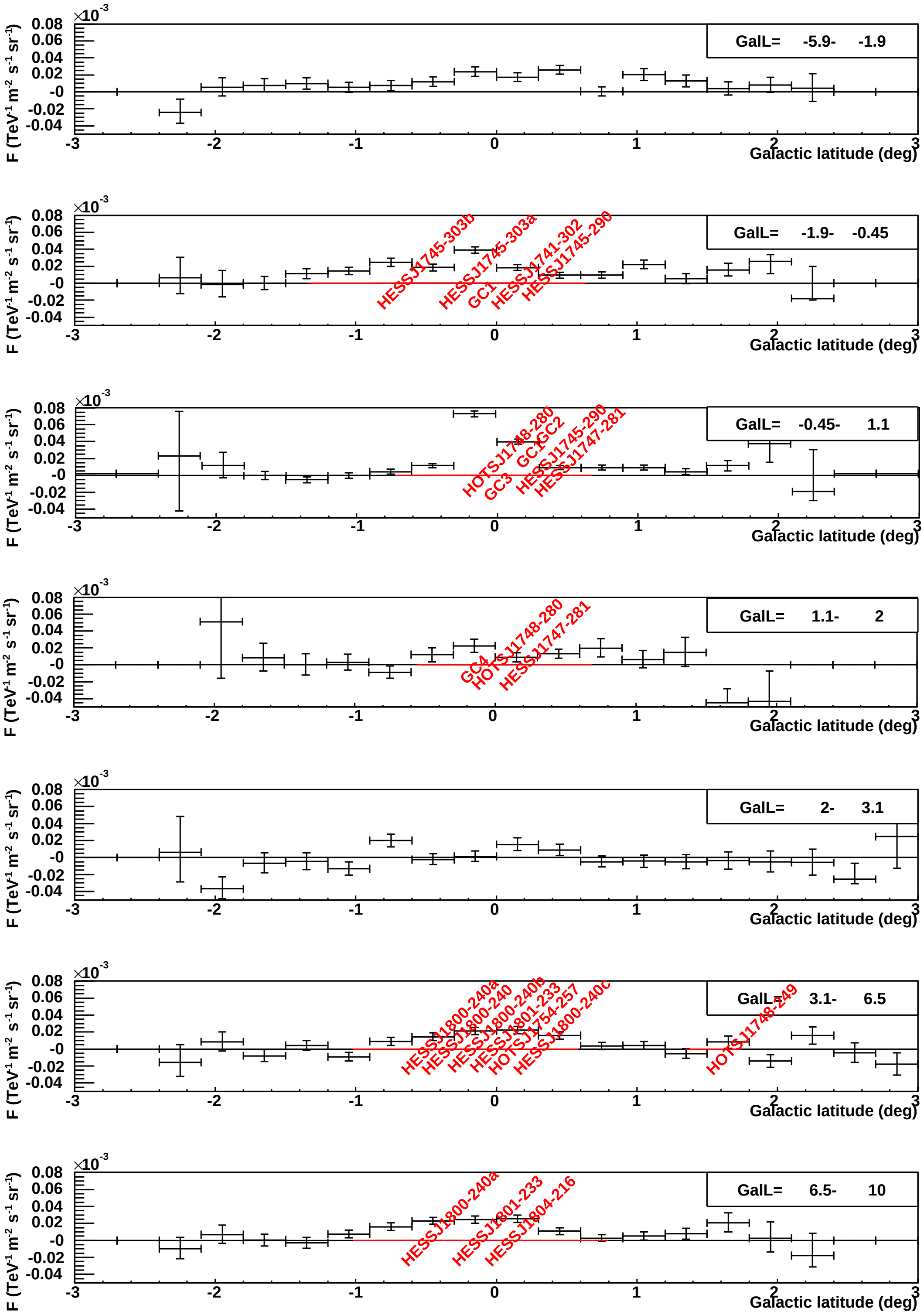

Figure B.8: Slices through the Galactic plane, for Galactic longitude bands between −5.9° and 10°.

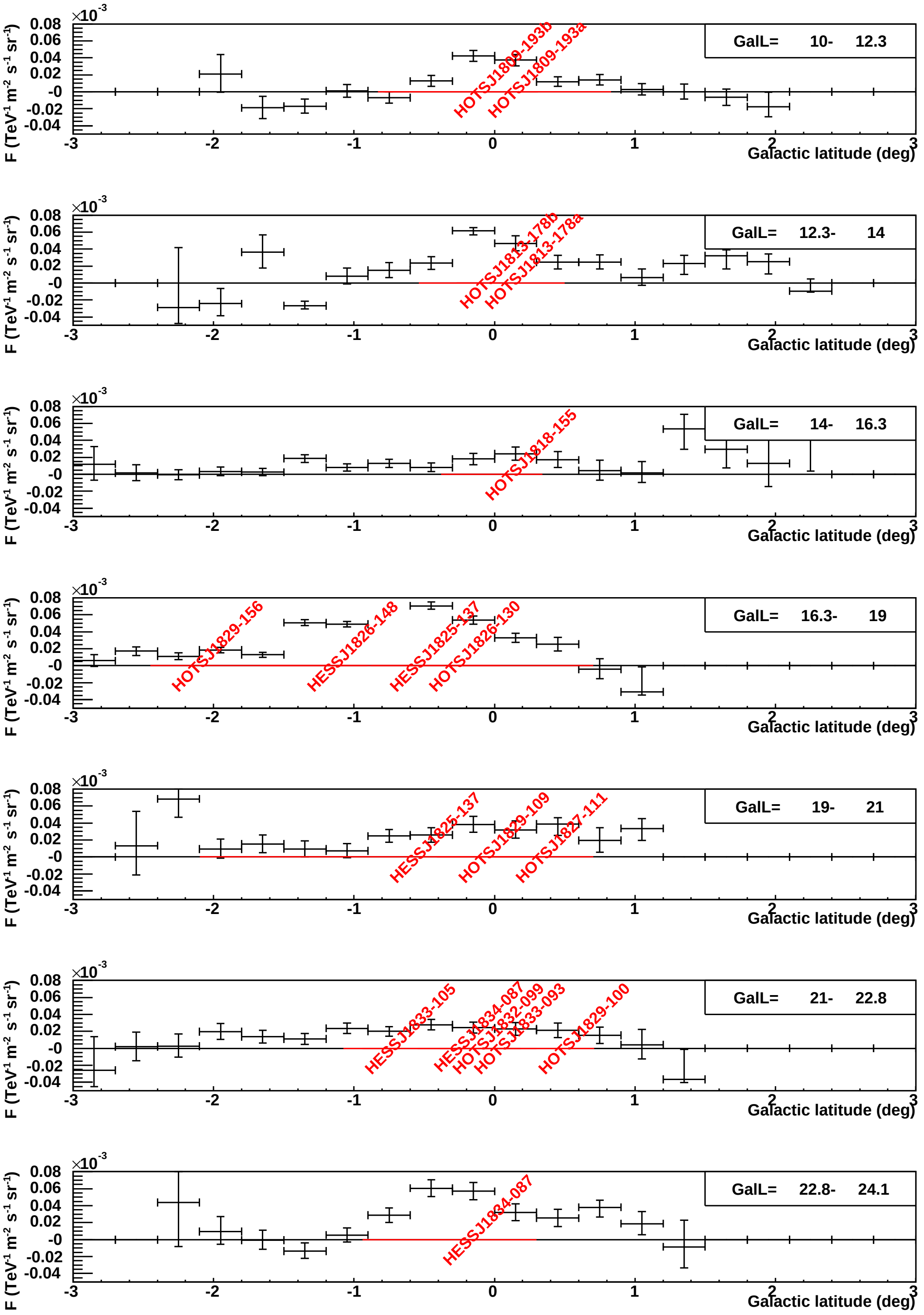

Figure B.9: Slices through the Galactic plane, for Galactic longitude bands between 10° and 24.1°.

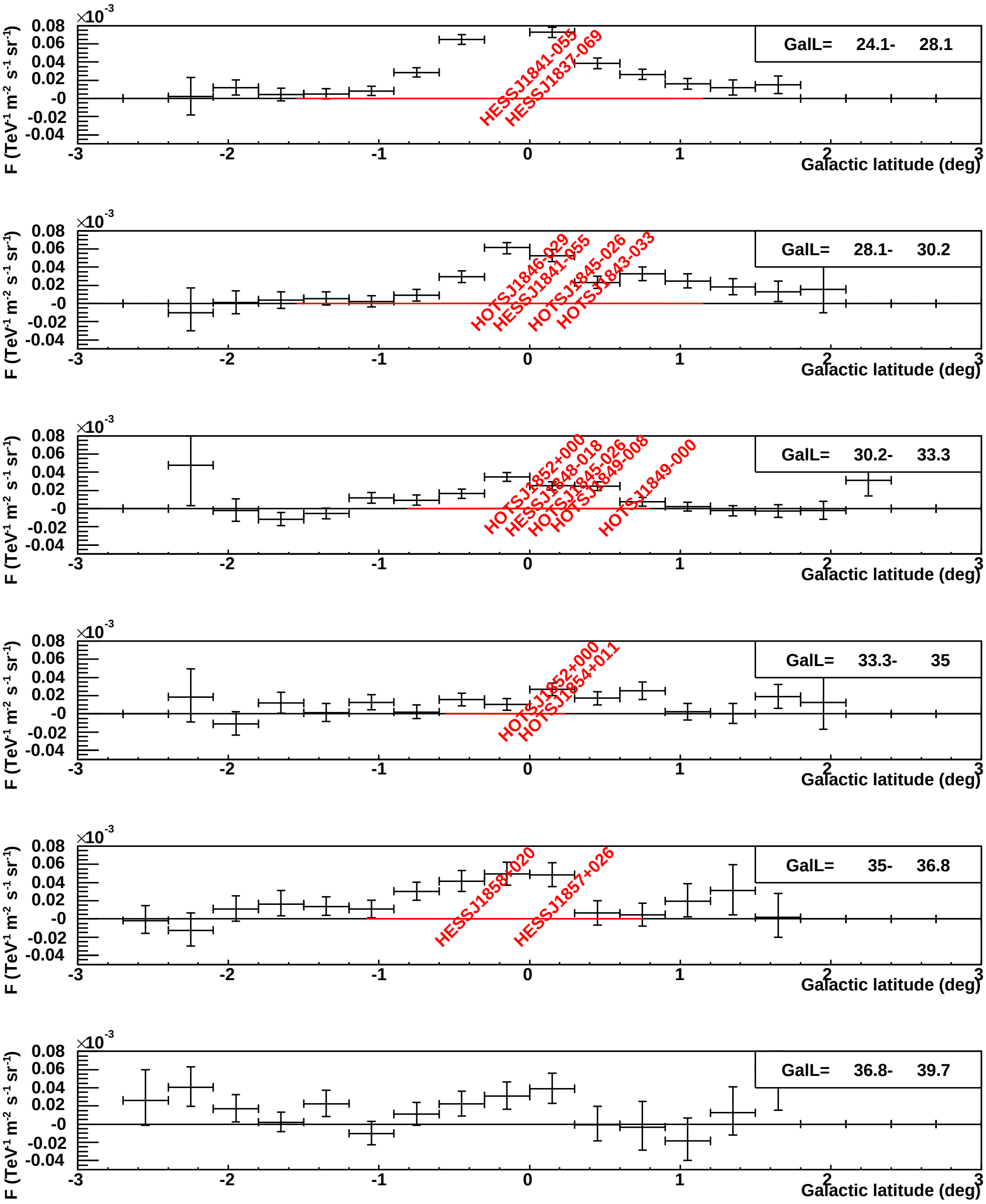

Figure B.10: Slices through the Galactic plane, for Galactic longitude bands between 24.1° and 39.7°.

B.2.2 Average over Galactic Longitude

For better statistics, the slices in Galactic latitude are averaged over all longitude positions, each slice weighted by its extension in Galactic longitude. A distinction is made whether a single grid square is part of an exclusion region or not. Since the grid squares are generally much larger than the exclusion regions themselves, this leads to an *extension* of the exclusion regions, which is visualised in Fig. B.2. The flux profiles of the single slices are averaged once for all grid squares including those that contain γ-ray sources and hot spots, and once only for those squares that are not part of the extended exclusion regions. The resulting profiles are shown in Fig. B.11. The flux distribution of all data including γ-ray sources peaks at Galactic latitude = 0, and falls off at both sides. This is the behaviour expected from the distribution of γ-ray sources in the Galactic plane. Also for the case of excluded sources, a significant excess over zero is observed. The flux distributions of the single latitude bins are shown in Fig. B.12. The latitude distribution again peaks at zero, corresponding to the distribution of target material for cosmic-ray interactions, which is highest directly in the Galactic plane.
It has to be stressed at this point that the relative heights of the two curves have no meaning. This is because of the arbitrary and coarse binning that excludes parts of the sky without any γ-ray sources because they are contained in a grid square scratching a γ-ray source/exclusion region, but normalises the flux to the total area.
While an interpretation of this result is beyond the scope of this work, Fig. B.11 indicates the existence of diffuse emission of VHE γ rays in the Galactic plane. A possible systematic effect in this measurement is the night sky background, which has to be evaluated for any conclusive results.

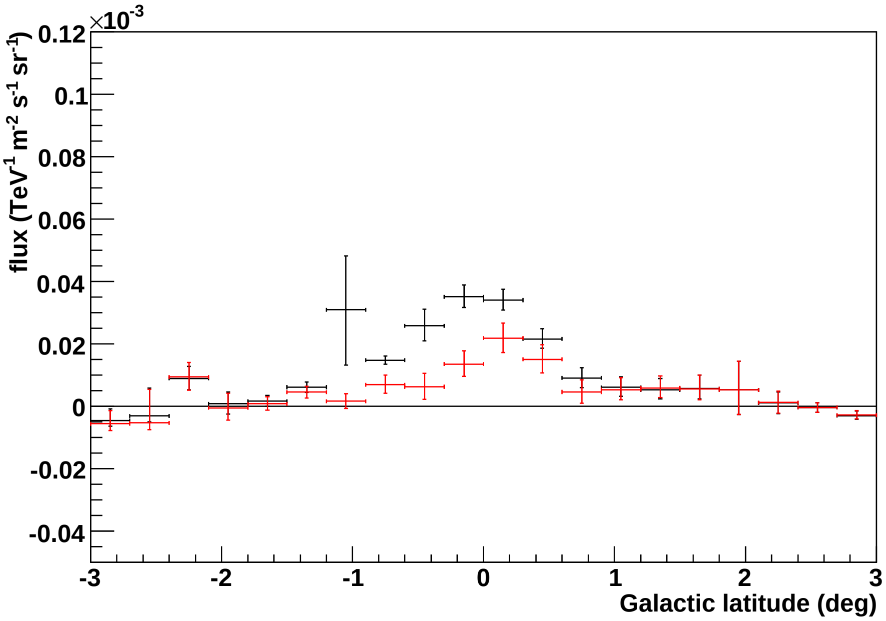

Figure B.11: Diffuse γ-ray flux as function of Galactic latitude. Red: diffuse emission, with all γ-ray sources excluded, black: the total data set containing γ-ray sources.

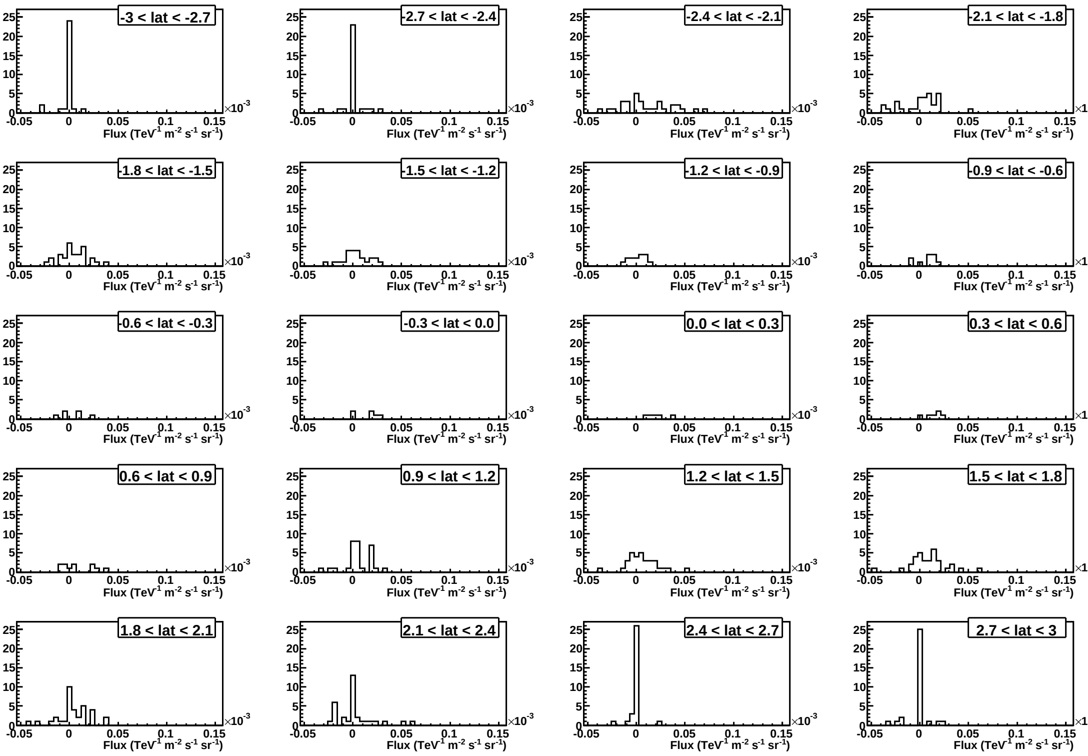

Figure B.12: The distribution of fluxes in each latitude bin of Fig. B.11 for the case of the excluded sources.

Bibliography

Abraham, J. et al. 2004, Nuclear Instruments and Methods in Physics Research A, 523, 50

Achterberg, A., Gallant, Y. A., Kirk, J. G., & Guthmann, A. W. 2001, MNRAS, 328, 393

Adriani, O., Barbarino, G. C., Bazilevskaya, G. A., et al. 2008, arXiv:astro-ph/0810.4995

Aguilar, M., Alcaraz, J., Allaby, J., et al. 2002, Physics Reports, 366, 331

Aharonian, F., Akhperjanian, A. G., Aye, K.-M., et al. 2005, Science, 307, 1938

Aharonian, F., Akhperjanian, A. G., Aye, K.-M., et al. 2004a, Astroparticle Physics, 22, 109

Aharonian, F., Akhperjanian, A. G., Barres de Almeida, U., et al. 2008a, Physical Review Letters, 101, 261104

Aharonian, F., Akhperjanian, A. G., Bazer-Bachi, A. R., et al. 2007a, ApJ, 664, L71

Aharonian, F., Akhperjanian, A. G., Bazer-Bachi, A. R., et al. 2006a, A&A, 457, 899

Aharonian, F., Akhperjanian, A. G., Bazer-Bachi, A. R., et al. 2006b, Nature, 440, 1018

Aharonian, F., Akhperjanian, A. G., Bazer-Bachi, A. R., et al. 2007b, Phys. Rev. D, 75, 042004

Aharonian, F., Akhperjanian, A. G., Bazer-Bachi, A. R., et al. 2007c, A&A, 464, 235

Aharonian, F., Akhperjanian, A. G., Bazer-Bachi, A. R., et al. 2007d, ApJ, 661, 236

Aharonian, F. A., Akhperjanian, A. G., Aye, K.-M., et al. 2004b, Nature, 432, 75

Aharonian, F. A., Atoyan, A. M., & Völk, H. J. 1995, Astron. & Astrophys., 294

Aharonian, F. A., Coppi, P. S., & Völk, H. J. 1994, ApJ, 423, L5

Aharonian, F. A. et al. 2008b, arXiv:astro-ph/0810.2689

Ajima, Y., Anraku, K., Haga, T., et al. 2000, Nuclear Instruments and Methods in Physics Research A, 443, 71

Albert, J., Aliu, E., Anderhub, H., et al. 2008, Nuclear Instruments and Methods in Physics Research A, 588, 424

Allen, G. 1999, in International Cosmic Ray Conference, Vol. 3, International Cosmic Ray Conference, 480–+

Antoni, T., Apel, W. D., Badea, F., et al. 2003, Nuclear Instruments and Methods in Physics Research A, 513, 490

Atkins, R., Benbow, W., Berley, D., et al. 2004, ApJ, 608, 680

Atoyan, A. M., Aharonian, F. A., & Völk, H. J. 1995, Phys. Rev. D, 52, 3265

Axford, W. I., Leer, E., & Skadron, G. 1978, in International Cosmic Ray Conference, Vol. 11, International Cosmic Ray Conference, 132–137

Baade, W. & Zwicky, F. 1934, Proceedings of the National Academy of Science, 20, 259

Bamba, A., Yamazaki, R., & Hiraga, J. S. 2005, ApJ, 632, 294

Barwick, S. W., Beatty, J. J., Bower, C. R., et al. 1998, ApJ, 498, 779

Bass, S. A. et al. 1998, Prog.Part.Nucl.Phys., 41, 225

Bell, A. R. 1978, MNRAS, 182, 147

Berezhko, E. G. & Völk, H. J. 2004, A&A, 419, L27

Berezinsky, V. 2006, Journal of Physics Conference Series, 47, 142

Berge, D., Funk, S., & Hinton, J. 2007, A&A, 466, 1219

Berkey, G. B. & Shen, C. S. 1969, Physical Review, 188, 1994

Blandford, R. D. & Ostriker, J. P. 1978, ApJ, 221, L29

Bock, R. et al. 2004, NIM A 516, 2-3, 511

Bolz, O. 2004, PhD thesis, Ruperto-Carola University of Heidelberg

Breiman, L. 2001, Mach. Learn., 45, 5

Büsching, I., de Jager, O. C., Potgieter, M. S., & Venter, C. 2008, ApJ, 678, L39

Chang, J. et al. 2005, in International Cosmic Ray Conference, Vol. 3, International Cosmic Ray Conference, 1–+

Chang, J. et al. 2008, Nature, 456, 362

Cheng, H.-C., Feng, J. L., & Matchev, K. T. 2002, Physical Review Letters, 89, 211301

Cholis, I., Dobler, G., Finkbeiner, D. P., Goodenough, L., & Weiner, N. 2008, arXiv:astro-ph/0811.3641

Coppi, P. S. & Aharonian, F. A. 1997, ApJ, 487, L9+

Dario Serpico, P. 2008, arXiv:astro-ph/0810.4846

Davies, J. M. & Cotton, S. 1957, Journal of Solar Energy, 1 de Boer, W., Nordt, A., Sander, C., & Zhukov, V. 2007, A&A, 470, 61

Delahaye, T., Donato, F., Fornengo, N., et al. 2008, arXiv:astro-ph/0809.5268

Drury, L. O. 1983, Reports on Progress in Physics, 46, 973

DuVernois, M. A., Barwick, S. W., Beatty, J. J., et al. 2001, ApJ, 559, 296

Egberts, K. 2005, Master's thesis, Ruperto-Carola University of Heidelberg

Egger, R. J. & Aschenbach, B. 1995, A&A, 294, L25

Erlykin, A. D. & Wolfendale, A. W. 2001, Journal of Physics G Nuclear Physics, 27, 941

Erlykin, A. D. & Wolfendale, A. W. 2002, Journal of Physics G Nuclear Physics, 28, 359

Ferenc, D. & MAGIC Collaboration. 2006, in Bulletin of the American Astronomical Society, Vol. 38, Bulletin of the American Astronomical Society, 388–+

Fermi, E. 1949, Phys. Rev., 75, 1169

Fletcher, R. S., Gaisser, T. K., Lipari, P., & Stanev, T. 1994, Phys. Rev. D, 50, 5710

Funk, S., Hermann, G., Hinton, J., et al. 2004, Astroparticle Physics, 22, 285

Gahbauer, F., Hermann, G., Hörandel, J. R., Müller, D., & Radu, A. A. 2004, ApJ, 607, 333

Gaisser, T. K. 1990, Cosmic Rays and Particle Physics (Cambridge University Press)

Garcia-Munoz, M., Mason, G. M., & Simpson, J. A. 1975, ApJ, 201, L141

Goldreich, P. & Julian, W. H. 1969, ApJ, 157, 869

Green, D. A. 2006, A Catalogue of Galactic Supernova Remnants (2006 April version), astrophysics Group, Cavendish Laboratory, Cambridge, United Kingdom (available at "http://www.mrao.cam.ac.uk/surveys/snrs/")

Grenier, I. A. et al. 2005, in International Cosmic Ray Conference, Vol. 4, International Cosmic Ray Conference, 13–+

Gull, T. R., Kirshner, R. P., & Parker, R. A. R. 1977, ApJ, 215, L69+

Guzik, T. G. 2008, in COSPAR, Plenary Meeting, Vol. 37, 37th COSPAR Scientific Assembly. Held 13-20 July 2008, in Montréal, Canada., p.1138, 1138–+

Heck, D. 2006, Nuclear Physics B Proceedings Supplements, 151, 127

Heck, D. & Pierog, T. 2007, Forschungszentrum Karlsruhe, CORSIKA User's Guide

Heck, D. et al. 1998, Forschungszentrum Karlsruhe Report, FZKA 6019

Hillas, A. 1985, in International Cosmic Ray Conference, Vol. 3, International Cosmic Ray Conference

Hinton, J. A. 2004, New Astronomy Review, 48, 331

Hocker, A., Speckmayer, P., Stelzer, J., et al. 2007, arXiv:physics/0703039

Holder, J., Atkins, R. W., Badran, H. M., et al. 2006, Astroparticle Physics, 25, 391

Hooper, D., Blasi, P., & Dario Serpico, P. 2008, arXiv:astro-ph/0810.1527

Hoppe, S. 2008, PhD thesis, Ruperto-Carola University of Heidelberg

Hörandel, J. R. 2003, Astroparticle Physics, 19, 193

Hörandel, J. R. 2004, Astroparticle Physics, 21, 241

Hörandel, J. R. 2005, in Neutrinos and Explosive Events in the Universe, ed. M. M. Shapiro, T. Stanev, & J. P. Wefel, 365–+

Hörandel, J. R. 2008, Advances in Space Research, 41, 442

Hunter, S. D., Bertsch, D. L., Catelli, J. R., et al. 1997, ApJ, 481, 205

Kaspi, V. M., Roberts, M. S. E., & Harding, A. K. 2004, arXiv:astro-ph/0402136

Katsuda, S. & Tsunemi, H. 2008, Advances in Space Research, 41, 383

Kneiske, T. M. 2007, arXiv:astro-ph/0707.2915

Kneiske, T. M. & Mannheim, K. 2008, A&A, 479, 41

Kobayashi, T., Komori, Y., Yoshida, K., & Nishimura, J. 2004, ApJ, 601, 340

Komori, Y. 2006, Advances in Space Research, 37, 1918

Koyama, K., Petre, R., Gotthelf, E. V., et al. 1995, Nature, 378, 255

Kramer, M., Lyne, A. G., Hobbs, G., et al. 2003, ApJ, 593, L31

Krymskii, G. F. 1977, Akademiia Nauk SSSR Doklady, 234, 1306

Kubo, H., Asahara, A., Bicknell, G. V., et al. 2004, New Astronomy Review, 48, 323

Lagage, P. O. & Cesarsky, C. J. 1983, A&A, 125, 249

Large, M. I., Vaughan, A. E., & Mills, B. Y. 1968, Nature, 220, 340

Leahy, D. A. 1987, MNRAS, 228, 907

Maier, G. & Knapp, J. 2007, arXiv:astro-ph/0704.3567

Malkov, M. A. & O'C Drury, L. 2001, Reports on Progress in Physics, 64, 429

Manchester, R. N., Hobbs, G. B., Teoh, A., & Hobbs, M. 2005, Astron. J., 129, 1993

Manchester, R. N. & Taylor, J. H. 1977, Pulsars (W. H. Freeman and Company)

Mao, C. Y. & Shen, C. S. 1972, Chinese Journal of Physics, 10, 16

Moiseev, A. A., Ormes, J. F., & Moskalenko, I. V. 2007, arXiv:astro-ph/0706.0882

Moskalenko, I. & Porter, T. A.and Digel, S. W. 2006, Astrophys. J., 652

Moskalenko, I. V., Strong, A. W., & Reimer, O. 2004, in Astrophysics and Space Science Library, Vol. 304, Cosmic Gamma-Ray Sources, ed. K. S. Cheng & G. E. Romero, 279–+

Müller, D. 2001, Adv. Space Res., 27, 659

Nishimura, J. 1994, Universal Academy Press, Tokyo, 1

Ohm, S. 2007, Master's thesis, Ruperto-Carola University of Heidelberg

Orlando, E. & Strong, A. W. 2007, Ap&SS, 309, 359

Ormes, J. F. & Moiseev, A. 2007, in American Institute of Physics Conference Series, Vol. 921, American Institute of Physics Conference Series, ed. S. Ritz, P. Michelson, & C. A. Meegan, 494–495

Ostapchenko, S. 2004, arXiv:astro-ph/0412591

Picozza, P., Galper, A. M., Castellini, G., et al. 2007, Astroparticle Physics, 27, 296

Plucinsky, P. P., Snowden, S. L., Aschenbach, B., et al. 1996, ApJ, 463, 224

Pohl, M. & Esposito, J. A. 1998, ApJ, 507, 327

Profumo, S. 2008, arXiv:astro-ph/0812.4457

Seo, E. S., Ahn, H. S., Beatty, J. J., et al. 2004, Advances in Space Research, 33, 1777

Shen, C. S. 1970, ApJ, 162, L181+

Simpson, J. A. 1983, Annual Review of Nuclear and Particle Science, 33, 323

Sobczynska, D. 2007, NUCL.PART.PHYS., 34, 2279

Sreekumar, P., Bertsch, D. L., Dingus, B. L., et al. 1998, ApJ, 494, 523

Stecker, F. W., Hunter, S. D., & Kniffen, D. A. 2008, Astroparticle Physics, 29, 25

Stone, E. C., Cohen, C. M. S., Cook, W. R., et al. 1998, Space Science Reviews, 86, 357

Strong, A. W., Moskalenko, I. V., & Reimer, O. 2004, ApJ, 613, 956

The Calet Collaboration. 2007, Nuclear Physics B Proceedings Supplements, 166, 43

Thompson, D. J. 2008, Reports on Progress in Physics, 71, 116901

Thompson, T. A., Quataert, E., & Waxman, E. 2007, ApJ, 654, 219

Torii, S., Tamura, T., Tateyama, N., et al. 2001, ApJ, 559, 973

Torii, S., Yamagami, T., Tamura, T., et al. 2008, arXiv:astro-ph/0809.0760

Vincent, P., Denanca, J.-P., Huppert, J.-F., et al. 2003, in International Cosmic Ray Conference, Vol. 5, International Cosmic Ray Conference, 2887–+

Vink, J. 2003, arXiv:astro-ph/0311406

Völk, H. J. & Bernlöhr, K. 2008, arXiv:astro-ph/0812.4198

Weekes, T. C., Cawley, M. F., Fegan, D. J., et al. 1989, ApJ, 342, 379

Yagi, A. & et al. 2005, in International Cosmic Ray Conference, Vol. 3, International Cosmic Ray Conference, 425–+

Yanasak, N. E., Wiedenbeck, M. E., Mewaldt, R. A., et al. 2001, ApJ, 563, 768

Yar-Uyaniker, A., Uyaniker, B., & Kothes, R. 2004, ApJ, 616, 247

Zhang, J., Bi, X.-j., Liu, J., et al. 2008, arXiv:astro-ph/0812.0522

Danksagung

An dieser Stelle möchte ich mich bei den vielen Menschen bedanken, die auf unterschiedlichste Art und Weise zur Entstehung dieser Arbeit beigetragen haben. Mein Dank gilt

- Werner Hofmann dafür, dass er mir diese Arbeit ermöglicht hat, dass er mir beigebracht hat, was es heißt, wissenschaftlich zu arbeiten, für viele anregende Gespräche und eine immer offene Tür.
- Andreas Quirrenbach dafür, dass er das Koreferat übernommen hat und für eine etwas entspanntere Endphase.
- Jim Hinton for his brilliant ideas, his cheerfulness, and many kleinigkeiten that meant a lot to me (and the fact that he has a phone!).
- Konrad Bernlöhr für viele Monte Carlo Simulationen und diverse damit verbundene Hilfestellungen, and Mathieu de Naurois for his helpfulness and many, many proton simulations.
- Thomas Lohse für die Rechnungen des Likelihood-Fits.
- Ruth Crespo für viele Buchungen und dafür dass sie uns ein so unbürokratisches Leben ermöglicht.
- Svenja Carrigan für die nette Gesellschaft und Hilfestellungen in allen Lebenslagen.
- Christopher van Eldik für viele Antworten auf viele Fragen und Stefan Ohm für vielfältige technische Hilfestellungen.
- Rolf Bühler, Stefan Hoppe und Dalibor Nedbal für Zuspruch, Unterstützung und Ansporn und die schöne gemeinsame Zeit.
- der gesamten Heidelberger H.E.S.S.-Gruppe für die gute Zusammenarbeit, das gute Arbeitsklima und den Spass, den wir zusammen hatten. Und natürlich Christopher, Christoph, André und Willi für das Korrekturlesen.
- der H.E.S.S.-Kollaboration für die anregende Arbeitsatmosphäre und die schönen Kollaborationstreffen.

Schließlich möchte ich meinen Eltern Barbara und Gerhard Egberts für fast 30 Jahre Rückhalt, Liebe und Unterstützung danken.
Meine besondere Dankbarkeit gilt dem Umstand, dass ich meinen Mann Sebastian an meiner Seite habe, der mir jeden Tag aufs Neue die Kraft und den Mut gibt, alles zu geben.